Novel phases in quasi-one-dimensional frustrated spin chain LiCuSbO4

Bosiočić, Marko

Doctoral thesis / Disertacija

2022

Degree Grantor / Ustanova koja je dodijelila akademski / stručni stupanj: **University of Zagreb, Faculty of Science / Sveučilište u Zagrebu, Prirodoslovno-matematički fakultet**

Permanent link / Trajna poveznica: https://urn.nsk.hr/urn:nbn:hr:217:231132

Rights / Prava: In copyright/Zaštićeno autorskim pravom.

Download date / Datum preuzimanja: **2025-04-01**

Repository / Repozitorij:

Repository of the Faculty of Science - University of Zagreb

University of Zagreb

Faculty of Science

Marko Bosiočić

NOVEL PHASES IN QUASI-ONE-DIMENSIONAL FRUSTRATED SPIN CHAIN LiCuSbO$_4$

DOCTORAL DISSERTATION

Supervisors:

Prof. dr. sc. Miroslav Požek

Prof. dr. sc. Fabrice Bert

Zagreb, 2022

University of Zagreb

Prirodoslovno-matematički fakultet

Marko Bosiočić

NOVE FAZE U KVAZIJEDNODIMENZIONALNOM FRUSTRIRANOM SPINSKOM LANCU LiCuSbO$_4$

DOKTORSKI RAD

Mentori:

Prof. dr. sc. Miroslav Požek

Prof. dr. sc. Fabrice Bert

Zagreb, 2022

Mojim roditeljima. To my parents.

INFORMATION ON THE SUPERVISORS

Miroslav Požek is full professor at the Department of Physics, Faculty of Science, University of Zagreb. He started his career at the Ruđer Bošković Institute, Zagreb, where he was a junior researcher. He received his PhD from the University of Zagreb in 1992, and performed post-doctoral research at the Ruđer Bošković Institute and the University of Stuttgart, Germany, as a Humboldt fellow (1993-1995). Since 1998 he is employed at the Faculty of Science where he teaches General Physics, Statistics, Laboratory Exercises in Physics, and Physics of Semiconductors for undergraduate students, as well as Solid State Physics for graduate students. In 2018/19 he was visiting scientist at Leibniz Institute for Solid State and Materials Research (IFW) Dresden, Germany. His research interests are in experimental condensed matter physics, with focus on superconductors and strongly correlated systems. Experimental methods of interest include microwave absorption, electron spin resonance and nuclear magnetic resonance. He was principal investigator of the FP7 project #229390 „SOLeNeMaR" in 2008-13, and with this funding he established the Laboratory for Broadband NMR at the Department of Physics. He is a coauthor of more than 50 scientific papers, cited more than 860 times, with h-index 17. He has supervised 12 master theses and two completed PhD theses. The PhD theses resulted in 7 published scientific papers. Currently he is the principal investigator of the Croatian Science Foundation project „Microscopic study of induced phases in Strongly correlated electron systems".

Fabrice Bert is full professor at the Department of Physics, Faculty of Science, University of Paris-Saclay. He obtained is engineer diploma at the Ecole Centrale Paris in 1997 and his PhD from the University of Paris-Sud, Orsay in 2001, on the low energy excitations in quasicrystals studied with ultrasound experiments. After one year of post-docoral position at the CEA Saclay on the slow dynamics in spin glasses, he became assistant professor at the Laboratoire de Physique des Solides of the University Paris-Sud. He is currently teaching the solid state physics lecture at the master 1 level. His research interests are in the electronic correlations in quantum materials. In particular, he has been studying the local magnetic properties of frustrated magnetic systems, with a special interest for $S = 1/2$ frustrated quantum antiferromagnets which stabilize exotic ground states such as spin liquids. His main experimental techniques are nuclear magnetic resonance (NMR) and muon spin rotation (μSR) at low temperature. He is a coauthor of about 60 scientific papers, cited more than 2700 times, with h-index 29. He has co-supervised six completed PhD theses and 2 ongoing.

ACKNOWLEDGEMENTS

ABSTRACT

Search for novel (quantum) states of matter is one of the prime goals of contemporary physics. Spin nematic phase, where spins form a state with vanishing dipolar moment while a more complex operator remains with non zero expectation value, was predicted in one dimensional (1D) spin systems with ferromagnetic (FM) interaction between first and antiferromagnetic (AFM) interaction between second neighbours in the region near saturation field. After decades of mainly theoretical work in low dimensional spin systems, the first material candidates started to emerge, albeit no clear experimental evidence for such a phase was presented so far.

In this thesis, extensive experimental research on $LiCuSbO_4$ compound, a spin nematic candidate, is presented. This material shows distinct properties: absence of 3D ordering in zero magnetic field down to 30 mK, saturation field of $\approx$13 T. Nuclear magnetic resonance (NMR), muon spin rotation (μSR) and magnetic susceptibility (SQUID) techniques were used to unravel and tackle different parts of the experimental phase diagram.

We conclude that the search for possible quadrupolar nematic (QN) phase is narrowed down to a field range 12.5-13 T, and remains a goal for future investigations. Results in this thesis are compared to the recent work by Grafe et al. [1]. Also, we summarize most important work on similar compound $LiCuVO_4$, which is investigated for 15 years and available in form of single crystals.

Keywords: Frustration, 1D, spin chain, NMR, μSR.

SAŽETAK

Potraga za novim (kvantnim) stanjima materije je jedan od važnijih ciljeva moderne fizike. Spinska nematska stanja, gdje spinovi formiraju stanja s iščezavajućim dipolnim momentom, dok kompleksniji operatori imaju neiščezavajuće vrijednosti, predviđeni su u jednodimenzionalnim (1D) spinskim sustavimna s feromagnetskom interakcijom među prvim i antiferomagnetskom interakcijom među drugim susjedima u području blizu saturacijskog polja. Nakon desetljeća, uglavnom teorijskih, radova u niskodimenzionalnim spinskim sustavima, prvi spojevi kandidati počeli su se pojavljivati, iako do sada nema jasnih eksperimentalnih dokaza za postojanje takvih faza.

U ovom radu prezentirano je iscrpno eksperimentalno istraživanje spoja LiCuSbO$_4$, kandidata za opažanje spinske nematske faze. Ovaj spoj pokazuje sljedeća svojstva: nepostojanje 3D uređenja u nultom magnetskom polju na temperaturama iznad 30 mK i saturacijsko polje od $\approx$13 T. U ovom su radu korištene tehnike nuklearne magnetske rezonancije (NMR), mionske spinske rotacije (μSR) i magnetske susceptibilnosti (SQUID) kako bi se istražili različiti dijelovi faznog dijagrama.

Zaključujemo da je potraga za mogućom kvadrupolnom nematskom (QN) fazom sužena na područje između 12.5 i 13 T i ostaje ciljem za buduća istraživanja. Rezultati predstavljeni u ovom radu uspoređeni su s nedavnim radom Grafea i suradnika [1].

Također, saželi smo najvažnije radove na sličnom spoju LiCuVO$_4$, koji je predmet istraživanja više od 15 godina i dostupan je kao monokristal.

Contents

List of Figures

Chapter 1

Introduction - Why 1D?

One dimensional (1D) physical systems are the most simple ones, but in many cases they show many interesting phenomena which emerge as a result of interactions and correlations between electrons. In this chapter we will give a brief introduction and several examples of ongoing investigations which should challenge the question "What's new in 1D systems? Everything is solved there!".

General increase of computational resources led to development of new methods such as numerical Monte Carlo method, exact diagonalization, density matrix renormalization group (DMRG) [2] etc. These methods are powerful theoretical tools for solving 1D, and in some cases 2D problems, whose validity should be confirmed by experimental results. In physics (today) there are three scenarios: theory develops ahead of experiment, experiments ahead of theory or they go in parallel. The physics of 1D systems was a purely theoretical playground for a long time, by introducing a diversity of various properties (finite size effects, impurities, Dzyaloshinskii-Moriya interaction, single ion anisotropy, elements of frustration etc). The number of models increased rapidly, but experimental evidences for predicted phases remained lacking for a long period, due to the absence of clean materials. We will show a few examples of why low dimensional physics is of great interest for scientific research.

High-temperature superconductors

A large stimulus for experimental research and synthesis of new materials was the discovery of high temperature superconductors (HTSC-s). Soon after the discovery, scientists started to construct phase diagrams depending on charge carrier doping, which always included both AFM phase and superconducting (SC) phase (Fig 1.1). Since 2D Cu-O conducting planes
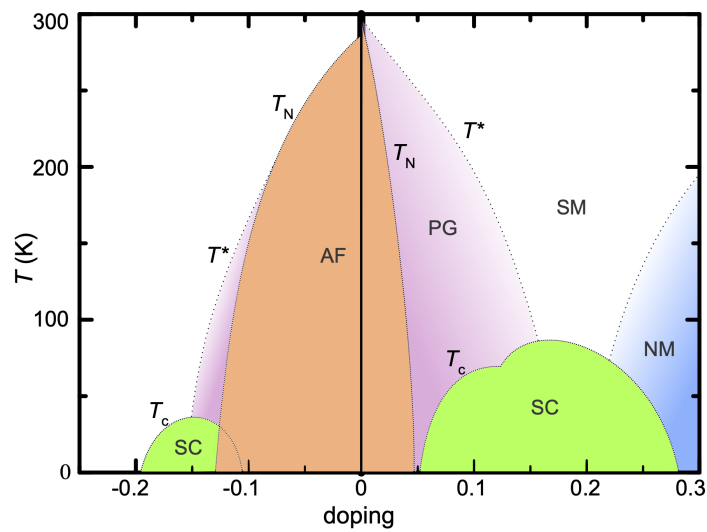
Figure 1.1: Schematic phase diagram of cuprate HTSC-s.

In dependence on charge carrier doping, the phase diagram of HTSC-s generically feature AFM and SC phases. Even today it is not understood whether these phases are somehow connected or not. Temperature T^* is the one which separates pseudogap (PG) behavior from the strange metal (SM) phase, T_c is transition temperature to a SC phase, and T_N temperature at which AFM order occurs. Blue phase on the right represents normal mental (NM) behavior.
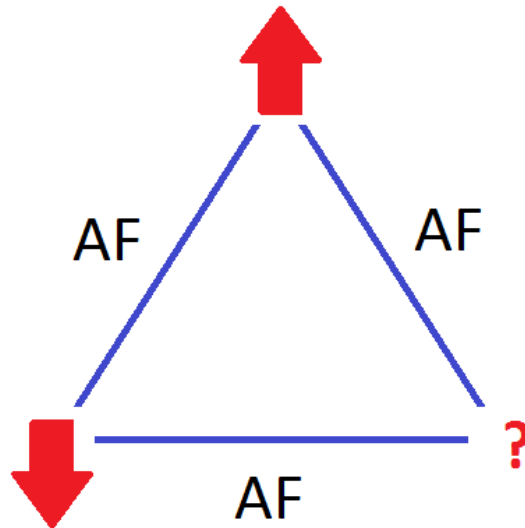
Figure 1.2: Frustration triangle.
Upper spin and the left one are aligned anti parallel. The right one wants to be anti
parallel to both upper and left spin, which is impossible and leads to frustration.

play a key role in cuprate HTSC, a natural question emerges: are AFM and SC phases somehow connected or not? For those who believed these effects are connected, understanding low dimensional magnetism became a key for understanding high temperature superconductivity: AFM fluctuations [4–8] (in these materials) were then considered as candidates for Cooper pair binding mechanism [9, 10].

1D and multiferroics

The discovery of multiferroicity, the coexistence and coupling of spin and charge degrees of freedom created a new boost for researching materials with such properties, with obvious possibilities for applied sciences. These materials are complex and their behavior is not completely understood yet. In search for simpler prototypical example, a frustrated 1D material with multiferroic properties was discovered: $LiCu_2O_2$ [11, 12]. In this frustrated chain cuprate compound, competition between ferromagnetic nearest neighbours (NN) exchange coupling J_1 and antiferromagnetic next nearestneighbours (NNN) exchange coupling J_2 leads to frustration, a common "ingredient" for many interesting physical properties (see Fig 1.2), such as spin liquids etc. The system exhibits a magnetic phase transition below $T_N = 25$ K to a spin spiral state. It turns out that ferroelectricity emerges simultaneously, and its polarization depends on

the direction and the strength of the applied magnetic field. The polarization $\mathbf{P}$ is proportional to the cross product between two neighboring spins $\mathbf{S}_i \times \mathbf{S}_j$, which is related to the pitch angle $\cos(2\pi\theta) = \mid J_1/(4J_2) \mid$.

Exotic excitations and new states of matter

Localized spin 1D systems are an even simpler subclass of such examples, since for their description one has to deal only with spin interactions, but they are still rich enough so they can "surprise" with their complexity. They are an ideal playground for theoretical calculations, both numerical and analytical, since it is much easier to calculate in 1D, than in 3D. Just to keep in mind the scope of the problem: the ground state of the simplest Heisenberg antiferromagnetic (AFM) Hamiltonian is not known:

$$H = \sum_{i,j} J\mathbf{S}_i\mathbf{S}_j, \tag{1.1}$$

in a system where the spins are located on the corners of kagome lattice, where sum over i goes over all sites, and sum over j with first neighbors and $J < 0$ AFM exchange interaction.

Historically, the first example of a classical spin chain was solved by Ernst Ising in 1925 [13]. There were high hopes that this model would be the first one to give microscopic insight into a thermodynamic phase transition at non-zero temperature. The next crucial discovery was made by Hans Bethe who managed to solve Heisenberg AFM model in 1D using the Bethe ansatz in 1931 [14]. Soon, Landau gave [15] a thermodynamic argument which is generally considered as "a proof" of the non existence of thermodynamic phase transitions in 1D systems with short range interactions. Many 1D models indeed do not have transition even at 0 K. However, seven decades later, Questa and Sanchez [15] emphasize that it is not a strict proof, and give various examples of 1D models which do exhibit a true thermodynamic phase transition. Hence, the generally accepted argument of non-existence of a phase transition in 1D with short range interactions is not true. Now we can see that as one gets deeper and deeper into the 1D physics, more complex problems start to emerge.

Due to the limited phase space, 1D systems are always strongly correlated, furthermore, these correlations are so strong that the Fermi liquid theory, as a starting approach to many-body problems, breaks down [16] and one has to use the Luttinger liquid (LL) theory as a starting point for treatment of 1D systems. Experimental signatures of the LL behavior were present in various systems such as: organic conductors, quantum wires, carbon nanotubes etc., but the first substantial experimental test of the LL behavior was done on spin ladder system

4
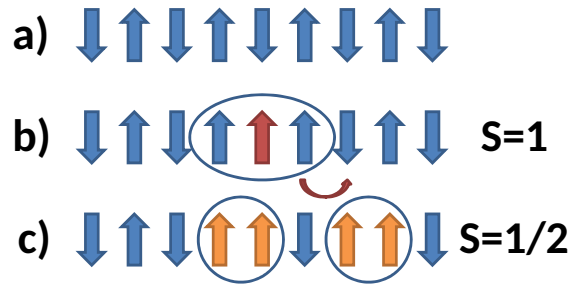
Figure 1.3: Spinons in 1D.

In AFM ordered spin chain (a), an elementary excitation is a magnon, a single spin flip that costs $2J$ of energy, whose spin is $S = 1$ (b). Two neighbouring spins can exchange positions without a change in the energy, which breaks magnons into two $S = \frac{1}{2}$ particles (spinons), which can propagate freely (c).

$CuBr_4(C_5H_12N)_2$ [17]. As mentioned before, despite theoretical progress, experimental observation of quasi 1D systems was lacking for a long period. One-dimensional systems can be classified as quantum-mechanical ones, which are in general described by some kind of Heisenberg Hamiltonian (low spin $S \leq 1$ together with the presence of quantum fluctuations ($J_z \approx J_x \approx J_y$)), and classical, which are described by Ising Hamiltonian ($S > 1$ or $J_z \gg J_x, J_y$). In the 1970s experimental realizations of 1D systems started to appear. One of the first examples of the classical spin chain was the compound $CsMnCl_2 \times D_2O$ [18]. Few years later the first quantum spin chain $CuCl_2 \cdot 2N(C_5D_5)$ [19] was discovered. The most studied examples of 1D spin systems are $KCuF_3$ [20, 21] and Sr_2CuO_3 [22, 23]. In general, compounds based on various stoichiometric ratios of strontium, copper and oxygen form various classes of chains and ladder systems which are widely investigated. It is worth to take a step back and mention spin-charge separation into spin $\frac{1}{2}$ excitations - spinons and holons - which were for the first time observed in the conducting 1D system $SrCuO_2$ in 1996 [24]. Spinons are spin $\frac{1}{2}$ excitations, quite common for 1D spin systems, contrary to the spin waves, whose elementary excitations are called magnons and carry spin 1. Interaction among spinons, was recently studied experimentally in the work by Mourigal et al. [25], where they used large single crystals of $CuSO_4 \cdot D_2O$, (2 cm^3). Although spinons are predicted and confirmed as elementary excitations in many 1D spin systems [21], they are quite exotic in 2D antiferromagnetic systems. However, they can appear in 2D spin liquids [21, 26]. A cartoon picture which explains this difference is
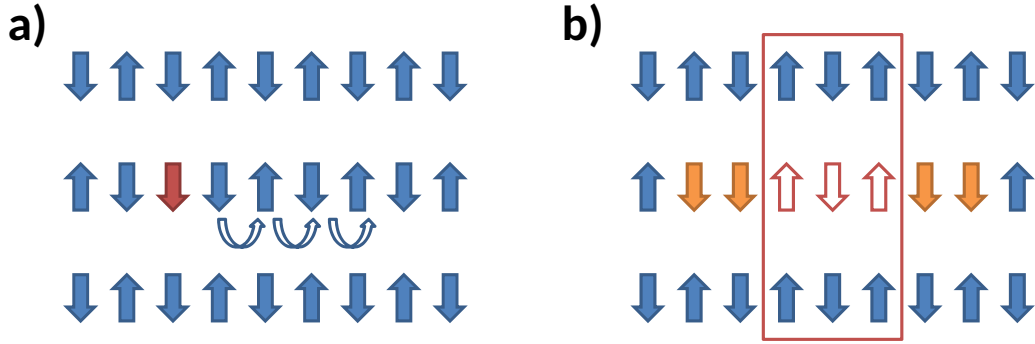
Figure 1.4: Spinons in 2D.

AFM ordered spins on 2D rectangular lattice. (a) Elementary excitation is again a single spin flip, but now with simple exchange of positions between spins, as two spinons move away from one another, a domain wall is formed which interacts ferromagnetically between neighboring chains (b).

shown in Figures 1.3 and 1.4. In the case of the simplest AFM interaction between neighboring spins JS_iS_j - in 1D, spinons are not bound and can propagate freely in 1D. Typically, in 2D they form a domain wall which interacts with spins from the chains above and below, and the energy has to increase. In 2D spin liquids, the ground state is highly degenerate and spins form singlets which can move (as water molecules move inside the water), so there is no interaction between spinons [26], providing that their density is low.

Spin nematics

In this thesis we will present search for a novel phase in 1D frustrated chain LiCuSbO$_4$ called spin nematic phase. This phase is described by an order parameter which is a tensor rank 2 or higher. More detailed explanation of this phase will be given in the following chapter but let us mention that such a state is difficult to observe because most techniques are sensitive to order parameters which are scalars or vectors. When one considers Hamiltonian multipole expansion, monopole couples to the potential, dipole to the field (gradient of the potential), quadrupole to the field gradient, etc.

Although, there are many more interesting effects in 1D spin systems, we will stop here hoping that we provided enough arguments to answer the question asked in the beginning "What's new in 1D systems? Everything is solved there!".

Chapter 2

Quadrupolar nematics

Magnetic order is usually related to some kind of spin pattern alignment with $\langle \mathbf{S}_1 \rangle \neq 0$. One can now ask if there are more subtle states that break rotational $O(3)$ symmetry, i.e. for every projection, where the average value of the spin operator $\langle S_1^\alpha \rangle = 0$ ($\alpha \in x, y, z$), while a more complex operator such as some bilinear combination of operator $\langle S^\alpha S^\beta \rangle \neq 0$ where $\alpha, \beta \in x, y, z$ do not vanish. We designate such multipolar states as nematic, with the quadrupolar one (bilinear combination) being the simplest. A more detailed discussion can be found in chapter 13 of the book [27]. One can immediately see that such quadruplar nematic (QN) state does not break the time reversal symmetry. The word "nematic" comes from analogy with the order parameter in liquid crystals, which is also a tensor rank 2 quantity. In 1888 Reinitzer tried to measure the melting point of cholesteryl benzoate crystals, but surprisingly he found two phase transitions instead of one [28], as shown in Fig. 2.1. It took until 1960s, when De Gennes realized the order parameter that describes the transition is not a simple number, or vector, but a tensor quantity [29]. A nice description of spin nematics is given by F. Mila in the

Figure 2.1: Phases of cholesteryl benzoate.
Liquid (left), liquid crystalline (middle) and solid (right) phase of cholesteryl benzoate [30].

reference [31].

2.1 Simple picture for bound spins $S = \frac{1}{2}$

For spin $S = \frac{1}{2}$ it is impossible to construct a quadrupolar nematic order which does not break time reversal symmetry [32], from single up $|\uparrow\rangle$ and down $|\downarrow\rangle$ states. However it is possible to construct such a state based on bond operators [32]. Let us take only two spins and label them as 1 and 2. We can now decompose the tensor operator $S_1^\alpha S_2^\beta$ into the irreducible tensor operators: $a)$ $Tr(S_1^\alpha S_2^\beta) \equiv \mathbf{S}_1 \cdot \mathbf{S}_2$ is a scalar, $b)$ $\mathbf{P}_{12} = \mathbf{S}_1 \times \mathbf{S}_2$ is a vector, and $c)$ $\mathcal{Q}_{12}^{\alpha\beta} = S_1^\alpha S_2^\beta + S_1^\beta S_2^\alpha - \frac{2}{3}(\mathbf{S}_1 \cdot \mathbf{S}_2)\delta_{\alpha\beta}$ is a symmetric tensor. Both $\mathbf{P}_{12}$ and $\mathcal{Q}_{12}^{\alpha\beta}$ are bilinear combinations and they describe an order where time-reversal symmetry is preserved. One can construct states which are invariant to the time-reversal:

$$
\begin{aligned}
|s\rangle &= \frac{1}{\sqrt{2}}(|\uparrow\downarrow\rangle - |\downarrow\uparrow\rangle), \\
|x\rangle &= \frac{i}{\sqrt{2}}(|\uparrow\uparrow\rangle - |\downarrow\downarrow\rangle), \\
|y\rangle &= \frac{1}{\sqrt{2}}(|\uparrow\uparrow\rangle + |\downarrow\downarrow\rangle), \\
|z\rangle &= -\frac{i}{\sqrt{2}}(|\uparrow\downarrow\rangle + |\downarrow\uparrow\rangle).
\end{aligned}
\tag{2.1}
$$

Time reversal symmetry breaking operators, which have finite magnetic moment are:

$$
\begin{aligned}
S_1^\alpha + S_2^\beta &= -i \sum_{\beta,\gamma \in \{x,y,z\}} \varepsilon_{\alpha\beta\gamma} |\beta\rangle\langle\gamma|, \\
S_1^\alpha - S_2^\beta &= i(|\alpha\rangle\langle s| - |s\rangle\langle\alpha|),
\end{aligned}
\tag{2.2}
$$

where $\varepsilon_{\alpha\beta\gamma}$ is Levi-Civita symbol. Non magnetic operators are:

$$
\begin{aligned}
\mathbf{S}_1 \cdot \mathbf{S}_2 &= \frac{1}{4} \sum_{\alpha \in \{x,y,z\}} |\alpha\rangle\langle\alpha| - \frac{3}{4}|s\rangle\langle s|, \\
P_{12}^\alpha &= \frac{1}{2}(|\alpha\rangle\langle s| + |s\rangle\langle\alpha|), \\
\mathcal{Q}_{12}^{\alpha\beta} &= -\frac{1}{2}(|\alpha\rangle\langle\beta| + |\beta\rangle\langle\alpha|) + \frac{1}{3}\delta_{\alpha\beta}|\gamma\rangle\langle\gamma|.
\end{aligned}
\tag{2.3}
$$

Bound wave function can be any linear combination in the base defined as in (2.1); $|\psi\rangle = c|s\rangle + \sum_\alpha d_\alpha|\alpha\rangle$, where $\alpha \in \{x,y,z\}$. States with real c and d do not break time reversal symmetry. For $c = 1$ ($\mathbf{d} = 0$), $|\psi\rangle$ is pure singlet, while for c=0 we refer to a state as n-nematic. When $c > 0$ and $\mathbf{d}$ is non-vanishing we call the state p-nematic. For further symmetry analysis one can take a look at the reference [33].
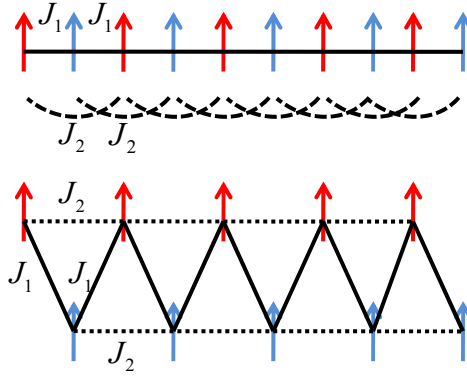
Figure 2.2: Spin chains and zig-zag ladders.
In the upper panel a chain with ferromagnetic interaction J_1 among NN and antiferromagnetic interaction J_2 among NNN. If we take blue spins and pull them down, while keeping the same interactions, we can see that spin chains with NN and NNN interaction are topologically identical to the zig-zag ladders. The rungs represent the J_1, while the legs J_2 interaction. Now, it is obvious that J_1 prefers FM ordering and J_2 AFM, which makes the "famous" frustrated triangle.

2.2 Theory of 1D frustrated spin chains

In this section we will give an overview on theoretical work where nematic order in 1D systems is predicted [34–36]. Let's consider the Heisenberg Hamiltonian:

$$H = \sum_i \{J_1 \mathbf{S}_i \mathbf{S}_{i+1} + J_2 \mathbf{S}_i \mathbf{S}_{i+2} - h S_i^z\}. \tag{2.4}$$

We take interactions between nearest neighbours (NN) J_1 and next nearest neighbours (NNN), J_2 in the presence of the applied magnetic field h, where the sum over i goes over the entire chain. We will introduce a further constraint and consider only FM interaction between NN ($J_1 < 0$) and AFM interaction between NNN ($J_2 > 0$). This configuration introduces geometrical frustration which is explained in Fig 2.2. If the energy of applied magnetic field h is comparable to the energies of J_1 and J_2, a competition between different interaction leads to the quantum criticality. A nematic phase in 1D chains was first predicted by Chubukov in 1991 [37]. After further theoretical calculations [34, 35, 38–40], experimentalist started the search for QN phase in real materials. In the following text we will present the theoretical phase diagram at $T = 0$ K [40].

If one considers the classical limit where a spin at site i is just a vector $\mathbf{S}_i$, the ground state is helical: $\mathbf{S}_i/S = (\sin(\theta)\cos(\phi_i), \sin(\theta)\sin(\phi_i), \cos(\theta))$ where the pitch angle between two neighboring spins is $\phi = \phi_{i+1} - \phi_i = \pm\arccos(-J_1/4J_2)]$ and the canting angle $\theta = \arccos(4hJ_2/S(J_1 + 4J_2)^2)$ [35]. The system is fully polarized at a saturation field above $h_s = S(J_1 + 4J_2)^2/4J_2$ or at zero field when $|J_1| > 4J_2$.

The quantum mechanical case for $S = \frac{1}{2}$ is much more complex. Helical order does not survive quantum fluctuations [35], however there are possibilities for long range algebraic (power law) correlations in contrast to the usual short range ones which are exponential. We will now inspect the theoretical phase diagram at $T = 0$ K (Fig. 2.3). The phases are named after the dominant correlation functions, and the boundaries between phases are not sharp, but may be described as crossovers. The variable parameters are the ratio of interactions J_1/J_2 and the magnetization which depends on applied field.

Vector chiral (VC) phase appears in the low field (magnetization) region. The spins are not ordered, their expectation values are zero ($\langle S \rangle = 0$). The correlation function which shows the slowest decay is the squared VC order parameter:

$$\kappa(r, d) = \langle [\mathbf{S}_0 \times \mathbf{S}_d]^z [\mathbf{S}_r \times \mathbf{S}_{r+d}]^z \rangle, \tag{2.5}$$

where $d = 1$ when we consider correlations across J_1 bonds, and $d = 2$ for J_2 bonds, while r represents distance bewteen 0-th and r-th spin.

Spin density wave phase of p bound spins (SDW_p) appears as we increase the applied magnetic field. Elementary excitations here are spin flips of p bounded spins ($\Delta S^z = p$), however, the dominant correlation function is:

$$\langle S_0^z S_r^z \rangle - \langle S_0^z \rangle \langle S_r^z \rangle \propto \cos\left[\frac{(1 - m/m_{sat})\pi r}{p}\right]\frac{1}{r^K}, \tag{2.6}$$

where we note that $\langle S_0^z \rangle = \langle S_r^z \rangle = m$. K is the Luttinger liquid (LL) parameter which is a function of $m(h)$, J_1 and J_2.

Nematic (N) phase appears just below the saturation field, separated by the dashed line from the SDW phases. The dominant correlation function in this phase is:

$$\left\langle \prod_{n=0}^{p-1} S_{0+n}^+ \prod_{n=0}^{p-1} S_{r+n}^- \right\rangle \propto (-1)^r \frac{1}{r^{1/K}}, \tag{2.7}$$

For $p = 2$, the phase is called quadrupolar, for $p = 3$ octupolar, and for $p = 4$ hexadecupolar. At this point, we mention that the compound LiCuSbO$_4$ studied in this work has the value of $J_1/J_2 \approx -2.2$ [41], and in the rest of the manuscript we will focus only on the part of the phase
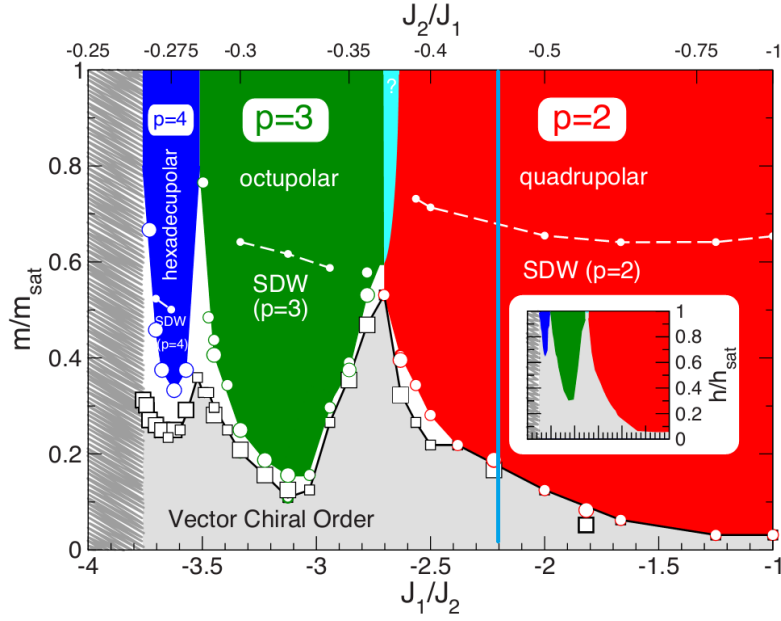
Figure 2.3: Phase diagram of the frustrated $J_1 - J_2$ chains

In the region of low magnetization (gray), the system is in the chiral phase. Above that the system behaves as LL, whose elementary excitations are flips of p bound spins (colored regions). Horizontal dashed lines are boundaries where the dominant correlation function changes from SDW_p- type to the nematic one (see text for further discussion). Magnetization m implicitly depends on the applied magnetic field h, and it is scaled with the saturation value (m_s, h_s). Vertical blue line represents position of $LiCuSbO_4$ in the phase diagram. The circles and squares are numerically evaluated points. [40]

diagram in which quadrupolar nematic (QN) phase is theoretically predicted. In section 2.1 we referred to a QN operator as any bilinear combination of spin operators. From this point on, we will reserve this term to the operator defined in equation (2.7), when $p = 2$, i.e. for the symmetric tensor $\mathcal{Q}_{12}^{\alpha\beta}$ in equation (2.3).

Fig. 2.4 shows the decay of the correlation functions in different phases, evaluated by density matrix renormalization group (DMRG).
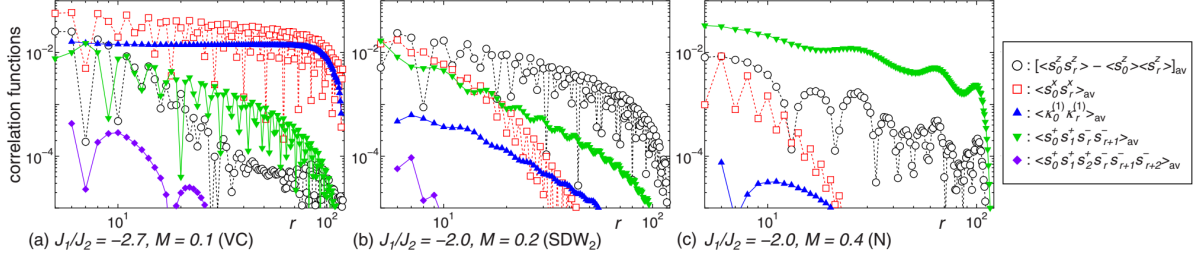
Figure 2.4: Decay of correlation functions in different phases. Result of the DMRG simulation. Saturation magnetization is $M_s = 0.5$ [36].

We will now take a closer look at the ground state at, and just below, the saturation field where a QN phase is expected [35, 36]. A mapping onto the LL Hamiltonian with hard core bosons is done in the following way. We start with a fully polarized state $|FM\rangle$. The elementary excitation is a spin flop of two bound spins $(-1)^r S_r^- S_{r+1}^-$ which corresponds to a boson creation operator $b_r^\dagger$. The boson density is $n_r \equiv b_r^\dagger b_r = \frac{1}{2}(\frac{1}{2} - S_r^z)$, where b_r is the annihilation operator at position r. The transverse spin correlations $\langle S_0^+ S_r^- \rangle$ are short-range, because it takes a finite amount of energy to break the bound magnon state. It is convenient to consider the excited magnon states with center of mass momentum k, with relative distance l between magnons:

$$|l; k\rangle = \frac{1}{\sqrt{N}} \sum_r e^{ik(2r+l)/2} S_r^- S_{r+l}^- |FM\rangle, \tag{2.8}$$

where N is the number of spins. The matrix elements are $\langle l; k|H|l'; k'\rangle = \delta_{k,k'} H_{l,l'}$, with nonvanishing elements of $H_{l,l'}$:

$$H_{l,l} = J_1(\delta_{l,1} - 2) + J_2(\delta_{l,1}\cos k + \delta_{l,2} - 2) + 2h,$$
$$H_{l,l+1} = H_{l+1,l} = J_1 \cos(k/2), \tag{2.9}$$
$$H_{l,l+2} = H_{l+2,l} = J_2 \cos k$$

Taking the result of [35], we state that for the QN phase in the range $-2.67 \leq J_1/J_2 < 0$, the
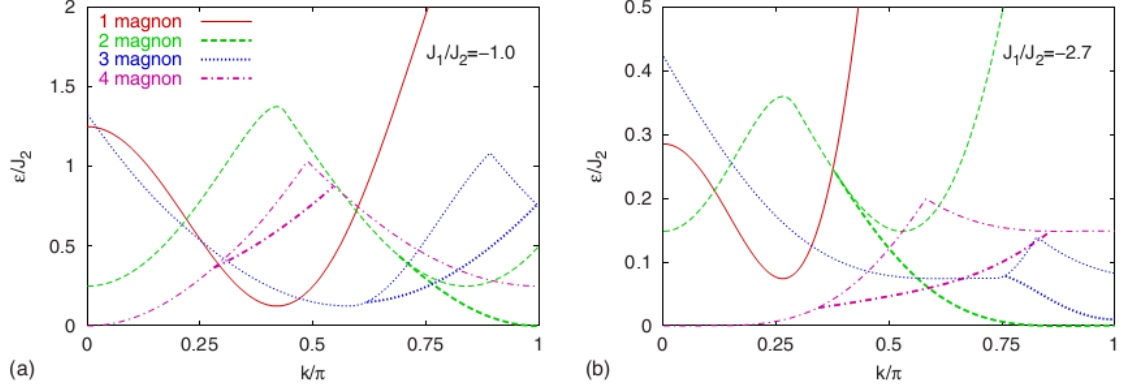
Figure 2.5: Energy $\epsilon(k)$ dependence of (multi)magnon excitations
For $J_1/J_2 = -1.0$ (a) and $J_1/J_2 = -2.7$ (b) at the saturation field. One can see that the lowest energy excitation for quadrupolar phase is at $k = \pi$ [35]
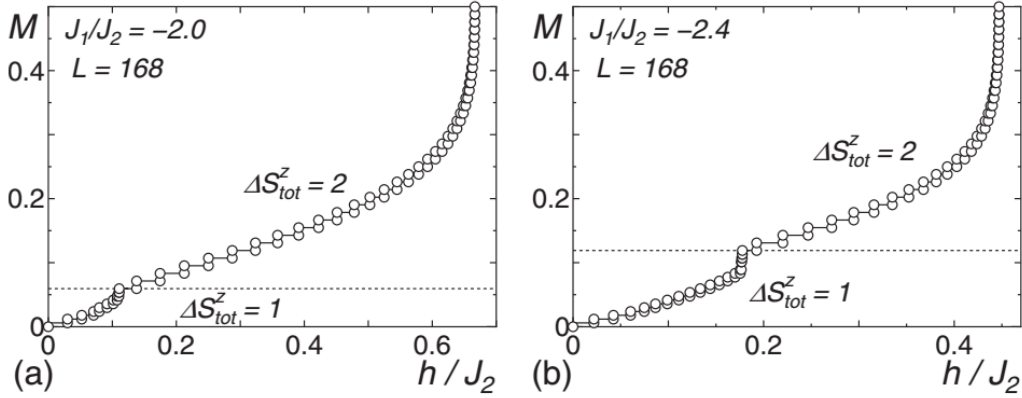
Figure 2.6: Magnetization curves at $T = 0$K.
Magnetization curves calculated using DMRG technique on chains with $L = 168$ spins for two different ratios of J_1/J_2 [36]. On the boundary between the VC and SDW_2 phases, the magnetization increases in steps from $\Delta S^z = 1$ to $\Delta S^z = 2$. This "S−shape" curve is the signature of 1-dimensionality, to our knowledge experimentally first reported by Klanjšek et al. [17]. Saturation magnetization is $M = 0.5$.

lowest energy excitation has momentum $k = \pi$:

$$\epsilon(\pi) = -J_1 - 3J_2 + \frac{J_2^2}{J_1 - J_2} + 2h, \tag{2.10}$$

and a cartoon picture where one can think about excitation as a sphere of two neighboring spin flips, corresponds very well to the real situation. The dispersion relation for $\epsilon(k)$ is shown in Fig. 2.5.

A crossover between the VC phase where excitations are single spin flips, to a SDW_2/QN,

was verified by DMRG simulations and is shown in Fig. 2.6.

The first theoretical predictions for experimental observables, such as magnetic susceptibility and heat capacity, were made by Heidrich-Meisner et al. in 2006 [34]. However, these are macroscopic probes. The former is very sensitive to impurities, while the latter does not probe the spin subsystem in isolation. Most experimental techniques measure two-point correlation functions and therefore the four-point correlation functions as in (2.7) for $p = 2$ are easily missed. Sato et al. have proposed an indirect way of probing the QN phase through NMR or neutron scattering experiments [42, 43]. NMR is especially convenient because its sensitivity increases with the strength of applied magnetic field. We will give a more detailed description of NMR observables in Chapter 3.2., but at the moment let us mention that NMR probes the dynamical correlations through the spin-lattice relaxation time T_1. In SDW_2 or QN phase, its behavior is expected to change asymptotically when $T \rightarrow 0$ K [42], $1/T_1$ is predicted to diverge as $T \rightarrow 0$ in the SDW_2 phase, while in QN phase $1/T_1 \rightarrow 0$ as system is cooled towards absolute zero. In the regime $\omega/k_B \ll T \ll J_2$, where ω is NMR frequency and k_B the Boltzmann constant, the temperature dependence of the spin-lattice relaxation rate $1/T_1$ is [43]:

$$\frac{1}{T_1} = D_1^{\parallel} T + D_2^{\parallel} T^{2K-1} + ..., \tag{2.11}$$

where $D_1^{\parallel}$ and $D_2^{\parallel}$ are temperature independent constants. Albeit this expression is similar to the one with dipolar field magnetism, parameters $D_1^{\parallel}$ and $D_2^{\parallel}$ are different, and a goal of future theoretical research [17]. In contrast, spin 1/2 AF chains without frustration, under applied magnetic field have a relaxation rate [44]:

$$\frac{1}{T_1} = E_1^{\parallel} T + E_2^{\parallel} T^{2K-1} + E_1^{\perp} T^{1/(2K)-1} ..., \tag{2.12}$$

where $E_1^{\parallel}$, $E_2^{\parallel}$ and $E_1^{\perp}$ are again temperature independent constants. The LL parameter K increases monotonically with applied magnetic field from 0 to 1. If one considers equation (2.11), for $K = \frac{1}{2}$ the asymptotic behavior of the relaxation rate changes due to the term related to $D_2^{\parallel}$. For $K < \frac{1}{2}$ it diverges when $T \rightarrow 0$ K, while for $K > \frac{1}{2}$ it approaches zero. On the other hand the last term in equation (2.12) ensures divergence for $T \rightarrow 0$K when $K > \frac{1}{2}$ and does not exist in equation (2.11), i.e. one of the terms $E_2^{\parallel}$ or $E_1^{\perp}$ always ensures divergence when $T \rightarrow 0$K irrespective whether we are in $K < \frac{1}{2}$ or $K > \frac{1}{2}$ regime. The value $K = \frac{1}{2}$ determines the border between the SDW_2 and the QN phase. This is shown in Fig. 2.7.

Due to this difference in $1/T_1$ asymptotic behavior when $T \rightarrow 0$K between AF and $J_1 - J_2$ chains, one could indirectly give an experimental proof for the existence of QN phase.
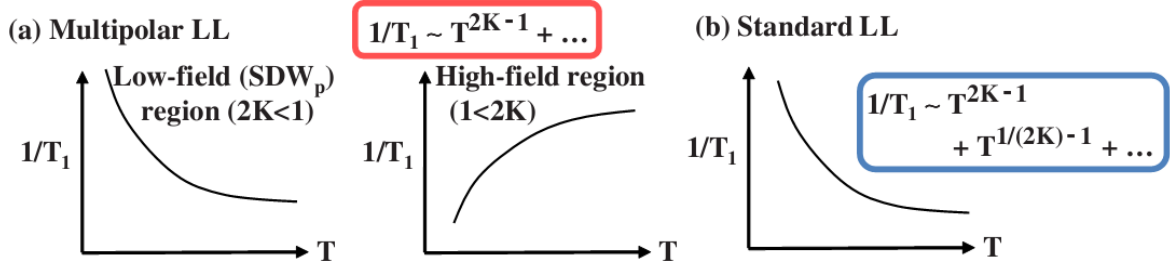
Figure 2.7: Temperature dependence of the NMR relaxation rate $1/T_1$
In: (a) Multipolar LL ($J_1 - J_2$ chains) in the low and high field region and (b) standard LL (AF chains). In the standard LL, there are contributions from two terms, where one of them always diverges when $T \to 0$K [42].

2.3 Experimental realizations of 1D frustrated spin chains

Experimentally, a high ratio of $J_1(J_2)/T_N$ indicates the existence of frustration and/or low dimensionality. Table 2.1 shows experimentally determined parameters of some compounds described by the $J_1 - J_2$ Hamiltonian. Although we considered so far ideal chains, which do not order at $T = 0$K, in real materials it is possible that a small interchain interaction J' leads to a true 3D order at s finite temperature T_N. The values of T_N at zero magnetic field are given in Table 2.1. As the magnetic field is increased it can stabilize or change the nature of the ground state. However, at high field where a nematic phase is expected, the field can suppress 3D ordering at T_N so existence of T_N at zero field does not play a determining role, since energy of the applied field is much stronger than the energy of thermal fluctuations (1 T magnetic field corresponds to ≈ 1.4 K). The first row of table 2.1 lists the parameters for the compound investigated in this work, whose properties will be presented in details in the following section. Its advantage is a low saturation field, accessible by standard laboratory magnets, but it is available only in the powder form. The most investigated compound listed in the table is LiCuVO$_4$. It has been synthesized in form of single crystals [45], which allows better experimental accuracy of the data. The main disadvantage of this compound is a high saturation field, which can not be reached at the present moment with persistent magnets. In the recent work [47, 55], authors have been debating the existence of a QN phase in this compound, however this question remains unsolved [31]. Other listed compounds show a variety of interesting phenomena, not only related to multipolar phases. The compound PbCuSO$_4$(OH)$_2$ drew attention due to a very interesting and complicated experimental phase diagram shown in Fig 2.8.

Table 2.1: $J_1 - J_2$ compounds.

Experimentally determined properties of most known materials described by a $J_1 - J_2$ Hamiltonian. H denotes saturation field while T_N denotes ordering temperature.

Compound	J_1[K]	J_2[K]	J_1/J_2	$\mu_0 H$[T]	T_N[K]	$|J_1/T_N|$	Ref.
$LiCuSbO_4$	-75	34	-2.2	13	<0.03	>2500	[41]
$LiCuVO_4$	-18.5	44	-0.42	45-52	1.7-2.3	9.3	[45–47]
$LiCu_2O_2$	-66-94	168	-0.41	est. 110	9,22,24	10.4	[48, 49]
Li_2CuO_2	-100	60	-1.7	?	9	11.1	[50]
$Cs_2Cu_2Mo_3O_{12}$	-93	33	-2.8	≈ 10	1.85	50.3	[51]
$Rb_2Cu_2Mo_3O_{12}$	-138	51	-2.7	14	< 2	69	[52]
$PbCuSO_4$	-100	36	-2.8	≈ 10	2.8	36	[53]
$NaCu_2O_2$	-16.4	90	-0.18	?	12	1.3	[54]

2.4   LiCuSbO$_4$ - previous knowledge

The first report on LiCuSbO$_4$ was given by Dutton et al. in 2012 [41]. In that work both, basic characterization (synthesis, SQUID, X-ray diffraction, EPR) and more detailed experiments have been made (neutron scattering, heat capacity in dilution refrigerator).

Characterization using X ray diffraction revealed that the compound crystallizes in the space group $Cmc2_1$ with a orthorhombic unit cell ($a = 5.74260$Å, $b = 10.86925$Å, $c = 9.73048$Å). The copper ions Cu^{2+} carry $s = 1/2$ unpaired spins. The structure is shown in Fig 2.9. The basic building blocks are CuO$_6$ edge-sharing octahedra which form chains along the a axis. Jahn-Teller distortion elongates Cu-O bonds in the direction of the local z axis (see Figure 2.9).

Figure 2.10 shows the bulk magnetic properties (magnetization and susceptibility) of the compound. A maximum in temperature dependence of magnetic susceptibility is observed in fields below 11 T, typical for the existence of short range correlations. In higher fields, χ monotonically increases. Figure (2.10b) shows magnetization measurements. At the lowest temperature (2 K) the magnetization curve bends, indicating that saturation regime is reached. The saturation field is estimated from the inflection point at $\mu_0 H_s \approx 12$ T. We emphasize that at the saturation field, a sharp vertical slope of the magnetization is expected, as in Fig 2.6. The nonexistence of such a sharp cusp in Fig (2.10b) possibly indicates that the temperature is too high for the precise determination of the saturation field. A simulation of the magnetization curve, shown by dashed line in Fig 2.10b was done using 24 spin system. In order to achieve
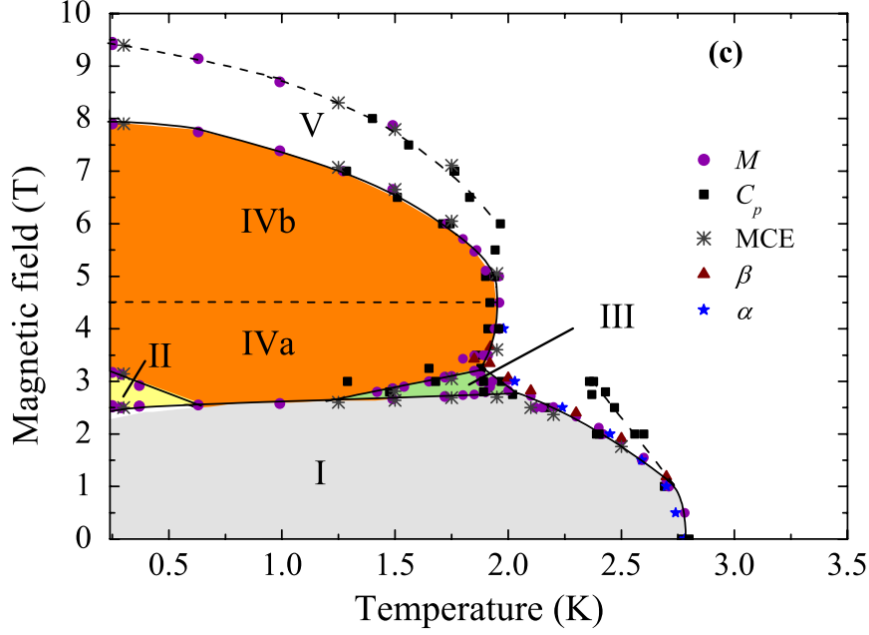
Figure 2.8: Experimental phase diagram of PbCuSO$_4$(OH)$_2$.
(I) ground state of eliptical magnetic helix, (II) magnetic hysteresis is observed, (III) longe range FM ordered phase; (IV) weak FM phase: (IVa) - region with negative slope in susceptibility,(IVb) the slope is positive indicating saturation of of this weak FM phase. Phase V is unknown, with possible multipolar correlations. The following techniques were used to sample phase diagram [53]: specific heat (C_p), the magnetocaloric effect (MCE), magnetization (M), susceptibility(χ), magnetostriction (β) and thermal expansion (α).

better agreement with measured data additional anisotropy to the Hamiltonian (2.4) was introduced where Δ quantifies the anisotropy ($\Delta = 1$ isotropic model, $\Delta > 1$ Ising type anisotropy, $\Delta < 1$ easy plane anisotropy):

$$H = J_1 \sum_i \left(\frac{3}{2+\Delta}(S_i^x S_{i+1}^x + S_i^y S_{i+1}^x + \Delta S_i^z S_{1+1}^z) + \frac{J_2}{J_1}\mathbf{S}_i\mathbf{S}_{i+2} - h(S_i^z \cos\theta + S_i^x \sin\theta) \right),$$
(2.13)

The angle θ is the one between the applied field h and molecular axis z. This model revealed the following: $J_1 = -75$ K, $J_2 = 34$ K and $\Delta = 0.83$, with 10% error bars. From a crystallographic point of view, there is a single distance between Cu-Cu bonds, but two different exchange paths exist between the atoms, so $J_1 - J_1' - J_2$ model could be an improved model Hamiltonian. Within this thesis we will assume that Hamiltonian 2.13 is a good starting point for the interpretation of our experimental data. Electron paramagnetic resonance measurements reveal an average g
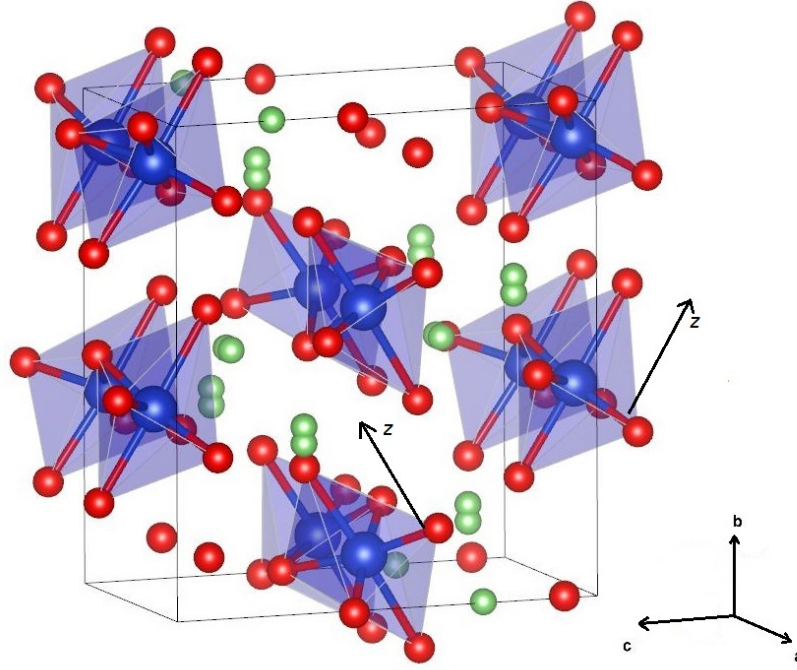
Figure 2.9: Crystal structure of LiCuSbO$_4$.

Unpaired spins are localized on Cu^{2+} ions (Blue) centered in CuO$_6$ octahedra. Edge sharing octahedra form spin chains parallel to the a axis. The local z axes, which points in the direction of the Jahn-Teller elongation, of two adjacent spin chains are canted by $34°$ in opposite directions with respect to the b axis. Distribution of Li(1) (Green) is supposed to be in the direction of b axis, while Li(2) in the direction of a axis. Oxygen atoms are labeled in red color. Antimony ions are omitted for clarity.

factor $g_{av} = 2.10$ [41].

Heat capacity (C_p) measurements presented in Fig. 2.11 show a broad peak at $T = 7$ K for zero field, which corresponds to a peak in C_p/T at 4.3 K. Upon applying higher fields, this peak shifts towards lower temperatures and in $B = 10$ T it is completely suppressed. The lattice contribution to C_p was modeled with the Debye law ($\theta_D = 410$ K). Magnetic entropy $\Delta S = \int C_p/T dT$ was extracted above 0.1 K. The magnetic entropy approaches the expected value ($R\ln2$) around 50 K, as shown in the inset of Fig. 2.11a.

At lower temperatures a second peak, enhanced by the applied magnetic field, emerges around $T = 0.6 - 0.7$ K. Its intensity increases with fields up to $B = 11$ T, and then quickly diminishes, and vanishes completely in $B = 14$ T. In the cartoon picture one would expect that the energy of the quadrupolar excitations does not change with applied field (it couples to the gradient of the magnetic field in the Hamiltonian), but the number of excitations is dependent
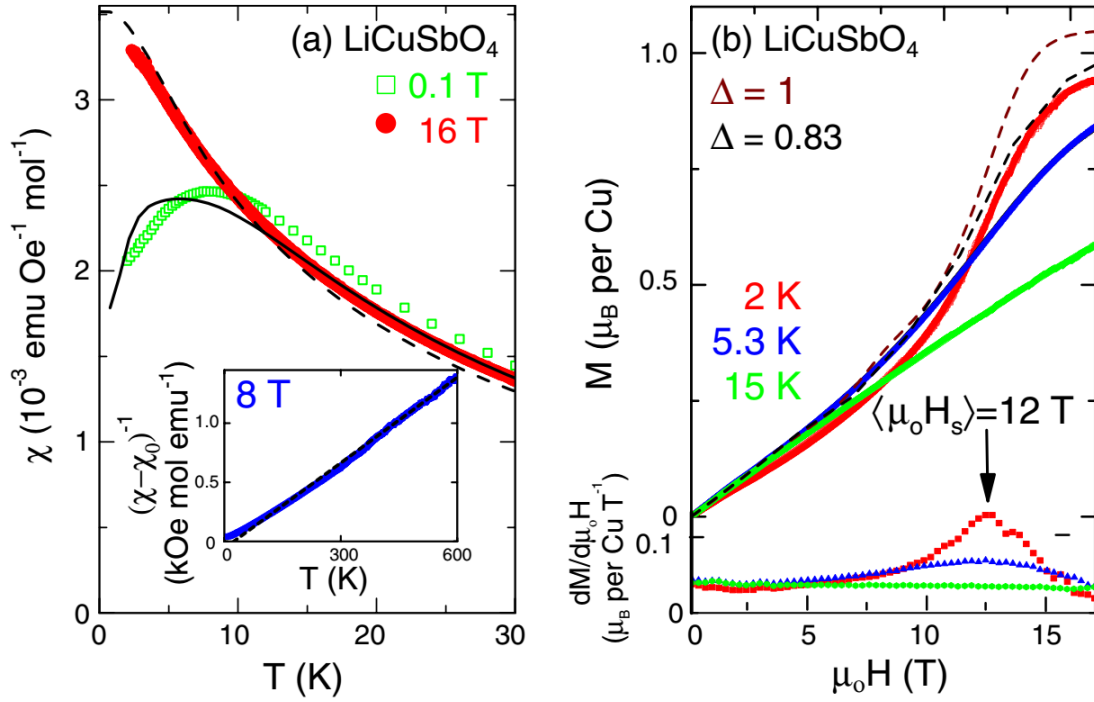
Figure 2.10: Magnetization measurements on LiCuSbO$_4$.
(a) Susceptibility measurements in 0.1 and 16 T field together with calculated susceptibility curves in respective fields (full and black dashed lines). A maximum in susceptibility (χ) such as the one in 0.1 T occurs in fields below 11 T. Above 11 T χ increases monotonically with lowering temperature. Inset shows a Curie-Weiss plot in 8 T field. (b) Magnetization measurements at various temperatures. At a lowest measured temperature of 2 K, an inflection point occurs around 12 T indicating the entrance in saturation regime. The full and dashed black lines are the result of simulation using Hamiltonian (2.13) with $J_1 = -75$ K, $J_2/J_1 = -0.45$ and $\Delta = 0.83$. Brown dashed line accounts for $\Delta = 1$ and $J_1 = -68$ K with same ratio of J_2/J_1 [41].

on the applied field (intensity of the peak). This, together with accessible saturation field values, gave a strong motivation for further investigations of LiCuSbO$_4$ presented in this thesis.

In addition to the so far presented experimental data, inelastic neutron scattering experiments in zero magnetic field were performed [41] (Fig 2.12). Figure 2.12a and b show the powder averaged structure factor $S(Q,\omega)$, at $T = 1.5$ K and 6 K, respectively. Figure 2.12a and b show the absence of gap in the magnetic excitations down to 0.07 meV, which is the resolution of the instrument. Figure 2.12c shows powder averaged $S(Q,\omega)$ calculated by exact diagonalization method for 16 spins, and parameters $J_1 = -75$ K, $J_2 = 34$ K with $\Delta = 0.83$.
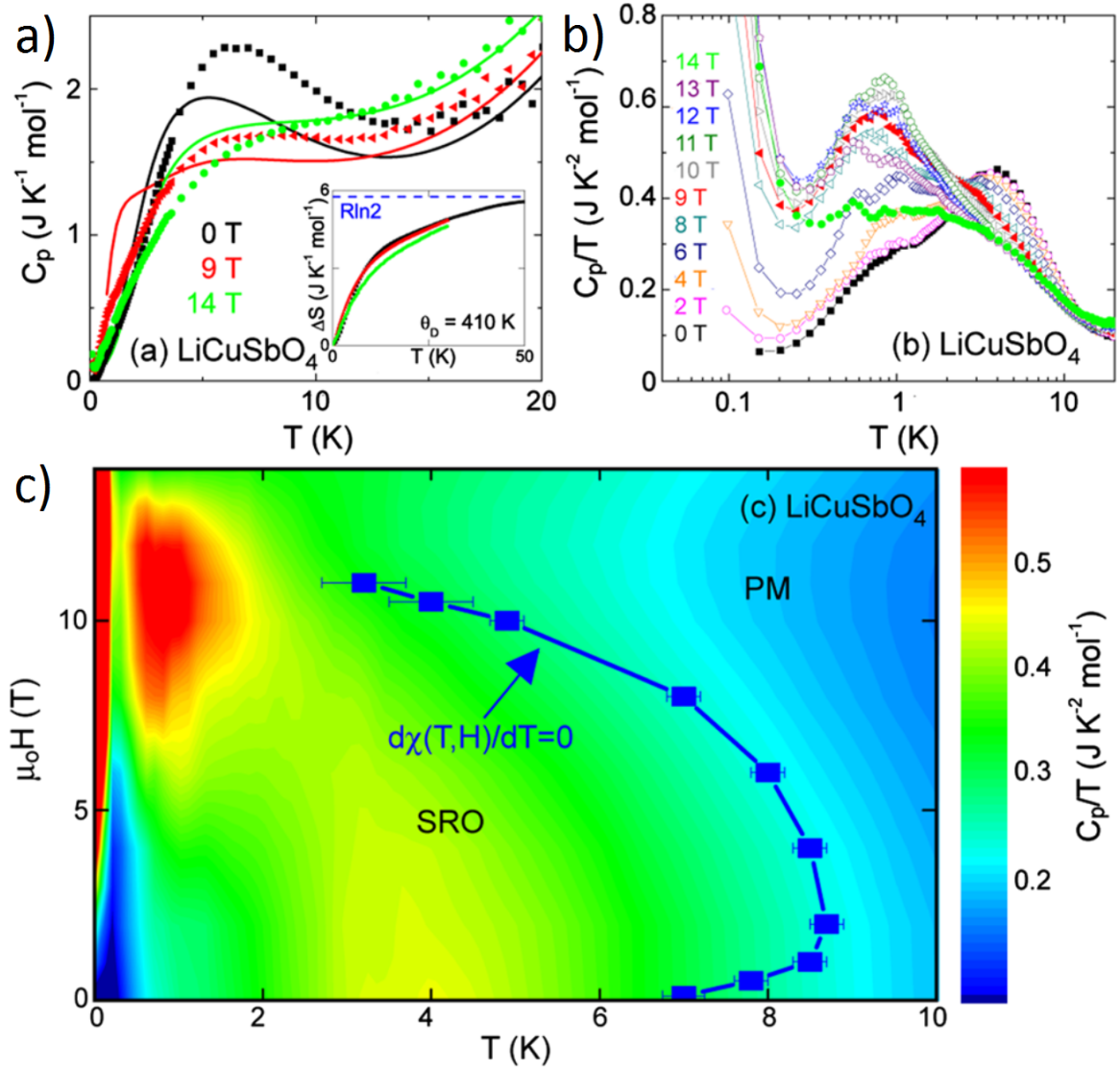
Figure 2.11: Heat capacity measurements on LiCuSbO$_4$.
(a) C_p as a function of temperature. Full lines represent theoretical results from exact diagonalization of a ring model with 16 spins in various fields. The inset shows the recovery of magnetic entropy. (0 T, 9 T, 16 T) (b) C_p/T vs. temperature in logarithmic scale. (c) Phase diagram from the heat capacity data, blue points show occurence of the peak in magnetic susceptibility. SRO stands for short range order/correlations.

Agreement between observed and calculated excitation spectra in the region 0.5 meV$<\hbar\omega<1.5$ meV is quite good. At low temperatures (1.5 K compared to 6 K), below 0.30 meV a magnetic quasielastic signal appears. As a function of momentum transfer, the signal is strongest for $Q = 0.52$ Å^{-1}, which is in accordance with $Q = 0.475\pi/a$ (0.26 Å^{-1}) expected for short-range correlations from [56].
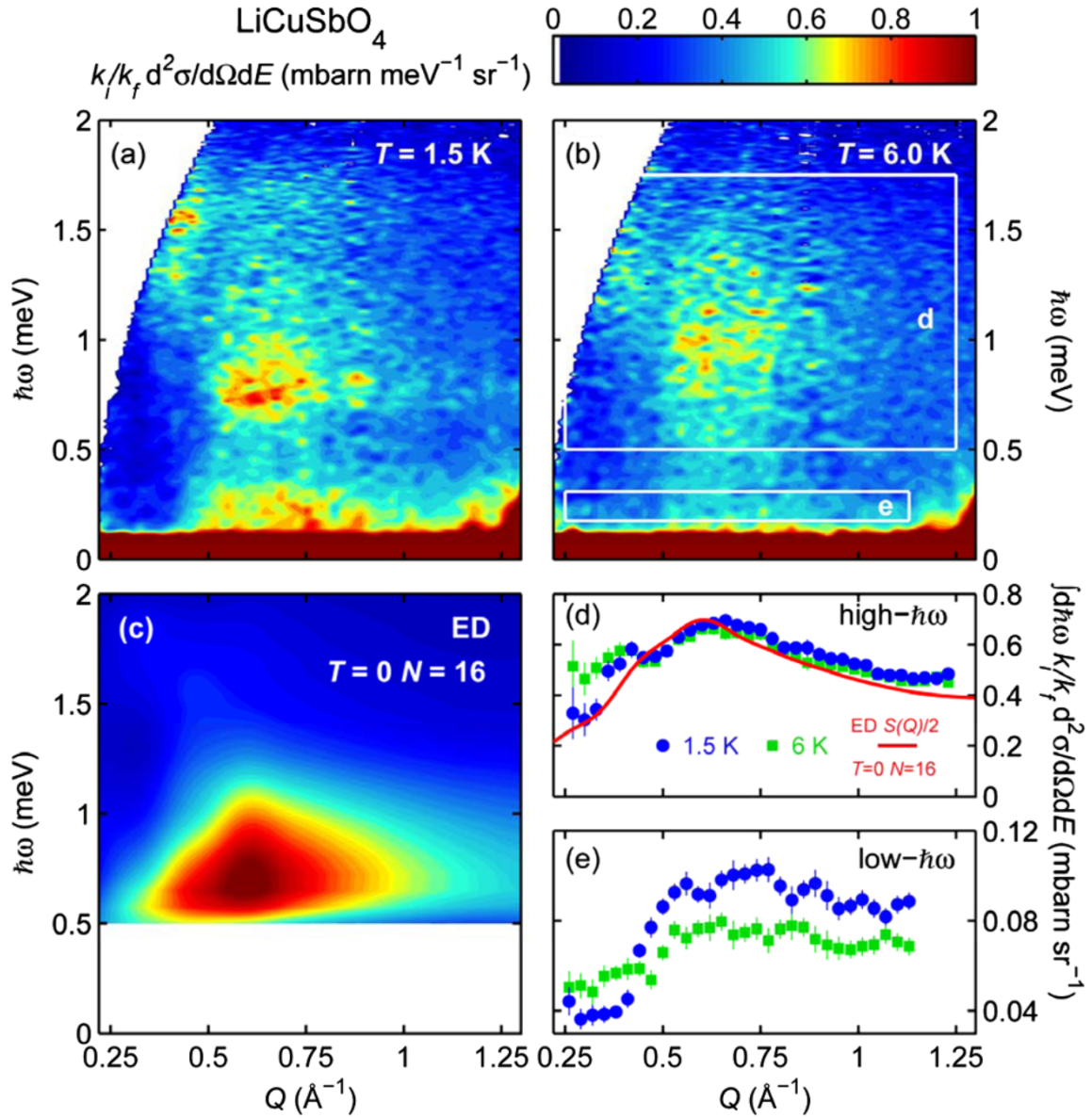
Figure 2.12: Neutron measurements on LiCuSbO$_4$.
Averaged dynamical structure factors $S(Q, \omega)$ at (a) $T = 1.5$ K and (b) $T = 6$ K.
(c) Exact diagonalisation calculation of $S(Q, \omega)$ for 16 spin chain. (d) Momentum-transfer dependence of the higher-energy signal $0.50 < \hbar\omega < 1.75$meV. (e) Quasielastic signal $0.18 < \hbar\omega < 0.31$meV. [41]

Chapter 3

Experimental methods

In this chapter we will give a short overview of muon spin rotation (μSR) and nuclear magnetic resonance (NMR) techniques, with emphasis on observables that provide useful information on magnetic insulators such as $LiCuSbO_4$ compound. The operation of the dilution refrigerator will be explained briefly, together with sample preparation.

3.1   Muon spin rotation

Muon spin rotation has become a common local technique for exploring condensed matter physics. Its high sensitivity to small magnetic fields (down to 0.1 G) makes it an ideal probe for exploring magnetic properties of materials. It can also probe magnetic fluctuations in a wide frequency range (10^4 to 10^{12} Hz). This unique time window makes it useful in the intermediate region (10^5 to 10^8 Hz) where nuclear magnetic resonance and neutron scattering techniques are less suitable.

3.1.1   Production of Muons

First, we are going to describe how muons are produced at the ISIS facility at the Rutherford Appleton Laboratory (RAL) in the United Kingdom, where the measurements in this thesis were performed (Figure 3.1). H^- ions are produced at the ion source and accelerated to 665 keV. Ions then enter into a linear accelerator where they are accelerated to 70 MeV. At the last stage H^- ions are stripped to protons and accelerated to 800 MeV (84% of speed of light) into the synchrotron. Proton beams are then guided to their targets where neutrons and muons are produced. Graphite or beryllium target are usually used for muon production. Pions are produced during the collision of the incident protons with the target nuclei. They have a short
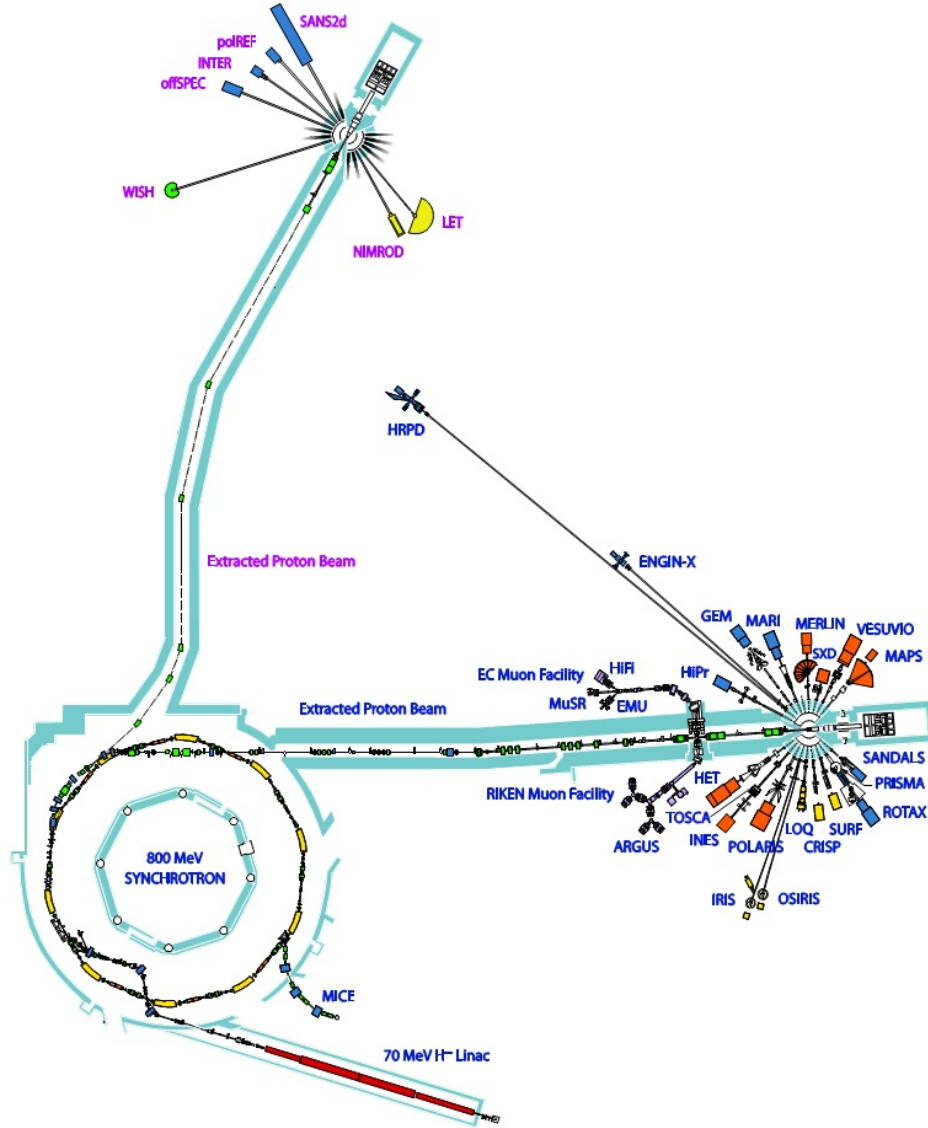
Figure 3.1: Experimental scheme at the RAL in UK.

Muon and neutron production and beam lines at ISIS (RAL, UK)

lifetime (26 ns) after which they decay into muon and neutrino

$$\pi^+ \to \mu^+ + \nu_\mu. \tag{3.1}$$

Only pions which are at rest in the laboratory frame are used. Muon and neutrino must have opposite momenta to conserve momentum which is initially zero. The neutrino has its spin directed opposite to the momentum (negative helicity) and since the pion has zero spin, muon's spin is also antiparallel to its momentum. This allows us to get muon beams which are 100% polarized, which is an advantage compared with other microscopic techniques, NMR or electron spin resonance (ESR), where strong external magnetic field are needed to obtain
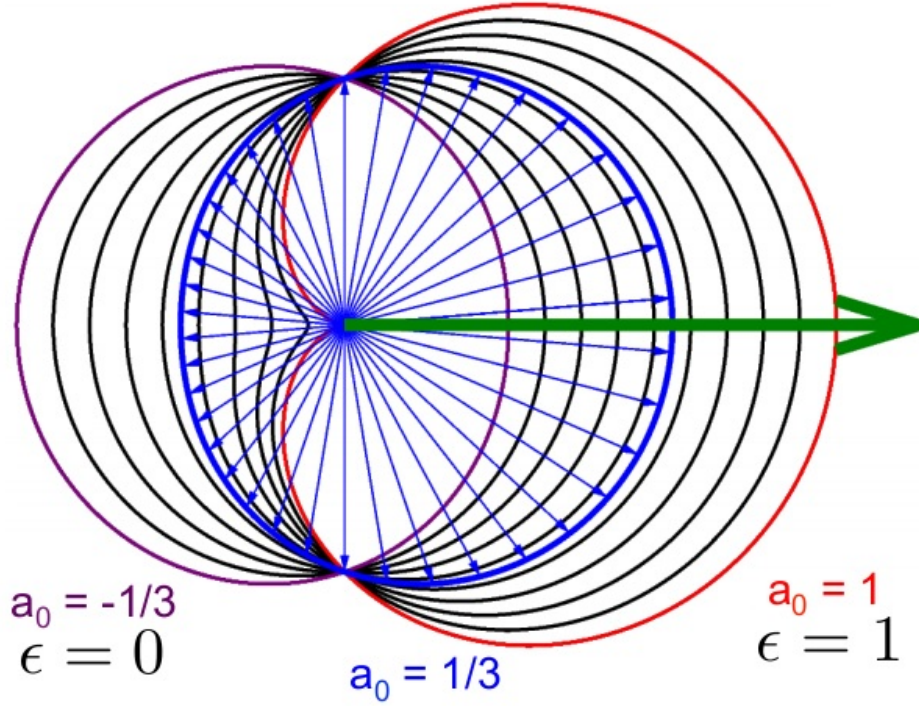
Figure 3.2: Distribution of emitted positrons

The angular distribution of emitted positrons with respect to the initial muon spin direction (green arrow). Distributions for several values of $a_0 = -1/3$ (purple), $a_0 = 1/3$ (blue) and $a_0 = 1$ (red) are plotted. Values of a_0 and ϵ are given in equation 3.3.

partial polarisation, given by Boltzman's distribution over spin levels. The muons produced out of stationary pions near the surface of graphite target are called surface muons, their kinetic energy is 4.119 MeV and momentum 29.8 MeV/c. Muon beams are then guided towards the sample with a series of dipole and quadrupole magnets. After implantation of muons inside the sample they lose energy quickly (0.1-1 ns) by ionization of atoms and by scattering with electrons to a few keV. The remaining energy is lost through a series of successive electron capture and loss reactions. All these processes are Coulombic so muons spins remain conserved until they stop in the sample.

Muons stopped in the sample decay after time t with probability e^{-t/τ_μ} where $\tau_\mu = 2.2\ \mu$s is the lifetime of the muon (we are neglecting the time between the decay of the pion and slowing down of the muon which is small compared to the muon's lifetime τ_μ). The muon undergoes a three body decay process:

$$\mu^+ \rightarrow e^+ + \nu_e + \overline{\nu}_\mu, \tag{3.2}$$

where only the positron is detectable. This decay occurs via weak interaction and does not
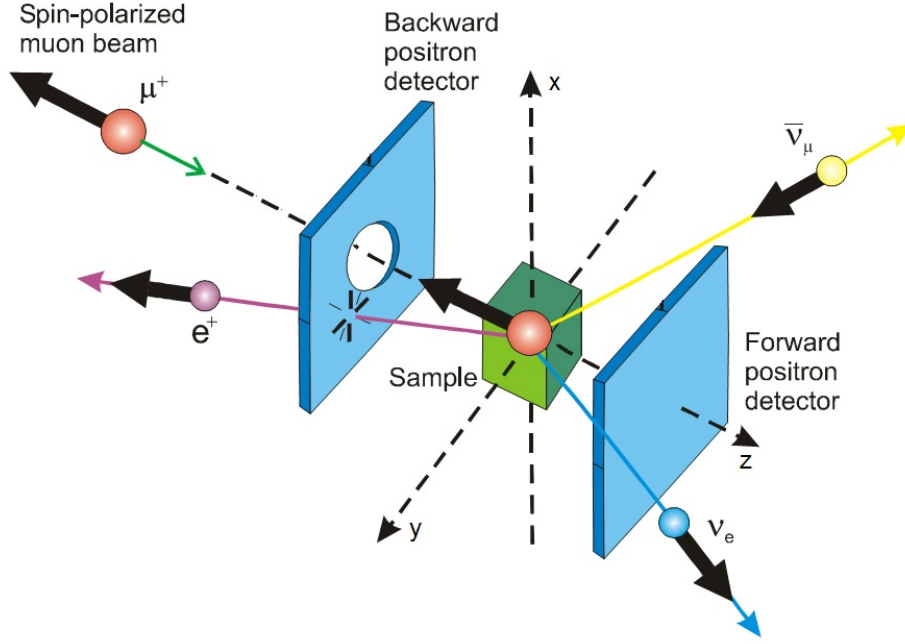
Figure 3.3: Typical muon spectrometer

Simplified scheme of typical muon spectrometer. Polarized muon beam enters through backward positron detector and falls in the sample. Detectors count the number of emitted positrons detected in either forward or backward detectors. [57]

conserve parity. In practice this means that the positron will be preferentially emitted in the direction of muon spin. This is an essential feature which allows us to directly relate the direction of the positron momentum to the muon's spin. The angular distribution of the emitted positrons is given by:

$$p(\theta) = 1 + a_0(\epsilon) \cos \theta; \; a_0(\epsilon) = \frac{2\epsilon - 1}{3 - 2\epsilon}, \quad (3.3)$$

where $\epsilon = E/E_{max}$ is the ratio of positron energy E divided by its maximum value $E_{max} = 52$ MeV. The angular distribution for several values of parameter a_0 is shown in Figure 3.2.

If all emitted positrons are detected with the same efficiency irrespective of their energy, after averaging $a_0(\epsilon)$ over all possible energies of positrons, one gets $\bar{a}_0 = 1/3$, which reflects the fact that positrons are dominantly emitted in the direction of muons spins, as stated before.

3.1.2 Positron Detection and Muon Decay Asymmetry

The experimental setup is schematically shown in Figure 3.3. As already mentioned, the only detectable particle in the experiment is the positron. Detectors are usually located near the
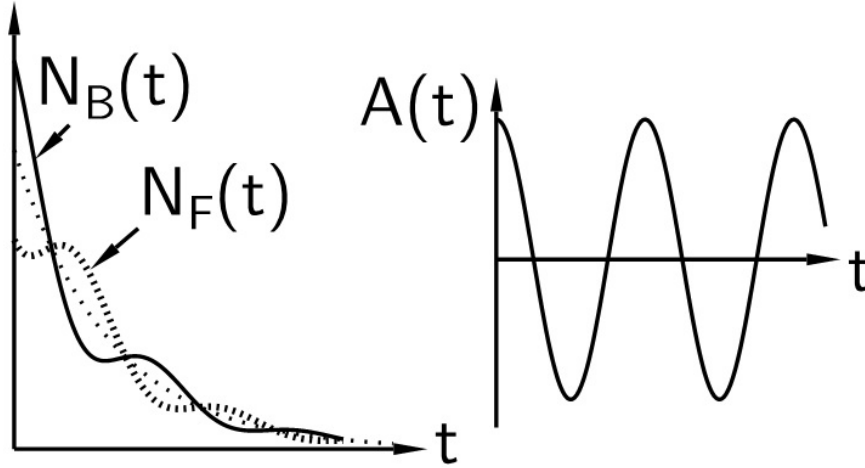
Figure 3.4: Asymmetry function
Number of positrons vs time detected by forward (F) and backward (B) detector if a
small transverse field is applied (left). Corresponding asymmetry function 3.4. (right)

sample so that they cover a large solid angle around the sample. In such a way the number of
positrons which escape without detection is minimized. Detectors are made out of plastic scin-
tillators that produce light which is then guided to photomultiplier using lightguides. Usually
there are two sets of Helmholtz coils around the sample space which can produce a magnetic
field in x or y direction (so called transverse field (TF) setup) or z direction, when magnetic
field points in the direction of incident muon beam (longitudinal field (LF) setup). We will not
go further into the technical aspects of experiment.

Let us assume that a small transverse field is applied, and for simplicity that there are no
internal magnetic fields inside the sample. If a muon decays immediately after its implantation
into the sample (time $t = 0$), the emitted positron will most probably be detected by the back-
ward detector. For $t > 0$ the muon spin precesses around the applied field and after some time
it will point towards the forward detector, then again towards the backward detector and so on.
The time evolution of the number of positrons in backward and forward detectors $N_B(t)$ and
$N_F(t)$ are shown in Figure 3.4. The average exponential decay reflects the finite lifetime of the
muon. After defining $N_B(t)$ and $N_F(t)$ we can track the time evolution of the muon polarization
through the asymmetry function (assuming perfectly symmetric detectors):

$$A(t) = \frac{N_B(t) - N_F(t)}{N_B(t) + N_F(t)}. \tag{3.4}$$

The normalization to the sum of the number of detected positrons allows us to elegantly cancel
out the exponential decay of muon number e^{-t/τ_μ}. We end up with a function that directly links

muon spin direction with experimentally measurable asymmetry $A(t)$ (see Fig. 3.4).

Due to intrinsic asymmetry of muon decay and efficiency of detectors for positrons with different energies, maximal asymmetry turns out to be around $A_{Max} \approx 25\%$.

The time resolution of the experiment depends on the source of proton (and later muon) beams. There are two types of facilities: continuous sources of protons and "pulsed" sources which produce bunches of protons.

Continuous facilities deliver protons at a constant rate in time. When a muon enters the detector a clock is triggered and time is running until positron is detected, then the next event can take place. The main advantage of this method is high time resolution (100 ps), which allows high magnetic fields to be measured. A drawback of this method is that it is hard to measure long lived muons because after the first muon started the clock, the second tends to come in the sample. Such event must be disregarded since one is not able to distinguish whether the detected positron came from the first or the second muon. This can be improved by use of electrostatic deflectors which prevent a second muon from entering in the sample until the positron is detected, however statistics at longer times remains poor.

Pulsed beam facilities ensure that the proton beam consists of a series of bunched pulses. Typical width of the pulses is ≈ 80 ns, which puts an upper limit on the time resolution. Fast relaxation rates in case of strong fields cannot be measured. However, now one can measure long living muons and slow relaxation up to ≈ 20 μs.

3.1.3 Muons in Magnetic Materials

The large magnetic moment of the muon ($3.18\mu_p$, where $\mu_p = 1.41 \times 10^{-26}$ J/T is the magnetic moment of the proton) makes it an ideal local probe to measure small magnetic fields (down to 10^{-5} T) in materials. Muons stop in the sample and each signal contributes to asymmetry proportional to its volume fraction. That makes muons a useful probe even in samples where there are several phases, or when the magnetic state is inhomogeneous.

Let us consider a muon stopped in a magnetic sample. It "feels" a local magnetic field $\mathbf{B}$ forming an angle θ with respect to its initial muon spin $\mathbf{s}_\mu(0)$. Such a configuration is shown in figure (3.5). The muon starts to precess around the magnetic field $\boldsymbol{B}$ with the Larmor frequency $\gamma_\mu B$. The normalized positron decay asymmetry function will be:

$$A(t)/A_{max} = \cos^2(\theta) + \sin^2(\theta)\cos(\gamma_\mu B t), \qquad (3.5)$$

where $\gamma_\mu = 851.37$ Mrad·s^{-1}·T^{-1} is the gyromagnetic ratio of the muon. If the magnetic field
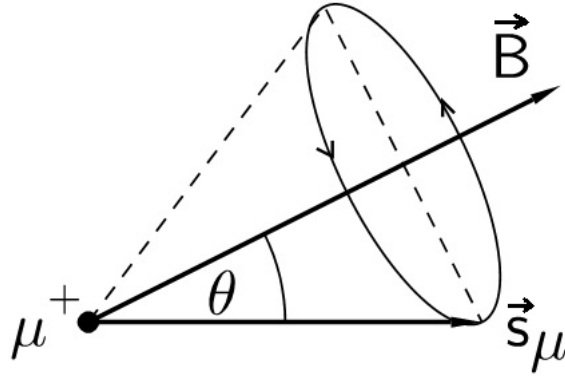
Figure 3.5: Muon precession

Muon spin precesses $\mathbf{s}_\mu$ around the local magnetic field **B**, where θ is the angle between the local field and muon spin.

is randomly oriented, which is always the case for powder samples, after averaging over all possible directions θ one gets:

$$A(t)/A_{max} = \frac{1}{3} + \frac{2}{3}\cos(\gamma_\mu B t). \tag{3.6}$$

To describe the situation in real materials we can take into account a possible distribution of magnetic field strengths. Muons situated at places with different local magnetic field strengths are precessing with different frequencies which is shown in Figure 3.6a. In case of a dense network of magnetic centers, according to the central limit theorem, the magnetic field strength is distributed according to a gaussian distribution of width Δ/γ_μ around zero:

$$P(B) \propto e^{-\frac{\gamma_\mu^2 B^2}{2\Delta^2}} 4\pi B^2. \tag{3.7}$$

After averaging $\int_0^\infty A(B,t)P(B)dB$ one gets:

$$A(t)/A_{max} \equiv g(t) = \frac{1}{3} + \frac{2}{3}e^{-\Delta^2 t^2/2}(1 - \Delta^2 t^2), \tag{3.8}$$

which is the well known Kubo-Toyabe function [59]. This relaxation function is shown in Figure 3.6b and represents the sum of functions shown in Figure 3.6a. Initially, the relaxation function starts as a cosine, then a minimum is reached after which the Kubo-Toyabe function recovers to its average value 1/3 which is usually called a "$\frac{1}{3}$-tail"- a clear signature of a static magnetic state. Such relaxation is found in some spin glasses, but also accounts for nuclear magnetization which is static on muon timescale.
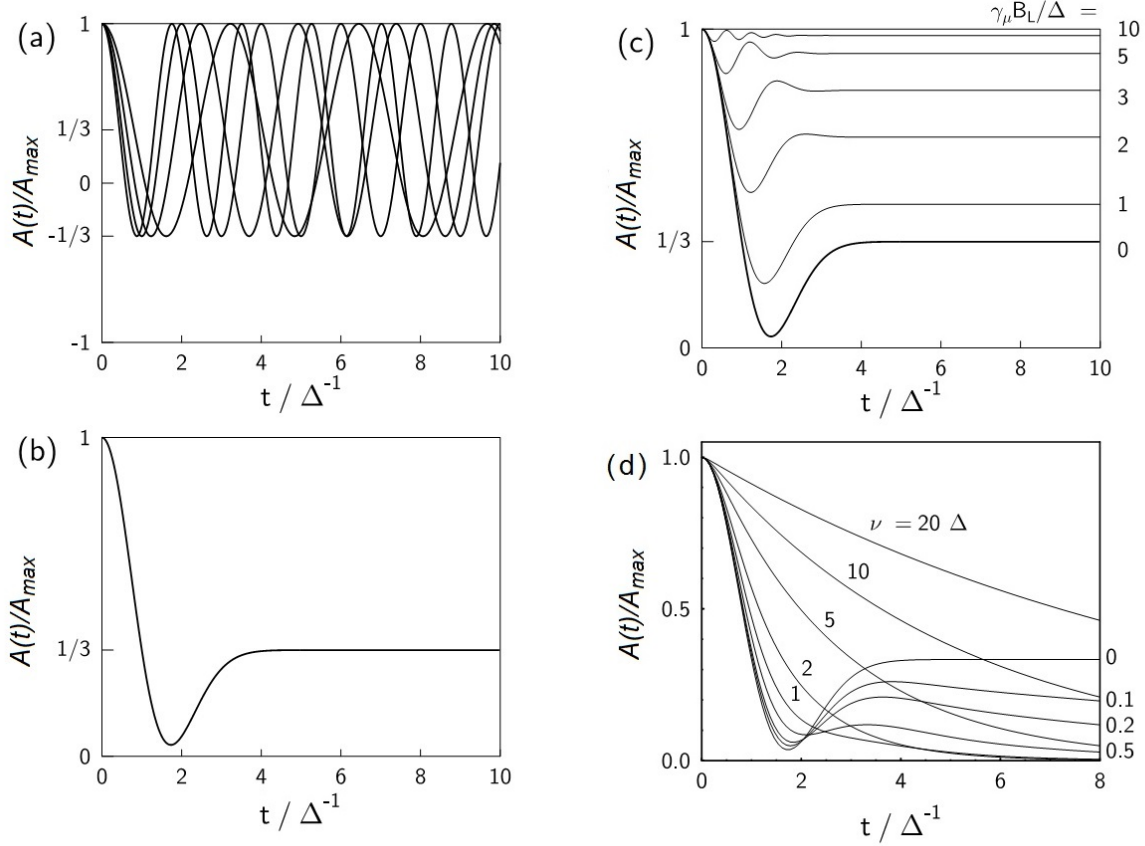
Figure 3.6: Origin of Kubo Toyabe function

a) Muons stopping at different sites will feel slightly different magnetic fields. As a result they will start to precess with slightly different frequencies so dephasing starts to take place. b) Asymmetry function is equal to the static Kubo-Toyabe function, which is obtained as a sum of the functions shown in panel a). The function has a characteristic dip, after which it reaches a constant value of 1/3. c) Relaxation of asymmetry when a longitudinal field is applied. For high fields the asymmetry stays close to unity. d) Asymmetry function is equal to a dynamical Kubo-Toyabe function $G(t, \nu, \Delta)$ for different values of ν. In case of a small degree of fluctuations ($\nu < \Delta$) only the 1/3 tail is affected. If fluctuations dominate over static field distribution, the relaxation becomes exponential. [58]

It is also worth considering relaxation in the case of an applied magnetic field along z axis. The distribution of an internal magnetic fields in x and y direction (perpendicular to the applied field) remains intact, but the distribution in the z direction is shifted; from zero to the applied

field B_L:

$$P(B_{x,y}) = \frac{\gamma_\mu}{\sqrt{2\pi}\Delta} e^{-\frac{\gamma_\mu^2 B_{x,y}^2}{2\Delta^2}}$$

$$P(B_z) = \frac{\gamma_\mu}{\sqrt{2\pi}\Delta} e^{-\frac{\gamma_\mu^2 (B_z - B_L)^2}{2\Delta^2}}. \tag{3.9}$$

After averaging equation (3.6) with respect to equations (3.9) one gets:

$$\frac{A(t)}{A_m} = 1 - \frac{2\Delta^2}{(\gamma_\mu B_L)^2}(1 - e^{-\frac{1}{2}\Delta^2 t^2}\cos\gamma_\mu B_L t) +$$

$$+ \frac{2\Delta^4}{(\gamma_\mu B_L)^3}\left(\int_0^t e^{-\frac{1}{2}\Delta^2 \tau^2}\sin(\gamma_\mu B_L \tau)d\tau\right). \tag{3.10}$$

Relaxation functions for several ratios $\gamma_\mu B_L/\Delta$ are plotted in Figure 3.6c. We can see that applied fields boost the "$\frac{1}{3}$ tail" to higher values, and for high fields (compared to Δ/γ_μ) the asymmetry remains close to unity, and does not change in time. The relaxation is said to be "fully decoupled" by the applied field.

So far we have considered relaxation which originates from static properties, i.e. field distributions. Now we also consider relaxation arising from dynamical properties (fluctuations). Let us assume that muons experience sudden changes (fluctuations) of local magnetic fields, after which the local fields are randomly distributed without correlation to the field directions before the change. If fluctuations occur at a rate ν, we can write:

$$\langle B(t)B(0)\rangle = \langle B^2(0)\rangle e^{-\nu t}. \tag{3.11}$$

The total dynamic relaxation function $G(t, \nu, \Delta)$ at time t will have contributions of muons that did not experience fluctuation up to time t ($g^{(0)}(t)$), muons that experienced one fluctuation up to the time t ($g^{(1)}(t)$), two fluctuations ($g^{(2)}(t)$) and so on...

The relaxation of muons that did not experience any fluctuations is simply a product of their fraction $e^{-\nu t}$ and static Kubo-Toyabe function $g(t)$

$$g^{(0)}(t) = e^{-\nu t}g(t). \tag{3.12}$$

The relaxation of muons that experienced "one" fluctuation at time t_1 is given by:

$$g^{(1)}(t) = \int_0^t \nu dt_1 e^{-\nu(t-t_1)}g(t-t_1)e^{-\nu t_1}g(t_1), \tag{3.13}$$

νdt_1 represents the fluctuation probability between t_1 and t_1+dt, $e^{-\nu t_1}g(t_1)$ describes relaxation before fluctuation at t_1 and $e^{-\nu(t-t_1)}g(t-t_1)$ relaxation after fluctuation. One needs to integrate

the entire expression since fluctuations can occur at any time between 0 and time t. For higher number of fluctuations the relaxation is described by:

$$g^{(n)}(t) = \int_0^t \nu dt' g^{(n-1)}(t-t')g^{(0)}(t'), \qquad (3.14)$$

Finally, the dynamical Kubo-Toyabe function is given by:

$$A(t)/A_{max} \equiv G(t, \nu, \Delta) = \sum_{n=0}^{\infty} g^{(n)}(t). \qquad (3.15)$$

This equation is usually calculated numerically and its shape is shown in figure (3.6d) for several values of ν (compared to Δ). For low fluctuation rates we see that only the $\frac{1}{3}$ tail is affected by fluctuations. For higher fluctuation rates the relaxation resembles an exponential function. At first it looks counter-intuitive that the relaxation becomes "slower" for higher fluctuation rates, but this effect comes from the so called "motional narrowing" because a muon feels an averaged field distribution which effectively decreases as fluctuations increase. In this limit, the relaxation $A(t)/A_{Max} = e^{-\lambda t}$ where $\lambda \propto 1/\nu$ in zero field and $\lambda \propto \frac{\nu}{\nu^2 + \gamma_\mu^2 B_{LF}^2}$, the so called Redfield [60] formula when a longitudinal field is applied.

It is worth emphasizing that one can clearly distinguish static and dynamic properties in materials. If one applies high longitudinal magnetic field (compared to Δ), relaxation in the absence of fluctuations will be close to unity. On the other hand, if fluctuations are responsible for the relaxation they will lead to exponential decay of asymmetry.

3.2   Nuclear magnetic resonance

Compared to μSR/neutron scattering experiments, which need muon/neutron sources and are available only in large facilities like RAL, and cost $\approx$1 billion euros, NMR experimental setups are much cheaper (on the scale of ≈ 0.5 million euros), and fit into a standard laboratory room.

Solid state nuclear magnetic/quadrupole resonance (NMR/NQR) is one of the few methods, together with already mentioned μSR, neutron scattering experiment, Mössbauer spectroscopy, electron paramagnetic resonance (EPR) and perturbed angular correlations (PAC) method which are known as "local probe". They measure microscopic effects (local) inside the materials, rather than measuring macroscopic net properties. The advantage of NMR (and related NQR) is that powder samples of just a few milligrams can be measured. It is especially convenient when a high magnetic field needs to be applied because the sensitivity increases quadratically with the applied field. NMR can detect various phases present in the same material, its inhomogeneities,
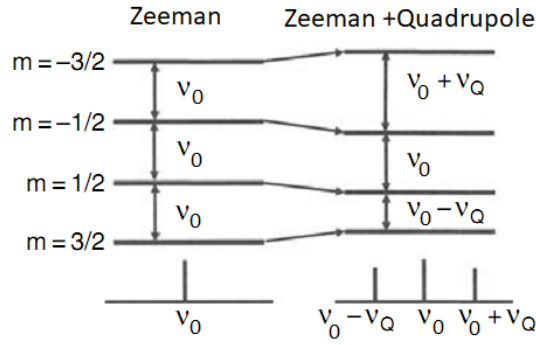
Figure 3.7: NMR levels

By applying an external magnetic field $\mu_0 H_0$, the degenerate nuclear spin ground state splits into four equidistant levels (for spin $I = 3/2$), with energy difference $h\nu_0$ (if one has a single crystal). Only one line at frequency ν_0 appears. If quadrupole interaction is present as well, it changes the spacing between levels and the spectral line splits into three, with difference in frequency $\pm\nu_Q$

and it can often distinguish and enable separate studies of impurity contributions from the clean part of the sample. Also, tiny gaps in the excitation spectrum down to a few mK can be detected. The main disadvantage compared to neutron scattering is a lack of sensitivity in k space, which is only partially mitigated if there are several NMR active nuclei in a unit cell and/or by using specific structures of the hyperfine coupling in the Fourier space.

In the NMR experiment, nuclear magnetism is measured. However nuclear spins interact with the surrounding electrons, which indirectly allows us a view into the electron subsystem which in most cases determines solid state properties. Available observables are spectra, T_1 and T_2 relaxation times. We will explain their basics in the following subsections.

3.2.1 NMR Hamiltonian

In an NMR experiment we observe nuclei of nuclear magnetic moment μ and spin I. These 2 quantities are related through $\mu = \gamma \hbar I$, where γ is the gyromagnetic constant, specific for each NMR active nucleus (the ones that possess spin $I \geq \frac{1}{2}$). By applying a magnetic field $\mu_0 H_0$ in the z direction on a sample that contains nuclei with spin I, the Zeeman splitting gives rise to $2I + 1$ energetically equidistant levels as shown in Figure 3.7, for spin $I = \frac{3}{2}$. The coupling of the spin to the applied field H_0 usually defines the dominant term in the nuclear Hamiltonian $\hat{H}_0$:

$$\hat{H}_0 = -\gamma \hbar \mu_0 H_0 I_z. \tag{3.16}$$

Nuclei with spin $I > 1/2$ are not spherical, but elliptical, so if there is some charge distribution which creates an electric field gradient V_{EFG} at the nuclear site, it couples to the quadrupole moment of the nuclei which is parametrized with the spin operators. This introduces a quadrupolar term in the nuclear Hamiltonian:

$$\hat{H}_{EFG} = \frac{eQ}{4I(2I-1)}[V_{zz}(3I_z^2 - \mathbf{I}^2) + (V_{xx} - V_{yy})(I_x^2 - I_y^2)]. \tag{3.17}$$

Here $V_{\alpha\beta} = \frac{\partial^2 V}{\partial x_\alpha \partial x_\beta}$ are the components of the EFG tensor. Initially equidistant Zeeman levels change their energies. In the special case when the z principal axis of the EFG tensor coincides with the direction of the applied magnetic field, the new energy levels are shown in the right part of Figure 3.7.

The third part of the Hamiltonian, which is usually most interesting in electron spin systems, is the magnetic coupling between nuclei under inspection and the surrounding electrons:

$$\hat{H}_{el-n} = -\gamma\hbar \sum_i I_\alpha A_{\alpha\beta}^i g\mu_B S_\beta^i, \tag{3.18}$$

where S_β are the spin operators of the electron subsystem and $A_{\alpha\beta}^i$ is the hyperfine coupling tensor. Here we point out that in paramagnetic materials the average value of $\langle S_\beta \rangle$ is zero when external magnetic field is not applied. The sum over i goes over all the electrons which interact with the given nuclei. We can in principle distinguish two different contributions: orbital coupling with neighboring electron, which is temperature independent and interaction with unpaired electron spins which is temperature dependent. In general, coupling with unpaired spins can be due to the dipolar interaction $D_{\alpha\beta}$ or/and through transferred hyperfine interaction $T_{\alpha\beta}$. In addition, these tensors (which add up into $A_{\alpha\beta}$) are multiplied with gyromagnetic constant ($g \approx 2$) which can in principle also be a tensor. Resolving these different contribution in the experiment requires measurements on single crystals so all directions can be measured. In the most simple case equation 3.18 is related experimentally to the NMR shift

$$K = \frac{\nu - \nu_0}{\nu_0}, \tag{3.19}$$

which measures local susceptibility. Also, NMR measurements alone are usually not enough to distinguish these contributions, one needs input from the following techniques: EPR, magnetic susceptibility measurements (SQUID or VSM) and NMR, together with numerical simulations. A superb analysis of such contribution is given in ref [46].

3.2.2 NMR measurement

The application of a static magnetic field $\mu_0 H_0$ in the z direction introduces Zeeman splitting, as previously said. At finite temperature T, the level occupation is given by the Boltzman distribution and nuclear magnetization in the z direction appears. The sample under study is located inside the coil whose axis is perpendicular to the applied field H_0. Through the coil a short pulse of current at frequency $\nu_0 = \gamma\mu_0 H_0$ through the coil creates a magnetic field H_x, and introduces an additional term in the spin Hamiltonian $\hat{H}_{pulse}$:

$$\hat{H}_{pulse} = -\gamma\hbar\mu_0 H_x I_x \cos(2\pi\nu_0 t). \tag{3.20}$$

Here H_x is magnetic field in x direction and I_x the component of spin angular momentum in x direction, with freedom to chose the x axis arbitrarily. The component I_x can be written using raising and lowering operators as $I_x = \frac{1}{2}(I_+ + I_-)$, so the Hamiltonian $\hat{H}_{pulse}$ can be regarded as a perturbation to the Hamiltonian in equation 3.16, which creates transitions between nuclear spin levels.

As soon as the magnetization M and field H_0 are not parallel, magnetization will start to precess around the field H_0 with angular frequency $\omega_0 = 2\pi\nu_0$. It is more convenient to follow the magnetization in a frame of reference that rotates with the same angular frequency ω_0, because we only have to consider the effects of the pulse field $H_x \cos(\omega_0 t)$. The field H_x is now static in the rotating frame and causes rotation of the nuclear magnetization M around x axis:

$$\frac{d\mathbf{M}}{dt} = \mathbf{M} \times (\gamma\mu_0 \mathbf{H}_x). \tag{3.21}$$

After time Δ, the angle of rotation of the magnetization around the x-axis is $\theta = \gamma\mu_0 H_x\Delta$. In the experiment it is important to determine Δ for which $\theta = \pi/2$ and $\theta = \pi$, these pulses are referred to as $\pi/2$ and π pulse.

The principle of measurement in an NMR experiment is the following. After we have applied a $\pi/2$ pulse around the x axis, the magnetization points towards the y direction. The magnetization starts to precess around the z axis. The same coil is used to apply the pulse and pick up the signal from the sample. The precession of the magnetization creates a change of flux in the coil which creates voltage. However it is not possible to use the coil for detection until transient effect from the pulse have decayed. Due to local inhomogeneities in solid samples, the spins feel some field distribution, so some precess faster and some slower than the frequency ν_0, which leads to loss of coherence. This is known as free induction decay (Fig. 3.8) and occurs during time T_2^*. This time can be shorter then the transient time in solid samples. This problem
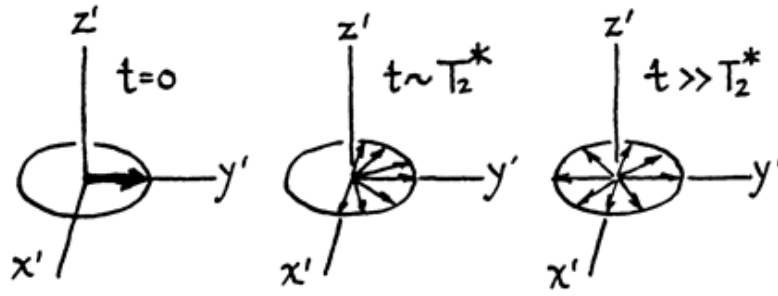
Figure 3.8: Free induction decay

Dephasing of nuclear magnetization after $\pi/2$ pulse around x axis in rotating frame of reference (x',y',z') [61]. Immediately after the $\pi/2$ pulse magnetization point in y' direction (left figure). Due to local inhomogeneities, magnetization starts to dephase on a timescale of T_2^*(central figure). When time t is larger then T_2^* loss of coherence is complete (right figure).

was first mitigated by Erwin Hahn. If another π pulse is applied in the x direction after the first $\pi/2$ pulse, the magnetization will refocus at time 2τ in the $-y$ direction. This is called the echo (Fig. 3.9).

Usually, due to magnetic broadening, the intrinsic width of NMR spectra in magnetic samples is wider than the frequency width of the pulse $(0.6/\Delta_\pi)$, i.e. to obtain full spectra one has to sweep the frequency and sum the individual Fourier transforms of each echo. Typical $\pi/2 - \tau - \pi - \tau - echo$ sequence for measuring spectra is shown in Figures 3.9. and 3.10a. For broad spectra the irradiation frequency is swept in such a sequence. Spin-spin T_2 relaxation is measured in the same way, only instead of the frequency one changes the time between two pulses. From the fit of the integrated signal to the function $M = M_0 \exp(-t/T_2)$ one can extract T_2, the intrinsic spin-spin relaxation time.

Physically more intuitive and relevant is the so-called spin-lattice relaxation time T_1. This is a measure of the time in which the magnetization returns to its equilibrium - in the direction of the z axis. It is measured in the following way. First we apply an excitation π_x pulse in the x direction and flip the magnetization into the $-z$ direction, then we wait for a time τ_1 during which the magnetization is relaxing. Keep in mind, that we can measure the magnetization only in the $x - y$ plane because of the orientation of the coil. This is done by applying the standard Hahn echo sequence explained above. By varying τ_1 and fitting the integrated data to a function $M = M_0(1 - 2\exp(-t/T_1))$ we extract T_1. The sequence is known as inversion recovery and is shown in the Figure 3.10b. Another possibility for measuring T_1 is to use a saturation recovery
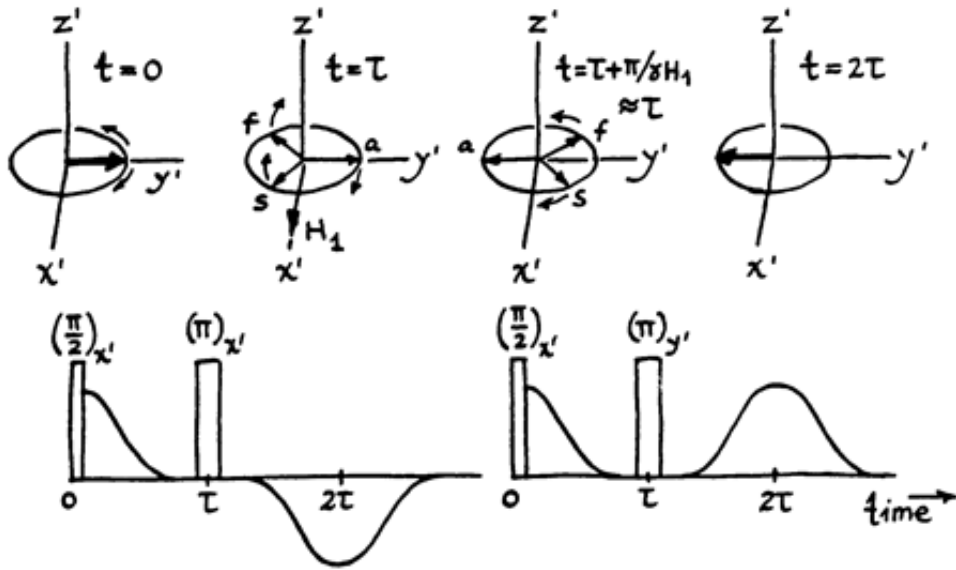
Figure 3.9: Hahn echo

Example of a Hahn echo sequence [61]. We follow magnetization in a rotating frame of reference (x',y',z'). Initially a $\pi/2_{x'}$ pulse is applied and magnetization is rotated from z' direction into y' direction. Then, dephasing starts to occur. Some nuclear spins are precessing faster(f) and some slower(s) than the average(a) depending on the local inhomogeneities. This is represented by arrows in the $x' - y'$ plane. If one at a time τ applies another $\pi_{x'}$ pulse, faster, slower, and average spins will be shifted in $x' - y'$ plane according to the third upper figure. Average magnetization will point into $-y'$ direction, while faster and slower spins will start to approach to the average value. At a time $t = 2\tau$ all nuclear magnetization will refocus at $-y'$ direction. If one applies second π pulse in y' direction, nuclear magnetization will refocus in the y' direction instead into $-y'$ one (bottom right figure).

sequence, where the initial pulse is not π, but $\pi/2$. The initial magnetization in z direction is not $-M_z$, but 0, so the fit function becomes $M = M_0(1 - \exp(-t/T_1))$.

In practice in NMR the signal to noise ratio is usually very small, so a large number of acquisitions needs to be averaged in order to get a good signal to noise ratio. Between each repetition one has to wait $\approx 5T_1$, for the magnetization to return to its equilibrium value before repeating the sequence. This makes NMR measurements time consuming.
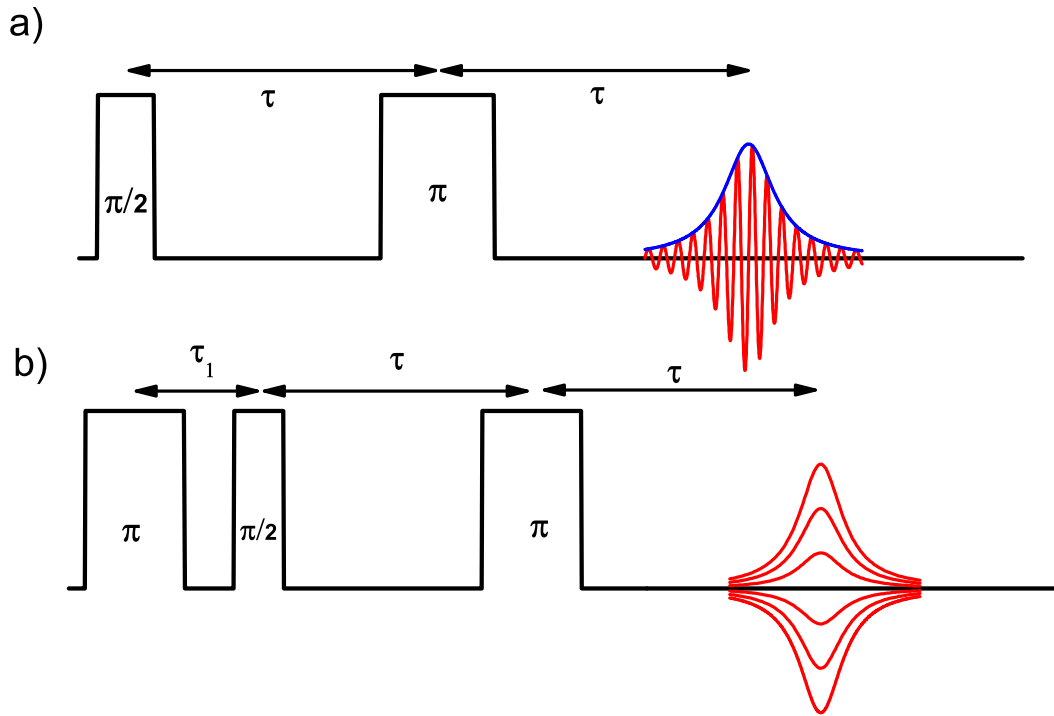
Figure 3.10: NMR sequence

Typical pulse sequence. a) $\pi/2 - \tau - \pi - \tau - echo$ sequence in the laboratory frame of reference, the signal is oscillating at the frequency ν. For measuring broad spectra frequency ν is varied, while for measuring T_2 relaxation time τ is varied. b) $\pi - \tau_1 - \pi/2 - \tau - \pi - \tau - echo$ sequence for measuring T_1 relaxation time (τ_1 is varied) in the rotational frame of reference. For small values of τ_1 magnetization (given by the integral of the echo) is inverted. As one increases τ_1 magnetization is returning to its equilibrium and for long τ_1 it reaches its full value.

3.2.3 Powder spectra

In Figure 3.7 we showed the simplest spectral shapes where there are three peaks, ideally delta functions, each corresponding to a transition between different levels. If one has a powder sample, and the nuclei under study have both anisotropic hyperfine coupling tensor and asymmetric EFG tensor, the spectra rapidly become complicated. In general, the resonant frequency then depends on the orientation between axis fixed in the crystal and the direction of the applied magnetic field $\mu_0\mathbf{H}_0$:

$$\nu = \nu(\cos\theta, \phi), \tag{3.22}$$
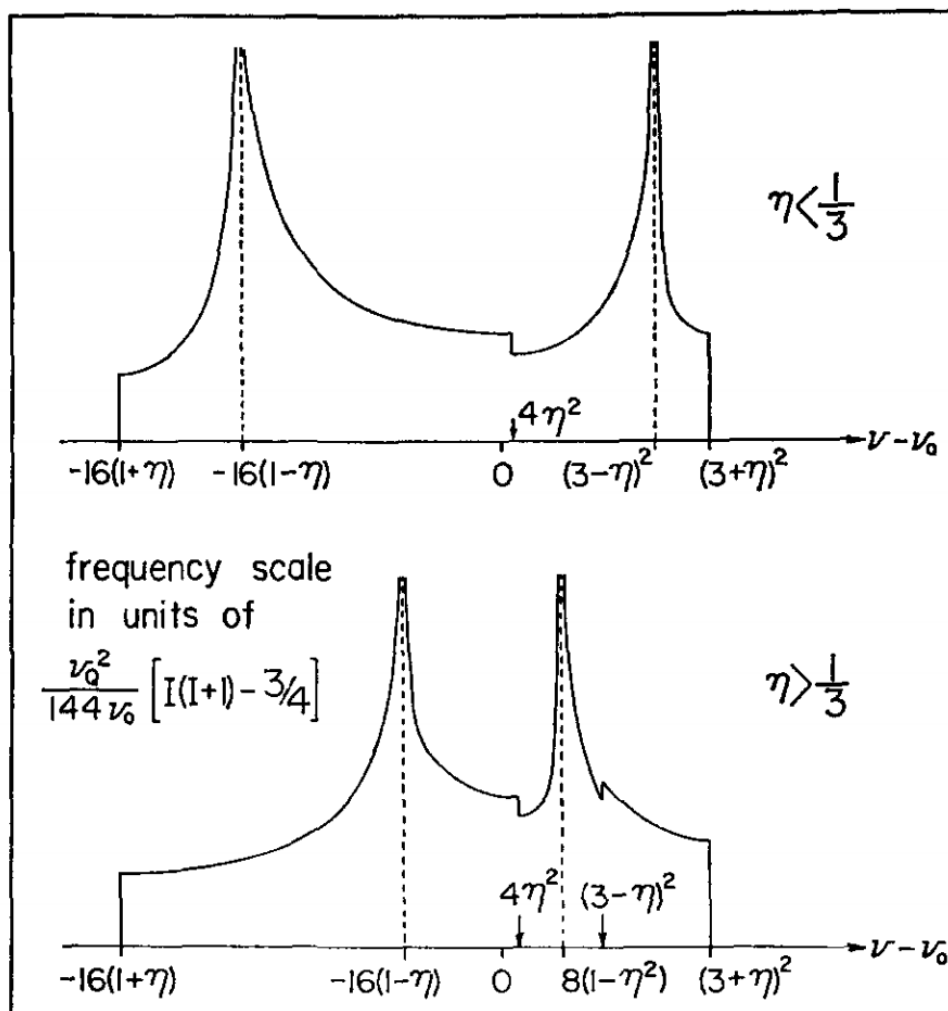
Figure 3.11: Central transition

Instead of a single delta function in single crystal case, if one has to deal with a powder sample, the central transition broadens and shows many features. Here, ν_Q is NQR frequency, ν_0 NMR frequency and η asymmetry parameter. Broadening occurs always with simultaneous loss of amplitude intensity. The integrals of the spectra are the same in both cases [62].

where θ and ϕ are polar angles which determine the directon between the local z' axis in the crystal and the direction of the magnetic field. The normalized powder spectra $P(\nu)$ are proportional to the probability that crystallites contribute to the "frequency window" between ν and $\nu + d\nu$:

$$P(\nu)d\nu = \frac{1}{4\pi}\int_{\nu}^{\nu+d\nu} \sin\theta d\theta d\phi, \qquad (3.23)$$

When $\hat{H}_{EFG}$ is treated as a perturbation to the $\hat{H}_0$, within first order perturbation theory one obtains the frequencies of the transition:

$$\nu_{m\leftrightarrow m-1} = \nu_0 - \nu_Q \left[\frac{3\cos^2\theta - 1}{2} - \frac{1}{2}\eta\sin^2\theta\cos 2\phi\right]\left(m - \frac{1}{2}\right), \qquad (3.24)$$

where $\nu_Q = \frac{3e^2qQ}{2I(2I-1)h}$ ($q \equiv 1/eV_{33}$) and $\eta \equiv \frac{V_{11}-V_{22}}{V_{33}}$; V_{ii} are the eigenvalues of the EFG tensor arranged in such a way that $V_{22} \leqslant V_{11} \leqslant V_{33}$. One notes, that the central transition frequency remains unchanged to first order in perturbation theory. If the quadrupolar interaction is strong, the central transition has to be treated up to second order of the perturbation theory, in which case it becomes [62]:

$$\nu_{1/2\leftrightarrow-1/2} = \nu_0 - \frac{R}{6\nu_0}[A(\phi)\cos^4\theta + B(\phi)\cos^2\theta + C(\phi)], \qquad (3.25)$$

where the constants, R, A, B and C are:

$$R = \nu_Q^2[I(I+1) - \frac{3}{4}], \qquad (3.26a)$$

$$A(\phi) = -\frac{27}{8} - \frac{9}{4}\eta\cos 2\phi - \frac{3}{8}\eta^2\cos^2 2\phi \qquad (3.26b)$$

$$B(\phi) = -\frac{15}{4} - \frac{\eta^2}{2} + 2\eta\cos 2\phi + \frac{3}{4}\eta^2\cos^2 2\phi \qquad (3.26c)$$

$$C(\phi) = -\frac{3}{8} + \frac{\eta^2}{3} + \frac{\eta}{4}\cos 2\phi - \frac{3}{8}\eta^2\cos^2 2\phi. \qquad (3.26d)$$

The shape of the powder spectra for the central transition is shown in Figure 3.11. However in case for lithium nuclei in our sample, treatment to the second order will not be necessary.

For magnetic materials, one can extract the most important information about the electron subsystem from the magnetic shift, related to the equation (3.18). For bare nuclei, in a magnetic field $\mu_0 H_0$ we expect the signal at frequency ν_0. In a material, the nuclei are surrounded by the electrons which are shielding nuclear spins, so the transition frequency is shifted: $\nu = \nu_0(1 - \sigma_{\alpha\beta})$. Shift values are typically small $10^{-2} - 10^{-5}$. If one again treats shielding in a powder sample as a perturbation to the Zeeman term (3.16), the frequency at which one observes the signal is:

$$\nu = \nu_0[1 - \sigma_{iso} - \sigma_{ax}(3\cos^2\theta - 1) - \sigma_{aniso}\sin^2\theta\cos 2\phi], \qquad (3.27)$$

39

where $\sigma_{iso} = \frac{1}{3}(\sigma_1 + \sigma_2 + \sigma_3)$, $\sigma_{ax} = \frac{1}{6}(2\sigma_3 - \sigma_1 - \sigma_2)$, $\sigma_{aniso} = \frac{1}{2}(\sigma_1 - \sigma_2)$ and $\sigma_1, \sigma_2, \sigma_3$ are the principal values of the tensor $\sigma_{\alpha\beta}$.

When taken into account simultaneously, quadrupole effects and anisotropic shifts, the spectra become increasingly complex.

3.2.4 Spin-lattice relaxation time T_1

So far we have considered some static properties of the material under study which are visible in the spectra. The NMR technique provides an insight into dynamic properties as well, through relaxation times, in particular the spin-lattice relaxation time T_1. As in the previous case, by observing the behaviour of the nuclei in the sample, we indirectly get information about the dynamical properties of the electron subsystem which usually determines "new" interesting properties of the material.

The basic idea is the following: by applying a pulse in the $x - y$ plane we rotate the nuclear magnetization out of equilibrium. It would stay there forever if there was no contact with the surroundings, which is commonly called "the lattice". One needs the lattice to produce fluctuations at the nuclear site in order for nuclear magnetization to relax to its equilibrium state. In magnetic materials, the "lattice" usually refers to the electron spin system. A connection between nuclear and electron subsystems is again ensured through formula (3.18), although different components of tensor A and spin projections (**I** and **S**) contribute to spectra and T_1 relaxation time, respectively. We first consider this through Fermi's golden rule:

$$W_{i \longleftrightarrow j} = \frac{2\pi}{h} |\langle i|H'|j \rangle|^2 \delta(E_i - E_j - \hbar\omega), \tag{3.28}$$

where $|i\rangle$ and $|j\rangle$ denote nuclear states, H' describes the perturbation that couples electronic spin fluctuations with nuclear transitions, E_i and E_j are energy levels of the nuclear states ($E_i - E_j = \hbar\omega_{NMR}$) and ω is the frequency of the fluctuation. Generally, magnetic moment of a particle is inversely proportional to the particles mass m: $\mu \propto \frac{1}{m}$. Since nuclei are ≈ 1000 times heavier then electrons, their transitions are at ≈ 1000 lower frequency than the single electron spin flips which are on the scale of 1 eV. This means that electronic spin fluctuations that couple to nuclei are usually the result of collective low energy excitations. Typical NMR measuring frequency is ≈ 100 MHz, which corresponds to ≈ 5 mK or ≈ 0.4 μeV. This obviously makes NMR a superb technique for observing even tiny gaps in magnetic systems (providing that the temperature is sufficiently low). It is worthy to emphasize that in NMR we are not exciting nuclear transitions which change angular moment L_N of nuclei whose energy is on the scale of

1 MeV, but only its spin.

For this work it is important to take a closer look at the equation (3.18), and its connection to (3.28). Nuclear states $|i\rangle$ and $|j\rangle$ are determined by the external field $\mu_0 H_0$ in the z direction. If the electronic fluctuations at nuclear site produce a field in the z direction ($B' \propto I_z$) the transfer integral $|\langle i|H_{el-n}|j\rangle|$ vanishes, so such fluctuations do not contribute to the relaxation process. On the other hand, if fluctuations produce a field in the $x - y$ plane, then $B' \propto \sum_\beta I_x A_{x\beta} S_\beta + \sum_\beta I_y A_{y\beta} S_\beta$ and $|\langle i|H_{el-n}|j\rangle|^2 \neq 0$, in matrix form:

$$\hat{H}_{el-n} = -\gamma\hbar g\mu_B \sum_i \begin{bmatrix} I_x & I_y & I_z \end{bmatrix} \begin{bmatrix} A^i_{xx} & A^i_{xy} & A^i_{xz} \\ A^i_{yx} & A^i_{yy} & A^i_{yz} \\ A^i_{zx} & A^i_{zy} & A^i_{zz} \end{bmatrix} \begin{bmatrix} S^i_x \\ S^i_y \\ S^i_z \end{bmatrix}, \qquad (3.29)$$

matrix elements A_{xx}, A_{xy}, A_{yx} and A_{yy} relate in-plane electron fluctuations with in plane field, while A_{xz} and A_{yz} allow coupling of an electron fluctuation in z direction with an in plane induced field. Existence of these nondiagonal terms is crucial for probing the QN phase with the NMR technique.

In order to give an idea how to construct a more familiar expression for T_1 known in the literature, we need to change from time-space domain into a frequency-wave vector domain by using Fourier transforms of hyperfine coupling tensor and the electron spin operators:

$$A_{\alpha\beta}(\mathbf{q}) = \sum_i A^i_{\alpha\beta} e^{i\mathbf{q}\mathbf{r}_i}, S_\beta(\mathbf{q}) = \frac{1}{\sqrt{N}} \sum_i S^\beta_i e^{-i\mathbf{q}\mathbf{r}_i}. \qquad (3.30)$$

The transfer integrals $|\langle i|H_{el-n}|j\rangle|$ then become linear combination of the electron spin correlation functions:

$$S^{\alpha\beta} = \sum_j e^{-ikj} \int_{-\infty}^{\infty} \mathrm{d}t e^{i\omega} \langle S^\alpha_j(t) S^\beta_0(0)\rangle_T, \qquad (3.31)$$

where $\langle \cdots \rangle_T$ denotes thermal average.

The transition probability $W_{i\leftrightarrow j}$ is connected with the spin lattice relaxation time T_1 through the relation $1/T_1 \propto W_{i\leftrightarrow j}$ [60]. It is common to express the spin operators S_x and S_y in terms of S^+ and S^-. After combining abovementioned relations and some algebra, one can derive well known expression for $1/T_1$:

$$\frac{1}{T_1} \sim \sum_k \left\{ \frac{|A^\perp_k|^2}{2}[S^{+-}(k,\omega) + S^{-+}(k,\omega)] + |A^\parallel_k|^2 S^{zz}(k,\omega) \right\}, \qquad (3.32)$$

where $A^\perp_k \propto A_{xx} + A_{yy}$ and $A^\parallel_k \propto \sqrt{A^2_{xz} + A^2_{yz}}$ [43] and $\omega = \omega_{NMR}$.

3.2.5 Experimental Setup

Typical experimental setup is shown in Fig 3.12. Liquid nitrogen is used for temperatures down to 77 K. For even lower temperatures ^{4}He is used, with a boiling point of 4.2 K at 1 bar. If
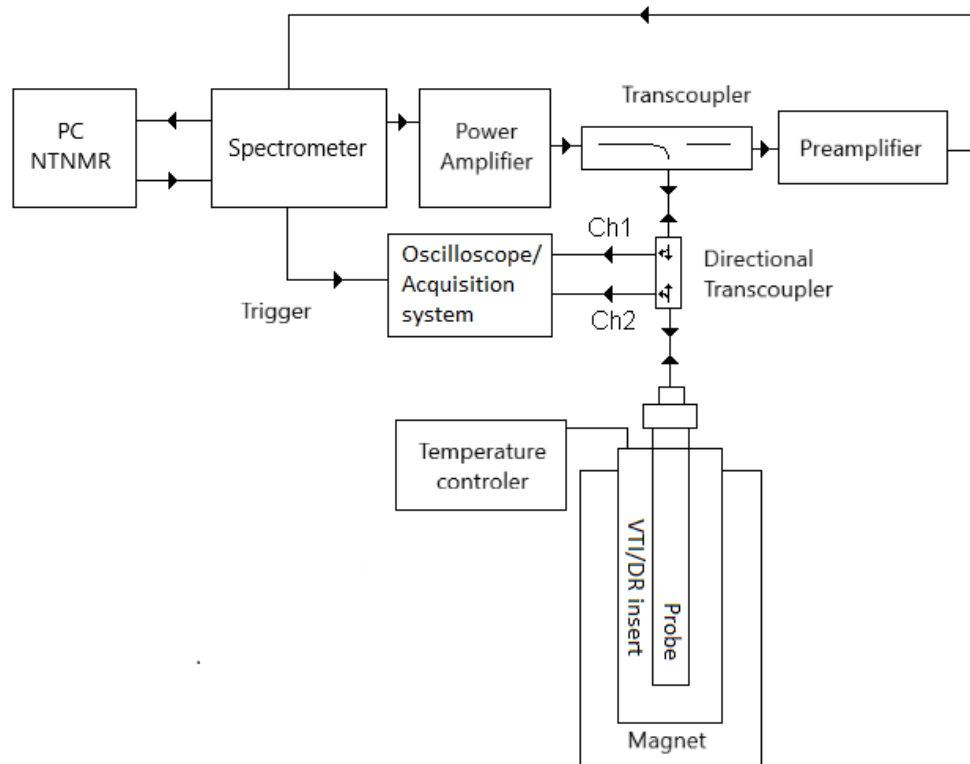
Figure 3.12: NMR setup

A PC, with appropriate software controls the spectrometer. Spectrometer with a highly accurate clock inside, sends RF signal (pulse) to power amplifier and simultaniously a TTL signal to trigger oscilloscope/acqusition board. The amplified pulse is guided throught transcoupler (or alternatively $\lambda/4$ cable) into the probe, preventing the signal to enter directly into preamplifier. The signal crosses through directional coupler, connected to the osciloscope, so one can measure both reflection and transmission (in and out of phase signal). The probe with its resonating circle is matched at 50 Ohms, and tuned precisely at the frequency where we expect the signal to appear. The probe is inserted into the VTI at the center of a superconducting magnet with very homogenous field (of the order of part per miliion (PPM) over a 1 cm^3). The temperature is controlled with a temperature controler, which is preferably in connection with a PC. For sub kelvin measurements instead of a VTI a dilution insert is placed into the magnet.

the pressure of the gas column above the liquid is lowered sufficiently, the temperature can be lowered down to ≈ 1.2 K. If one replaces ^{4}He for ^{3}He, and uses (in principle) the same setup, due to much higher vapor pressure of ^{3}He, one can reach ≈ 0.3 K. This does not seem like a big difference on linear scale, but we should have in mind that the "base temperature" for these two differ for a factor 4! The disadvantage of using ^{3}He is its increasingly high price which is ≈ 2500 euros per liter of gas at standard temperature/pressure.

3.3   Dilution refrigerator

Dilution refrigerator (DR) is an experimental setup which allows continuous measurements below 1 K, typically down to 30 mK or even lower. It uses a mixture of ^{3}He and ^{4}He isotopes, which shows some unexpected properties at low temperatures, due to quantum mechanics. Upon cooling below 870 mK, a phase separation between two phases occurs. The first phase is a concentrated ^{3}He phase which consist of almost pure ^{3}He, the second phase is a mixture of 6.6% ^{3}He and 93.4% ^{4}He, referred to as the dilute phase. To give a cartoon picture of how DR works, let us mention that ^{3}He is lighter and therefore has stronger zero-point motion then ^{4}He. If we also consider the attractive van der Waals forces between atoms, it means that ^{3}He "prefers" to be surrounded with ^{4}He, however, it will fill quantum states up to a point where the chemical potential of ^{3}He in the diluted phase equals the one of concentrated ^{3}He (because it is a fermion). This results in finite solubility of ^{3}He in ^{4}He. In practice, the dilute phase is below the ^{3}He concentrated phase. If one starts pumping on the dilute phase high energy ^{3}He atoms will start to leave the dilute phase due to higher vapor pressure, and the temperature is going to decrease. Then, since some quantum levels below the chemical potential are empty, new ^{3}He from the concentrated phase enters the dilute one, which allows for continuous cooling. Schematic of a DR is shown in Figure 3.13.

Technical problem of NMR experiments with a DR cooling option is that the power of NMR pulses is typically in kW, while the cooling power (dQ/dt) of DR is quadratically decreasing with the temperature of the mixture (T_{mc}) [63]:

$$\frac{dQ}{dt} = \frac{dn_3}{dt}(95T_{mc}^2 - 11T_3^2),\tag{3.33}$$

where n_3 is molar circulation of ^{3}He, and T_3 is the temperature of ^{3}He entering the concentrated phase. Typical cooling power of the DR at 30 mK is 50 mW. This means that one has to wait for a very long time before sending the next NMR pulse. In addition, all the leads (for pulses, temperature readings etc.) have to be grounded and well thermally anchored before entering

Figure 3.13: Dilution refrigerator

Simplified scheme of the DR (commercial ©Cryoconcept) used during this work in the operational mode. Before starting the experiment the mixture of ^{3}He and ^{4}He is held in the dump. We will skip the part where we explain the preparation of the experiment, which takes about a week, and just explain the steady state operation. In the DR insert (box on the right) in the mixing chamber ^{3}He concentrated liquid phase is above the dilute phase. One pumps ^{3}He from the dilute phase through the P.G.1 whose pressure is ≈ 1 mbar. After the pump there is a filter (preventing the oil gases to contaminate the pipeline). After the pump (P.G.2. shows ≈ 100mbar), ^{3}He passes through a compressor K which compresses the gas to ≈ 2 bars (monitored by P.G.3). Then it passes through charcoals (to eliminate possible air which would block the fridge), which are cooled with liquid nitrogen. ^{3}He (still in gas phase) enters into DR insert, it is first cooled down to 4.2 K by the ^{4}He liquid from the magnet space. This particular DR, has a Joule Thompson (JT) stage where precooled ^{3}He gas under pressure (2 bars) passes through a capillary and expands rapidly (pressure drops down to ≈0.5 bar and temperature to ≈1 K). Due to JT stage, there is no need of a 1 K pot in this DR. Before entering the mixing chamber, ^{3}He goes through series of high impedances made of fine silver powder, which are in thermal contact with cold ^{3}He which leaves the dilute phase. In such a way ^{3}He is eventually liquified into the ^{3}He liquid state, inserted into the mixing chamber, and the process starts again.

the mixing chamber. Electronics for detection is also specially made, with probing power of RuO_2 temperature sensor on the scale of pW in order to put minimal heat load on the mixing chamber. Taking all this in mind, albeit first commercial DR appeared in 1967, even these days it is a state of the art experiment.

3.4   Samples

The sample was prepared by authors of reference [41] from a stoichiometric mixture of predried Li_2CO_3, CuO and Sb_2O_5. Pellets were heated at 700 °C for 12 h, followed by a 24 h heating at 1000°C. Despite substantial efforts to grow single crystals, samples are available only in powder form.

Contrary to μSR experiments, where we used a simple powder sample, for NMR and magnetization measurements we prepared an oriented powder sample in the following way: first we ground the polycrystalline sample and mixed it with a slowly hardening epoxy glue. During hardening, the sample was rotated in a room-temperature-bore magnet of $\approx$ 7 T for 24 h. In such a way, the easy plane of the crystallites is forced to stay in the plane perpendicular to the
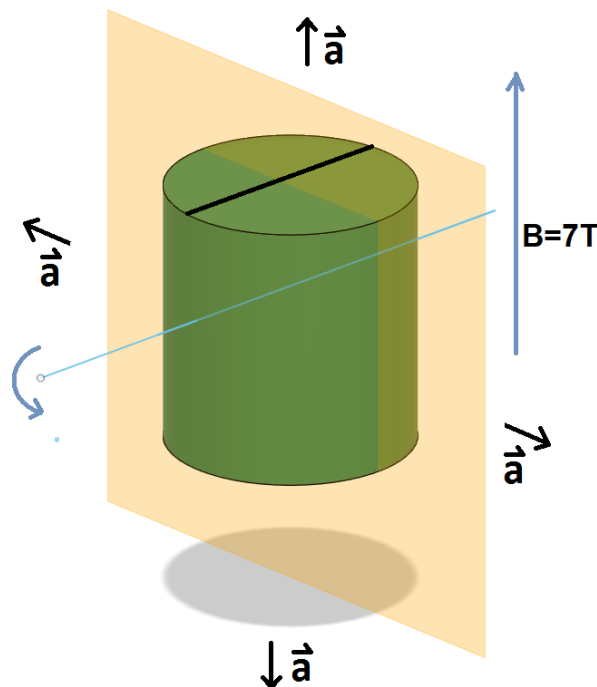
Figure 3.14: Rotation of the sample in the magnetic field during the hardening process. After the hardening, for NMR experiments, the field was applied along the rotation axis (black mark on the cylinder); perpendicular to the chain direction **a**.

rotation axis, as shown on Fig. 3.14 (yellow plane). The hard axis is then parallel with the rotation axis and marked on the sample (black line on Fig. 3.14). X ray measurements on the oriented powder have shown that the oriented hard axis is perpendicular to the a axis implying that the hard axis is in the bc plane.

Chapter 4

Results and Discussion

Results presented in this chapter were published in Bosiočić et al. [64].

4.1 μSR Measurements

The principal intention of μSR experiment was to check whether spin freezing occurs or not. Previous heat capacity measurements [41] were consistent with the absence of spin freezing in zero field down to 100 mK. However, signatures of static disordered states may be very weak in such measurements. Confirmation from a highly sensitive local technique like μSR is certainly needed. Experiments were performed on the MuSR spectrometer at ISIS (RAL,UK). For temperature control a cryostat with a dilution refrigerator (DR) insert was used. A powder sample of mass ≈ 1 g was mounted on a thin silver holder with drops of GE-varnish on the powder for better thermal contact.

In practice there is always some difference in efficiency between forward and backward detectors, the sample is never exactly in the center of the spectrometer etc. In order to compensate for these effects a slight experimental modification of equation 3.4 is needed:

$$A(t) = \frac{N_B(t) - \alpha N_F(t)}{N_B(t) + \alpha N_F(t)}, \tag{4.1}$$

where $\alpha \approx 1$ is a parameter which we need to estimate before each experiment. In order to do that, a small (20 G) transverse field is applied at high temperature, (in the paramagnetic phase) around which the muon spins precess. In figure 4.1 precession is shown for several values of α, with correct value $\alpha = 1.214$ chosen to give symmetric oscillations of the asymmetry around 0. All data were analyzed with WiMDA data analysis software [65].
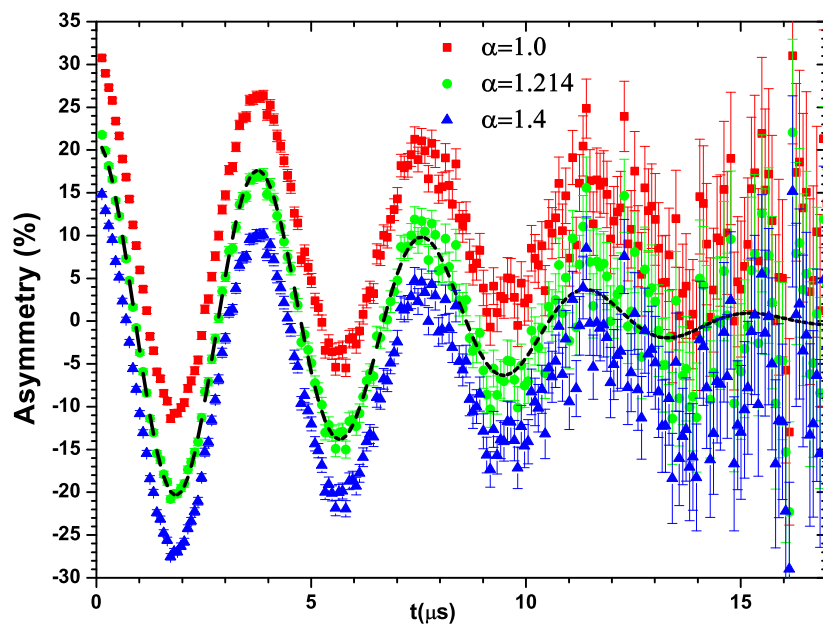
Figure 4.1: Determination of α coefficient.

For correct α value the asymmetry oscillates around x axis. A Gaussian envelope appears due to a distribution of the local magnetic fields. Black dashed line is a fit of the data to a oscillating function with Gaussian damping.
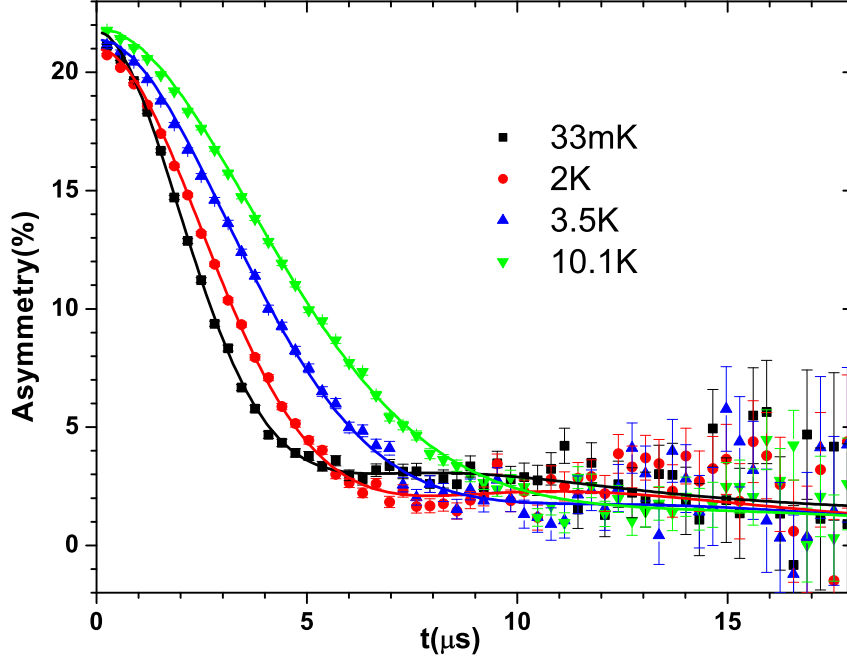
Figure 4.2: μSR relaxation spectra at different temperatures in zero field.

4.1.1 Zero field Measurements

In order to check whether spin freezing occurs or not, we followed the asymmetry decay from 10 K down to 30 mK in zero field. Corresponding histograms are shown in figure 4.2. For the fit function we used $A(t) = A_0 G(t, \nu, \Delta) + A_b$, where $G(t, \nu, \Delta)$ is the dynamic Kubo-Toyabe function.

At 10 K the main contribution to the asymmetry decay comes from nuclear moments, which are static on the timescale of the muon lifetime. The width of the field distribution is $\Delta/\gamma_\mu = 2.2$ G. At lower temperatures the width of the field distribution increases and reaches a plateau of $\Delta/\gamma_\mu = 4.3$ G below 0.7 K. We attributed this change to a small spin freezing of electronic moments. It is plausible to assume that muons stop near O^{2-} (all other ions are positively charged), which are ≈ 2 Åaway from Cu^{2+} sites. The crudest approximation in case of full ordering with $1\mu_B$ per Cu ion and dipolar coupling of muons would give a field $\mu_0\mu_B/(4\pi r^3) \approx 1160$ G at O^{2-} sites. With this in mind we can discard typical 3D order since observed fields are three orders of magnitude lower than expected in case of full ordering of spins at Cu^{2+} sites. It is possible that the small observed spin freezing reflects the existence of short range correlations as suggested in reference [41].
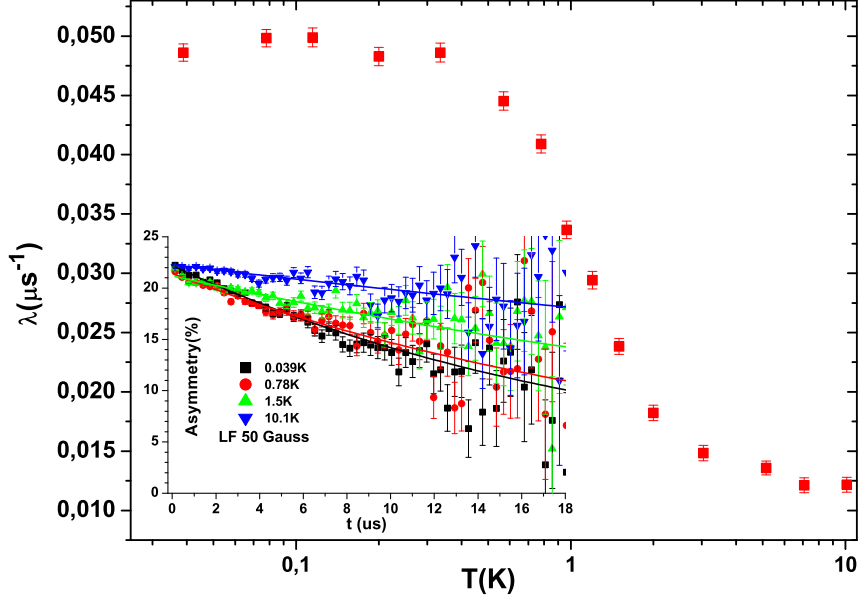
Figure 4.3: Temperature dependence of λ parameter.
Inset shows histograms with exponential fits (full lines).

4.1.2 Longitudinal Field Measurements

To better follow the changes in dynamical properties we applied a longitudinal field of 50 G to decouple the static fields and fit spectra to the function form:

$$A(t) = A_0 e^{-\lambda t} + A_b, \tag{4.2}$$

(inset of figure 4.3) where the intrinsic background contribution was estimated to be $A_b = 1.4\%$ from zero field spectra at 10 K with 100 million events, and fixed for all experiments with applied longitudinal field. The temperature dependence of the parameter λ is shown in figure 4.3. The increase in λ clearly signals a slowing down of the spin dynamics as if the system was approaching a transition around 1 K. However, instead of a divergence of λ and a decrease below 1 K, λ levels off indicating that slow fluctuations persist down to $T = 0$ K. This is a common feature of frustrated materials. It is worth noticing that λ changes by a factor of 5 from 10 K to 30 mK.

We also performed field-dependent measurements at 40 mK and 1.2 K. If the correlations decay exponentially, as $e^{-t/\tau}$ with a characteristic timescale τ, we can expect that the relaxation rate λ obeys the Redfield equation [60, 66]:

$$\lambda = \frac{2\gamma_\mu^2 \sigma^2 \tau}{1 + \gamma_\mu^2 B_{LF}^2 \tau^2}, \tag{4.3}$$
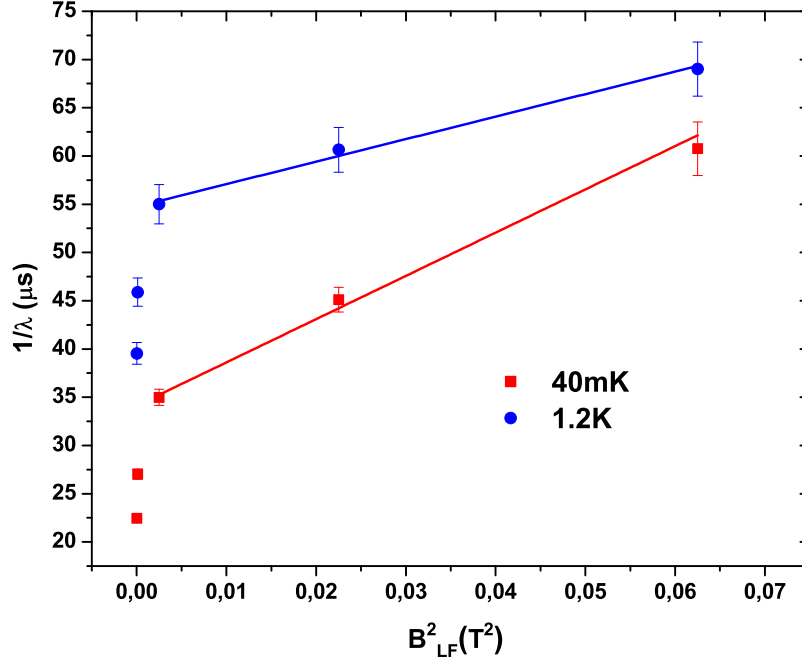
Figure 4.4: Field dependence of λ parameter

Full lines are fits to the Redfield equation.

where B_{LF} is the longitudinal applied field and σ the magnitude of the dynamical internal field. To make a more obvious comparison to the Redfield equation we plot λ^{-1} versus B_{LF}^2, we can see that the equation is satisfied for applied fields only above 50 mT. From the linear fits we extracted values for $\tau = 4.3(2)$ ps and $\sigma = 22(2)$ G at 40 mK and $\tau = 2.4(2)$ ps and $\sigma = 23(6)$ G at 1.2 K.

4.2 NMR Results and Low Temperature Susceptibility

The most suitable nucleus for NMR in LiCuSbO$_4$ is ^{7}Li due to high $\gamma/2\pi = 16.54607$ MHz/T. The spectra above 1.5 K were obtained using a $\pi/2 - \tau - \pi/2$ sequence with pulse length between $1.5\,\mu$s and $3\,\mu$s, and $10\,\mu$s in the dilution fridge. When the width of NMR spectra was larger than the pulse excitation width, the spectra were acquired by addition of Fourier transforms of the signal [67]. When precise field values were needed, a solution of LiBr in deionized water was used to determine the NMR reference frequency ν_0.

4.2.1 Li NMR Spectra at Room Temperature

Room temperature spectra for various magnetic fields, applied in the direction of rotation axis (hard axis), in range between 2.2 T and 7.5 T are shown in Fig. 4.5. At fields lower than $5\,\mathrm{T}$, the central line consist of contributions from two crystallographically different lithium sites Li(1) and Li(2). One of these sites has higher quadrupolar coupling, which is visible from two quadrupolar satellite peaks on the right and left with $\nu_Q = 47(1)$ kHz. The length of the $\pi/2$ pulse was optimized for the central transition, so the satellites lines are suboptimally excited and the theoretical ratio 3:4:3 of the central line and satellites intensities is not observed. The two Li sites have different hyperfine coupling, which is obvious when higher fields are applied: as seen in Fig 4.5. The central peak positions change, and the Li site with the smaller coupling begins to overlap with the right satellite of the more coupled site. From the quadrupolar effects, we have tried to assign the NMR lines to the different Li positions in the unit cell using a simulation of point charge distribution (Appendix A), and later more refined CASTEP calculations [68], but without conclusive results, maybe because of the distribution of the Li position.

The orientation of the oriented powder sample was checked by comparing NMR spectra measured with the magnetic field at different angles with respect to the hard axis. This was done by rotation of the oriented powder in magnetic field of 3 T as shown in Fig. 4.6. The quadrupolar satellites are most pronounced when the magnetic field is applied along the hard axis, i.e. the eigenvector of the EFG tensor which corresponds to the eigenvalue V_{zz} points in the direction of the hard axis, within an experimental error of $\approx 10°$. The inset of Fig. 4.6
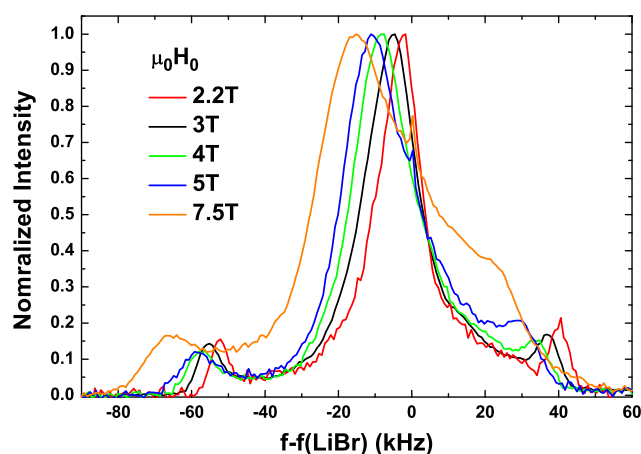

Figure 4.5: ^{7}Li spectra at 300 K in different magnetic fields (up to $7.5\,\mathrm{T}$). At lower fields one can resolve the quadrupolar satellites of the Li site with the higher quadrupolar coupling.
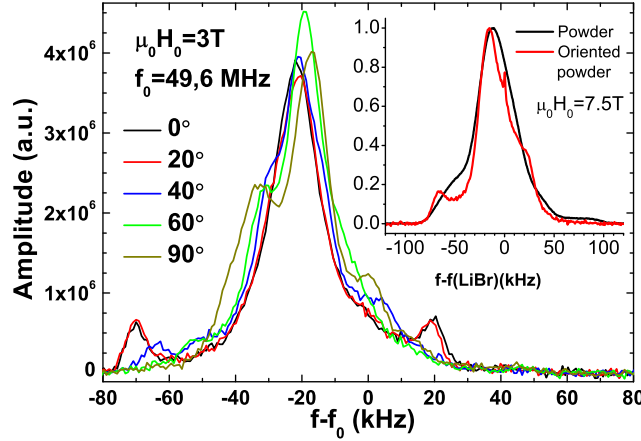
Figure 4.6: Angle dependent spectra, at $T = 300$ K and $\mu_0 H = 3$ T. Room temperature spectra at $\mu_0 H = 3$ T for different orientations of the applied field with respect to the hard axis. The quadrupolar splitting is the broadest when the applied field is parallel to the hard axis ($0°$). Inset: Unoriented vs. oriented powder spectrum measured in $\mu_0 H = 7.5$ T. The small peak at zero shift comes from the LiBr reference signal.

shows the difference between oriented and unoriented powder spectra in a magnetic field of 7.5 T. In the unoriented powder spectra, quadrupolar sites cannot be resolved. Two oriented powder samples were made, with the same spectra when magnetic field is applied along hard axis.

4.2.2 Low Temperature Magnetic Susceptibility

The magnetization and susceptibility of both, oriented and unoriented powder sample, prepared as previously described, were measured versus temperature in various magnetic fields in a commercial MPMS-XL7 Quantum Design SQUID magnetometer equipped with a ^{3}He insert for subkelvin measurements. In the lowest investigated field of 0.01 T, a small difference between the field cooled and zero field cooled susceptibilities is observed below about 15 K (see Fig. 4.7). This irreversibility is very weak in 0.1 T and disappears upon applying higher fields. The occurrence of some level of spin freezing in low field is consistent with the μSR data.

We have measured the low-temperature magnetic susceptibility of an oriented and unoriented powder in several magnetic fields (Fig. 4.8). For oriented powder, when the magnetic field is applied along the hard axis, a feature at $T = 0.7$ K appears in all curves, which points to a phase boundary. The feature is a minimum of susceptibility in low fields (1 T and 3.5 T), while a slight increase of χ is visible at 5 T and 7 T. These different kinks in magnetic suscep-
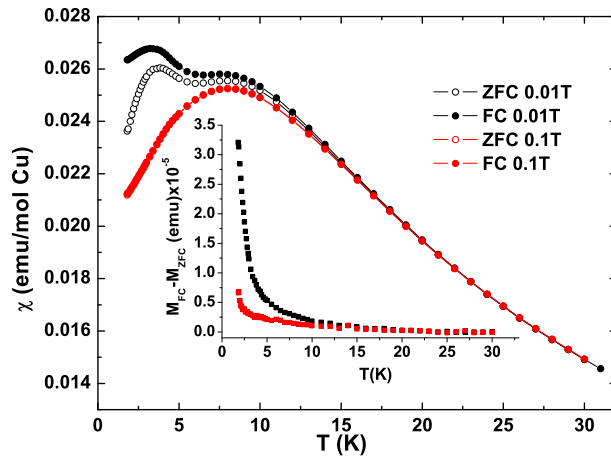
Figure 4.7: Low field susceptibility
Measurement on a non oriented powder sample. In the magnetic field of 0.01 T, FC
and ZFC susceptibility start to differ at 15 K. Upon increasing magnetic field this dif-
ference vanishes. Inset show differences between between FC and ZFC magnetization
curves in a 0.01 T (black) and 0.1 T (red).
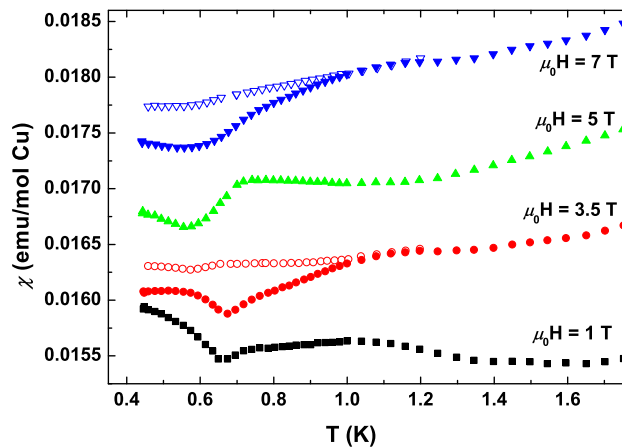
Figure 4.8: Low temperature magnetic susceptibility
Low-temperature magnetic susceptibility of the oriented powder LiCuSbO$_4$ with mag-
netic field parallel to the average hard axis (full symbols). The curves are shifted ver-
tically for clarity. Empty symbols: for comparison, susceptibility of the unoriented
powder sample at 3.5 and 7 T.

tibility point towards different phases i.e. there exist a phase boundary, if the field is increased
at constant temperature between 3.5 T and 5 T. Similar small changes in the signatures of the
transitions were observed in single crystal of linarite PbCuSO$_4$(OH)$_2$ and used to draw its com-
plex magnetic phase diagram. [53]. These kinks are even smaller for LiCuSbO$_4$, and easily
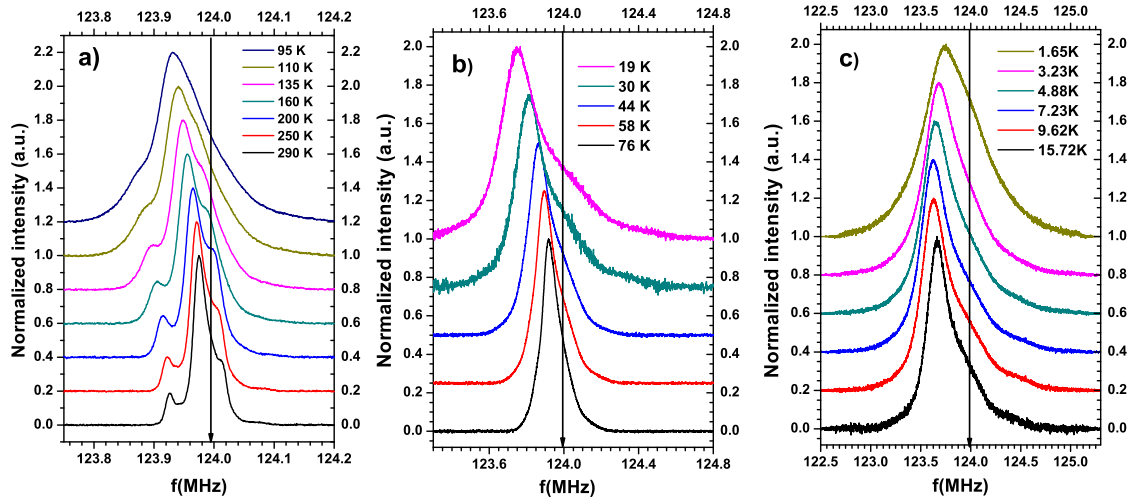
Figure 4.9: Spectra at $\mu_0 H = 7.5\,\mathrm{T}$ for different temperatures. Measurements on the oriented powder. The vertical lines denote the reference frequency ν_0.

overlooked in the unoriented powder sample (empty symbols in Fig. 4.8).

4.2.3 NMR Line Shift and Saturation Field

The dependence of the spectral lineshape on temperature at 7.5 T is shown in Fig 4.9. The spectral lines shift towards lower frequencies while simultaneously broadening. Quadrupolar satellites cannot be distinguished below $\approx$80 K. In order to check how the Li nuclei experience the magnetization increase of the electron subsystem in the paramagnetic state we compare the spectral shift $K = (\nu - \nu_0)/\nu_0$ (probing the local susceptibility) to the macroscopic susceptibility χ_{macro} measured by SQUID at similar fields respectively $7.5\,\mathrm{T}$ and $8\,\mathrm{T}$ (see Fig. 4.10), using the general relation:

$$K = A_{hf}\chi_{macro} + K_0 \ , \tag{4.4}$$

where K_0 is the temperature independent orbital shift, and A_{hf} is the hyperfine coupling constant. Despite the existence of two lithium sites, we were able to follow the shift consistently with temperature by following the position of the peak of the spectra, with a more significant contribution of the more coupled Li site (see below Fig. 4.11). Jaccarino plot in the inset of 4.10. Eq. (4.4), is valid for a large temperature range down to about 9 K, which provides the hyperfine couping constant value $A_{hf} = -0.57(2)$ kOe/μ_B and $K_0 = 0(6)$ ppm. Below 9 K, NMR shift and macroscopic susceptibility do not match any more. There are two possible

55
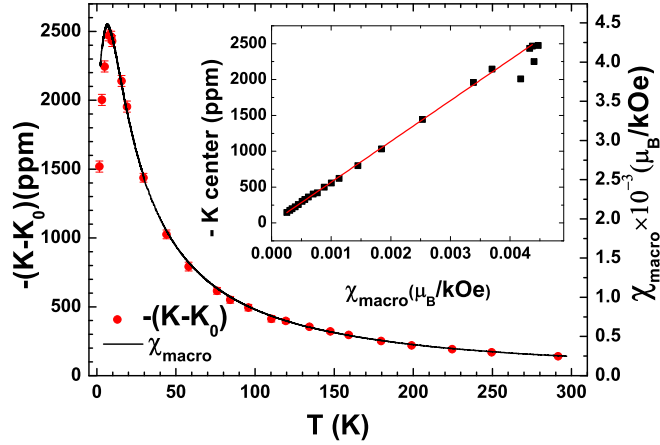
Figure 4.10: NMR shift and SQUID susceptibility
Temperature dependence of the NMR shift (red circles) and macroscopic SQUID susceptibility (line). Inset: The Jaccarino plot shows the dependence of the NMR shift on the macroscopic magnetic susceptibility measured at 8 T.

reasons for that: (i) NMR spectra and susceptibility were obtained on oriented and unoriented powders, respectively, (ii) a small amount of impurities or edge defects on chains can cause a Curie-like tail in χ_{macro}: these are contributing to the edge of the spectral line, not the peak position. However, the small difference between K and χ_{macro}, where both show a maximum, demonstrate the high quality of the sample and set an upper limit of the impurity concentration, such as Li/Cu or Sb/Cu intersite mixing, of 1%, in agreement with the structural refinement [41].

When the magnetic moment increases (either by applying a higher magnetic field or by lowering the temperature), the typical spectral shape resembles the one shown in Fig. 4.11 ($\mu_0 H_0 = 12\,\mathrm{T}$ at $1.55\,\mathrm{K}$). The spectrum is well described by a Lorentzian line for the strongly coupled site and a Gaussian line for the weakly coupled one. The ratio of their intensities is 55:45 in favor of the Lorentzian line. The contribution of the weakly coupled site to the amplitude of the main peak is $\approx 28\%$.

Below 1 K, the spectral shape changes and starts to be field dependent as shown in Fig. 4.12. The vertical line shows the maximum shift ($0.057\,\mathrm{T}$) of the peak position when $1\mu_B$ is frozen at the Cu site, as obtained from the hyperfine constant. The spectral width at 0.125 K is considerably larger than the one at 1.55 K in the corresponding fields. These broad spectra are obtained at fixed irradiation frequencies ν_0 by field sweeps around the reference field $\mu_0 H_0 = 2\pi\nu/\gamma$.

The spectrum at 5.2 T and 0.125 K, shows a squarish shape, typical for a magnetically ordered system in powder form, where all nuclei experience the same magnetic moment but
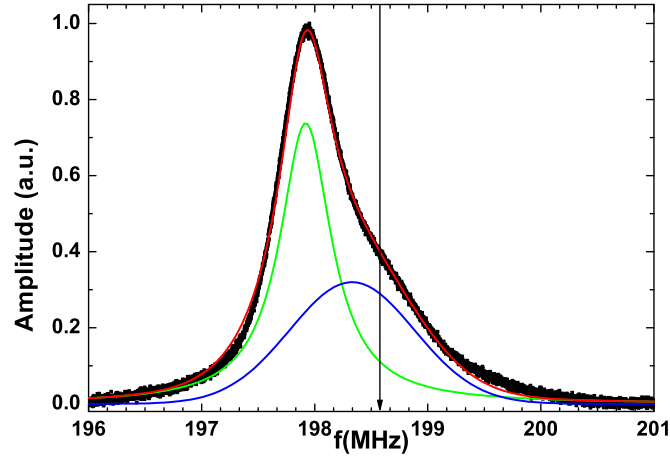
Figure 4.11: Spectrum at $T = 1.55$K in 12T field

Spectrum recorded at $T = 1.55$ K in magnetic field $\mu_0 H_0 = 12$ T (black). The red line is a simulation composed of a Lorentzian (green) and Gaussian (blue) line. Ratio of integrated intensities is 55:45 in favor of the Lorentzian line. The contribution of the Gaussian line at the main peak position is $\approx 28\%$. The vertical line shows the shift reference.
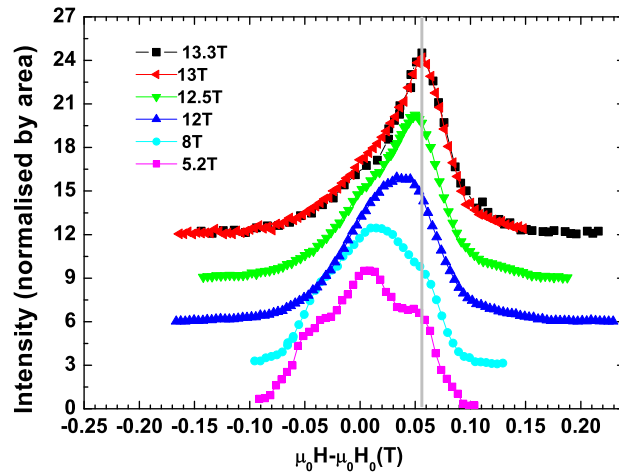
Figure 4.12: Spectra at T=0.125K

Spectra obtained by field sweeps at different frequencies ($\nu = \gamma \mu_0 H_0$) at $T = 0.125$ K. The vertical line represents the maximum hyperfine field of 0.057 T corresponding to $1\mu_B$ per Cu site This value was obtained independently from Jaccarino plot, hence, the peak positions of the spectra in saturation regime are right where we expect them to be. In 5.2 T and 8 T spectra are squarish in shape indicating SDW state. As the field increases, the system polarizes and the spectra narrow.

with different orientations with respect to the applied field (Appendix C). From the width of the spectra we estimate the moment on the Cu sites to be $\approx 0.75\ \mu_B$. The narrower component on the top of the squarish one is probably due to the site with smaller coupling.

With an increase of frequency, i.e. increase of external magnetic field, the spectra become narrower, and more shifted. This occurs due to the increase in polarization of the electron spin towards saturation where all spins point along the applied magnetic field. Spectra at 13 T and 13.3 T overlap, which implies that saturation is reached in that field range. The shift of the peak position in 13 T and 13.3 T is 0.057 T, which coincides perfectly with magnetic shift from the Jaccarino plot when $1\mu_B$ per Cu site is reached. These two independent arguments provide strong evidence that the system is saturated above 13 T in the ground state.

In previous work [41] (and section 2.4) the saturation field value of LiCuSbO$_4$ was estimated to be 12 T from the magnetization curve of bulk powder at 2 K (full red line in Fig. 4.13). The full saturation is not reached even at 16T most likely due to a too high temperature. Also, for bulk magnetization, an unoriented powder was used. These two facts prevented a precise determination of the saturation field which is crucial to explore the possible QN phase.

Alternatively, the magnetization curve can be determined from the peak shift of the ^{7}Li strongly coupled line (Fig. 4.12). The shift is proportional to the magnetization value, and the additional benefit is the use of oriented powder sample. The field dependence of the NMR shift at $T = 0.125\,\mathrm{K}$ is shown by full circles in Fig. 4.13. The maximum shift (i.e. local magnetization) is not reached at 12 T, but is saturated above 13 T. Compared to the bulk magnetization data taken at $T = 2$ K on unoriented powder [1], the increase of the NMR shift is much steeper around $12\,\mathrm{T}$.

In order to ascertain that we are probing the ground state of the electron system we measured the shift at 1.55 K. These data (squares in fig 4.13) correspond more closely to the macroscopic magnetization at 2 K. From all of the above arguments we conclude that the saturation field is above 12.5 T, probably slighty under 13 T. The full saturation is reached at $T =$0.125 K while the increased temperature and/or the lack of orientation smear out this transition at 2 K. Hence, we emphasize the advantage of NMR for the determination of the saturation field to investigate the local magnetization at very low temperatures, preferably on oriented powder.

4.2.4 Relaxation Measurements

Saturation recovery pulse sequence was used to measure spin-lattice relaxation times T_1. First, a saturation pulse was used (4-5 μs) which rotates the nuclear magnetization in the xy plane. Then
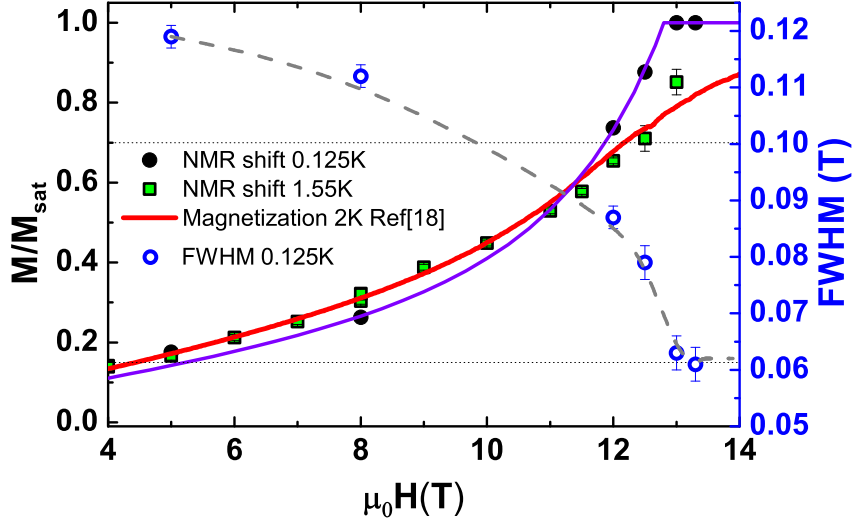
Figure 4.13: Shift and width of NMR lines
Field dependence of the NMR peak position at $T = 0.125$ K (black circles) and $T = 1.55$ K (green squares) compared to the bulk magnetization at 2 K from ref. [41] (red line). The purple line is a guide to the eyes for the $T = 0.125$ K NMR data. Right axis: FWHM of the spectra at 0.125 K (blue empty circles). The dashed line is guide to the eyes.

one waits for τ_1. In the meantime the nuclear magnetization starts to recover into z direction determined by applied magnetic field. At the time τ_1 an amount of nuclear magnetization in z direction is detected by standard solid echo sequence with 3 μs long $\pi/2$ pulses. Several relaxation curves are shown in Fig 4.14. In all fields below 12 T, and temperatures above 1.5 K, a single exponential recovery curve fits the data well giving a single T_1 (Fig. 4.14a – red circles). Above 12 T and below 5 K, the shape of the recovery changes and is not consistent with a single exponential function (Fig. 4.14a and c). This is due to the presence of different relaxation times for different frequencies (Fig. 4.14b), namely the left part of the spectrum (strongly coupled line) is relaxing slower than the right one. To take into account these different contributions of the two Li sites at the main peak position (see Fig. 4.11), we used a function of the general form:

$$1 - \frac{M(\tau_1)}{M_\infty} = ae^{-(\tau_1/T_1)^\beta} + (1 - a)f(\tau_1) \tag{4.5}$$

where M_∞ is the magnetization at equilibrium, a represents the contribution of the strongly coupled site, and is fixed to 0.72 from the analysis of the spectral shape in Fig 4.11, and $f(t)$ is the relaxation attributed to the weakly coupled site which is determined independently on the right
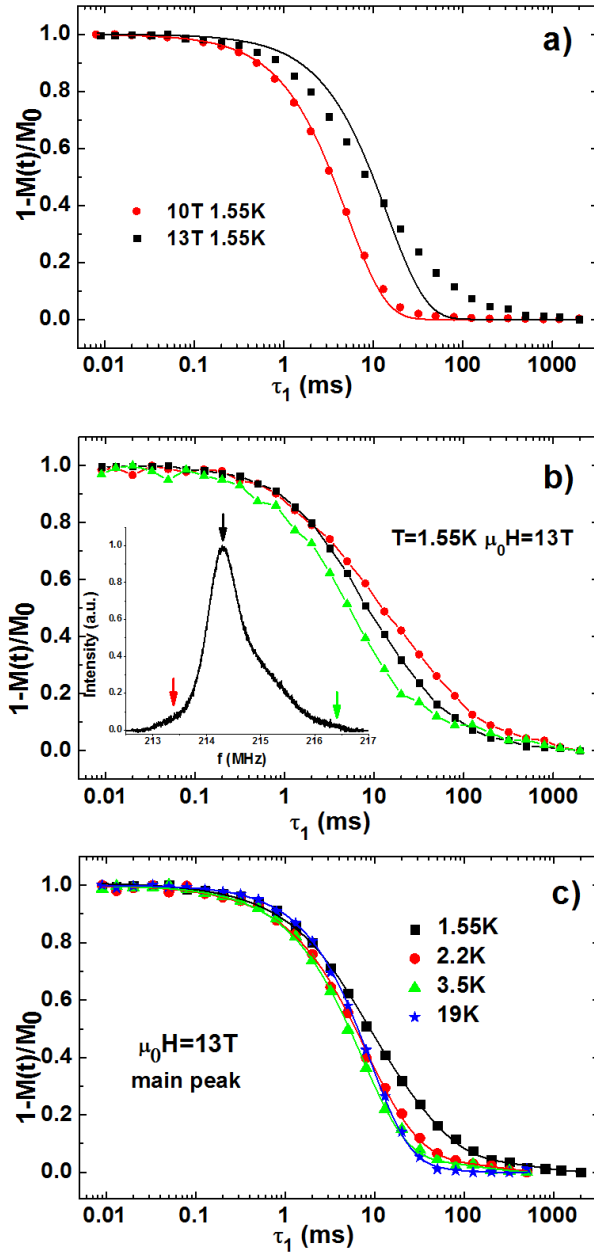
Figure 4.14: Relaxation curves
a) Spin-lattice relaxation (central peak) measured at $T = 1.55\,\text{K}$ at $\mu_0 H = 10\,\text{T}$ (red circles) and at $\mu_0 H = 13\,\text{T}$ (black squares). The lines are single-exponential fits; b) Relaxation of the magnetization at different parts of spectra at the temperature $T = 1.55$ K. Arrows on the spectra correspond to frequencies where relaxation was measured. Lines are guide for the eyes; c) Relaxation curves at the main peak at various temperatures. Full lines are obtained by the fit to Eq. (4.5).

side of the spectrum (see Appendix A). The temperature dependent stretch exponent $\beta < 1$ accounts for an increasing width of the local T_1 distribution at low $T < 5$ K (see inset Fig. 4.16b).

Such a distribution may be due to some local excitations which can be an intrinsic property of the chains or due to impurities (switching Cu with Li or Sb [41]) or defects (vacancies and chain edges). The upper limit for the impurity concentration is 1% so they can significantly perturb a dozen of neighboring spins differently [69–71], leading to a distribution of relaxation times and the appearance of stretched exponentials [72]. For β values around $\beta \approx 0.5$, width of relaxation rate distribution is on the order of magnitude [73].

We have measured the field dependence of T_1 at two different temperatures, $1.55\,\mathrm{K}$ and $4.6\,\mathrm{K}$ (Fig. 4.15). At $T = 1.55\,\mathrm{K}$ there is a peak in the relaxation rate $(1/T_1)$ around 6 T. From the local magnetization (NMR shift) in Fig. 4.13, we know that the magnetization is at $\approx 20\%$ of its saturation value M_s. Theoretical work by Sudan et al. [40, 74], predicts that at 20% of saturation magnetization a crossover from vector chiral to SDW_2 phase occurs. With this in mind, the above mentioned peak in $1/T_1$ could be related to the vicinity of VC-SDW_2 boundary.
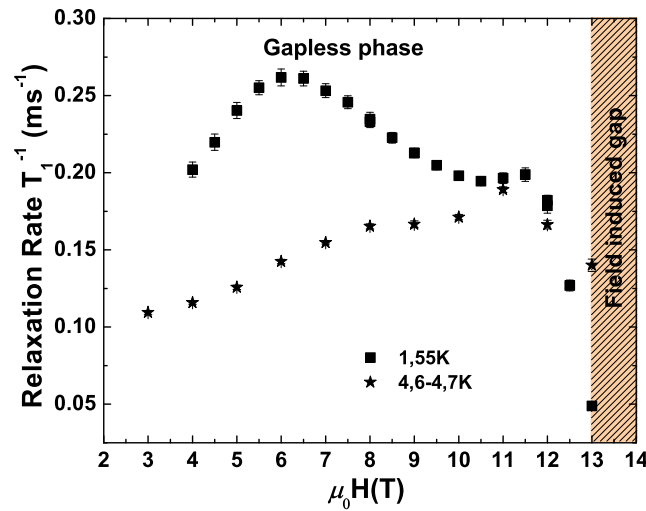
Figure 4.15: Field dependence of relaxation rate.
Field dependence of the relaxation rate at $T = 1.55\,\mathrm{K}$ and $T = 4.6\,\mathrm{K}$. The peak around $6\,\mathrm{T}$ at $T = 1.55\,\mathrm{K}$, may be a finite-temperature remnant of the crossover between the VC and SDW_2 phases. T_1 drastically changes above $\mu_0 H \approx 12\,\mathrm{T}$, and above $\mu_0 H = 13\,\mathrm{T}$ the system is in the field induced gap phase. Between $12\,\mathrm{T}$ and $13\,\mathrm{T}$ it is plausible to search for the existence of a QN phase.

A quadrupolar nematic phase is predicted above 70% of M_s. The magnetization curve is very steep in that region, and the QN phase would be expected to occur in the narrow range between 12 T and 13 T. This is a reason for dramatic change in $1/T_1$ above 12 T in Fig. 4.15. More specifically, from theory in strictly 1D systems, a magnetic transition only allowed at

$T = 0$ K, $1/T_1$ at very low temperatures should follow a power law $1/T_1 \propto T^{2K-1}$ in both SDW$_2$ and QN phases, with $K \in [0,1]$ being a field-dependent Tomonaga-Luttinger parameter [42,43]. The boundary between the two phases occurs at a field where $K = 1/2$, roughly when 70% of saturation magnetization is reached [40,42]. In SDW$_2$ phase ($K < 1/2$) one therefore expects a power-law divergence of $1/T_1$ at low temperatures, while for the QN phase ($K > 1/2$) a power-law drop towards zero is predicted. This should appear below ≈ 10 K where 1D is well defined. Above the saturation field, the system is gapped and $1/T_1$ should decay exponentially towards zero. With this in mind, we chose the fields of $\mu_0 H_0 = 4, 8, 12$ and 13 T to follow the temperature dependence of the relaxation rate (Fig. 4.16).

In $\mu_0 H_0 = 4$ T, where the VC phase is expected, $1/T_1$ shows traces of divergence down to 1.55 K with a critical exponent $1/T_1 \propto T^{-0.55(2)}$ ($K = 0.24(1)$). In $\mu_0 H_0 = 8$ T, where the SDW$_2$ phase is expected, $1/T_1$ shows a similar behavior down to 1.55 K with a critical exponent $1/T_1 \propto T^{-0.30(1)}$ ($K = 0.38(1)$). The exact values of K are sensitive to the range over which they are fitted, but it is clear that they monotonically increase with field, as theoretically expected [36]. Macroscopic magnetization measurements indicate that $\mu_0 H_0 = 12$ T is close to SDW$_2$/QN phase boundary. The temperature dependence of $1/T_1$ shows a broad maximum around 2.5 K which might indicate the proximity of the QN phase.

In $\mu_0 H_0 = 13$ T a maximum in the relaxation rate occurs at much higher temperature, around 6 K, but below 2.2 K the drop is too steep to be associated with a QN phase. If we take into account DR measurements, the critical exponent is $1/T_1 \propto T^{3.6}$, which would give a nonphysical value of $K = 2.3(1)$. A more likely explanation, consistent with the formerly discussed static measurements, is that the magnetization is already saturated at $\mu_0 H_0 = 13$ T, and the $1/T_1$ shows a gapped (exponential) behaviour. The 13 T data below 2.9 K were then fitted to the function $1/T_1 = C_1 exp(-\Delta/T) + C_2$, where $\Delta = 3.24(19)$ K, $C_1 = 0.396(47)$ ms^{-1} and $C_2 = 5.1(1.4) \times 10^{-5}$ ms^{-1}. The latter T-independent term likely accounts for the contribution of a tiny amount of impurities or defects. Hence, the temperature dependence of the spin-lattice relaxation time changes qualitatively and quantitatively in the narrow field range $12 - 13$ T, from a power-law divergence characteristic of the SDW$_2$ phase to a gapped behavior characteristic for the saturation regime.

Finally, the relaxation rate measured at a single temperature point $T = 0.125$ K in the field $\mu_0 H_0 = 5.2$ T gave a significantly longer T_1 (86 ms) than at 1.55 K, showing that there exists a maximum in the relaxation rate somewhere in between these two temperatures. As already noted, a peak in the heat capacity is observed at 700 mK, [41] which, together with an anomaly
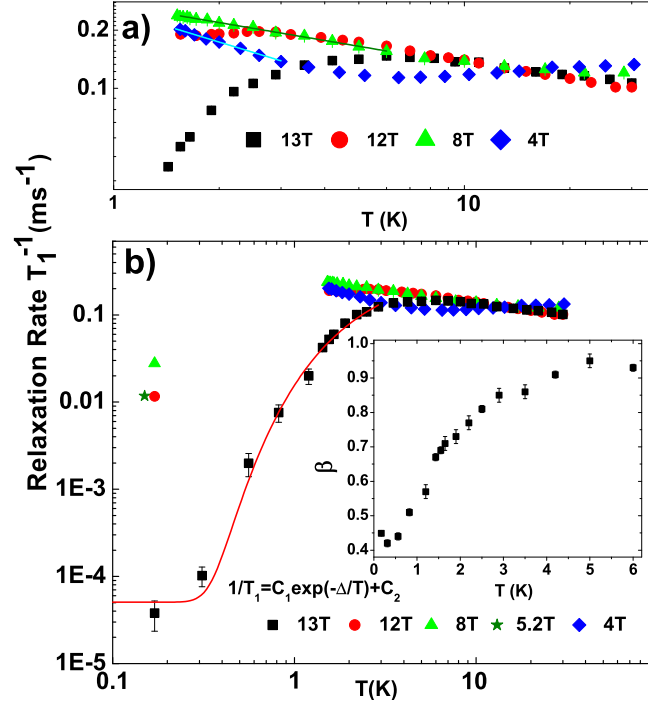
Figure 4.16: Temperature dependence of the spin lattice relaxation T_1^{-1}
(a) Temperature dependence of the spin lattice relaxation T_1^{-1} in magnetic fields $\mu_0 H = 4, 8, 12$ and $13\,\text{T}$. In $4\,\text{T}$ and $8\,\text{T}$ relaxation rate obeys power law behaviour down to $1.55\,\text{K}$ with critical exponents -0.55(2) and -0.27(1), respectively. At $12\,\text{T}$ and $13\,\text{T}$ a broad maxima appears, but the drop in $13\,\text{T}$ below $2.2\,\text{K}$ is too steep to be assigned to a QN phase. (b) Additional low temperature (DR) measurements down to 125 mK. 13 T data below 2.9 K were fitted to the function $1/T_1 = C_1 \exp(-\Delta/T) + C_2$, where $\Delta = 3.24(19)$ K, with $C_1 = 0.396(47)$ ms^{-1} and $C_2 = 5.1(1.4) \times 10^{-5}$ ms^{-1}. Inset: T-dependence of the stretched exponent β, indicating a broad distribution of relaxation times at low temperatures.

in the susceptibility measurements, may mark a phase transition causing the non-monotonous behavior of the relaxation rates.

4.2.5 Discussion

In the following, we discuss the various low temperature phases of $LiCuSbO_4$ in the light of known data from the present study and Ref. [41] and summarize our current understanding in the tentative phase diagram shown in Fig. 4.17. We will compare our results to recently published work by Grafe et. al. [1] and give a short overview on $LiCuVO_4$, a compound which has been
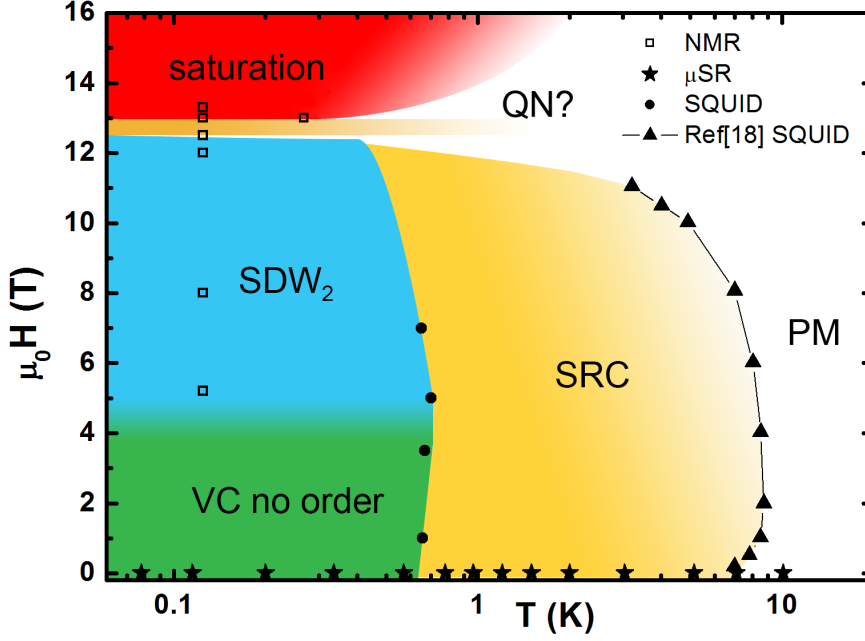
Figure 4.17: Low-temperature phase diagram of LiCuSbO$_4$.
Above 9 K, the system is in the paramagnetic regime (PM - white). As the temperature is lowered short range correlations (SRC) among neighboring spins appear (yellow). However, from the width of NMR spectra at temperatures down to 1.5 K at various fields (4 T, 8 T, 12 T, 13 T), one can clearly dismiss any kind of 3D order (these points are omitted from the phase diagram for clarity). Below 0.7 K, the system enters in a vector chiral (VC) regime with no static order in the fields up to $\approx$ 4 T. Above 4 T a crossover to an ordered SDW$_2$ phase occurs, as evidenced by NMR (blue). At high field and low temperature there is a narrow possibility for the existence of QN phase (orange), just below the saturation regime (red).

thoroughly investigated for more than two decades now. To label the various field-induced phases, we rely on the theoretical work by Sudan et al. [40]. From the latter study of frustrated spin chains, in LiCuSbO$_4$ with $J_1/J_2 = -2.22$, the magnetic excitations of $p = 2$ bound spin flips should govern the phase diagram. Several field-induced ground states are predicted: (i) a vector chiral phase (VC) for $M/M_{sat} < 0.15$, (ii) an SDW$_2$ phase for $0.15 < M/M_{sat} < 0.7$, and (iii) a QN phase for $0.7 < M/M_{sat} < 1$. Using the NMR shift at 0.125 K from Fig. 4.13 as a measure of the magnetization, one estimates that $M/M_{sat} = 0.15$ occurs at $\mu_0 H \approx 5\,\mathrm{T}$, $M/M_{sat} = 0.7$ occurs at $\mu_0 H \approx 12\,\mathrm{T}$, and $M = M_{sat}$ occurs at $\mu_0 H \approx 13\,\mathrm{T}$.

Vector chiral phase. From the μSR measurements, we drew the main conclusion that in the zero magnetic field, there are no traces of typical 3D magnetic ordering. Dutton et al. [41]

suggested that this may be due to the fact that adjacent chains are not parallel, but canted one with one respect to the other. These μSR data are labeled by stars in Fig. 4.17. Together with SQUID data (Fig. 4.8) in 1 T and 3.5 T, where a dip in magnetic susceptibility at 0.7 K is observed we can draw the boundaries of the VC phase (green area in Fig. 4.17). Above 5 T susceptibility shows a different shape of curve indicating a different magnetic phase than the VC one. Additionally, the heat capacity curves shown in in Figure 3b of Ref. [41] are similar at 0 and 2 T and evolve gradually only above 4 T with the growing of a peak around $T = 0.7$ K. Therefore the boundary between the two phases seems to occur between 4 and 5 T. The gradual evolution of the heat capacity suggest a crossover rather than a sharp transition from the VC phase to the SDW$_2$ phase.

The NMR spectra measured at $T = 125\,\mathrm{mK}$ in $\mu_0 H = 5.2$ T and $8\,\mathrm{T}$ (Fig. 4.12) clearly show that magnetic ordering has occurred. This is confirmed by specific heat measurements where a peak at $T = 0.7\,\mathrm{K}$ clearly indicates a transition in this intermediate field range. NMR relaxation measurements at $\mu_0 H = 8\,\mathrm{T}$ above the transition temperature show the temperature dependence $1/T_1 \propto T^{-0.30(1)}$ consistent with a SDW$_2$ phase (negative exponent less than 1). These results give strong indication that in the intermediate field range between $\mu_0 H \approx 5$, and $12\,\mathrm{T}$ the theoretically predicted SDW$_2$ phase is indeed stabilized by the magnetic field.

Possible quadrupolar nematic phase. NMR relaxation measurements at $\mu_0 H = 12\,\mathrm{T}$ show a negative slope above $T = 2.5\,\mathrm{K}$, consistent with SDW$_2$ phase, but below $T = 2.5\,\mathrm{K}$ the slope changes to positive which could be consistent with a QN phase (positive exponent less than 1). This behavior may point to the proximity of the crossover between SDW$_2$ and QN phases. Contrary to the SDW$_2$ phase, the QN phase should not broaden the NMR spectrum, which was recently pointed out by Orlova et al. [55] in LiCuVO$_4$ just below the saturation field. Inspection of Fig. 4.12 shows that the spectrum at $\mu_0 H = 12\,\mathrm{T}$ is narrower than the spectra at $\mu_0 H = 5.2\,\mathrm{T}$ and $8\,\mathrm{T}$, but still broader than the spectra at higher fields. This again points to the proximity of QN phase. The spectrum at $\mu_0 H = 12.5\,\mathrm{T}$ is narrower, consistent with the appearance of a QN phase. From the line shift, the magnetization $M/M_{sat} = 0.85$ is theoretically in the QN phase ($M/M_{sat} > 0.7$) but the QN phase could be pushed to even higher magnetization for systems with hard-axis anisotropy [74]. NMR relaxation measurements down to the lowest temperatures may help to decide whether the QN phase is present at this field. In any case the lower boundary of the QN phase should be close to 12.5 T. On the other hand at $\mu_0 H = 13\,\mathrm{T}$ the full saturation is reached, giving the upper boundary for the possible QN phase.

Saturation regime. When the saturation is reached one expects a gap in the excitation spec-

trum. This is confirmed by our relaxation measurements in the dilution refrigerator shown in Fig. 4.16.b which yield the gap value $\Delta \approx 3.2\,\mathrm{K}$ at 13 T. A theoretical model for the isotropic case [35] predicts the opening of the gap (ie the entrance in the saturation regime) when the ratio of the spin magnetic energy $\epsilon_s = g\mu_B\mu_0 H_s$ and the NNN interaction J_2 reaches $\epsilon_s/J_2 \approx 0.5$ which is in excellent agreement with our case (for g=2.21 [41] in field of $\mu_0 H_0 = 13\,\mathrm{T}$ $\epsilon_s = 18.2$ K while $J_2 = 34$ K). So far we have interpreted our results guided by the theory for isotropic $J_1 - J_2$ chains, while our compound possesses a small easy plane anisotropy (≈ 0.8) [41]. A detailed analysis of the phase diagram for such an anisotropic case is given in Ref. [74]. Easy plane anisotropy favors the vector chiral phase, but if the anisotropy is not pronounced, the QN phase may still exist in the high field regime. This is a possible reason why the QN phase is restricted to so narrow field range just below saturation. The presence of a small interchain coupling may further narrow the QN stability domain [75].

Grafe et al. [1] recently reported an extensive experimental and theoretical investigation of LiCuSbO$_4$. NMR measurements were performed up to 16 T on an unoriented powder sample, at temperatures down to 2 K, so the $T \to 0$ K phase diagram was not accessible. Nonetheless, in the temperature and field range common to our study, the NMR results are consistent. In particular at 13 T they also observed a gapped behavior of T_1, with a gap value $\Delta \approx 2.4$ K which is similar to our value. The main discrepancy with the present study is the determination of the saturation field which is of great importance in order to put an upper boundary on QN phase. In ref. [1], the magnetization curve obtained from macroscopic measurements using pulsed fields at 0.45 K did not reach saturation up to the highest measured field of 20 T (Fig. 4.18), which was interpreted as a signature of in-plane exchange anisotropy ($J_1^x \neq J_1^y$). In contrast, our NMR shift data point to a well defined saturation field close to $13\,\mathrm{T}$ and do not demand modifications of the magnetic model. Their tentative phase diagram is shown on Fig. 4.18.

For comparative purposes, it is worth here taking a look at the most investigated compound among $J_1 - J_2$ candidates, LiCuVO$_4$ [45]. This compound is available in the form of single crystals, which is a big experimental advantage, however it has quite high saturation field, above 40 T. The work of Svistove et al. [76] was the first (and for a long time, the only) investigation of the high-field regime. A small kink in the dM/dH curve was detected, as shown in the Fig 4.19 (a) and (b) in the 41-44 T field range. Several groups have reported follow-up investigations of different parts of LiCuVO$_4$ phase diagram [77–80], and a superb analysis of hyperfine coupling tensors was given in a paper by Nawa et al. [46], followed by a high field NMR study by Büttgen
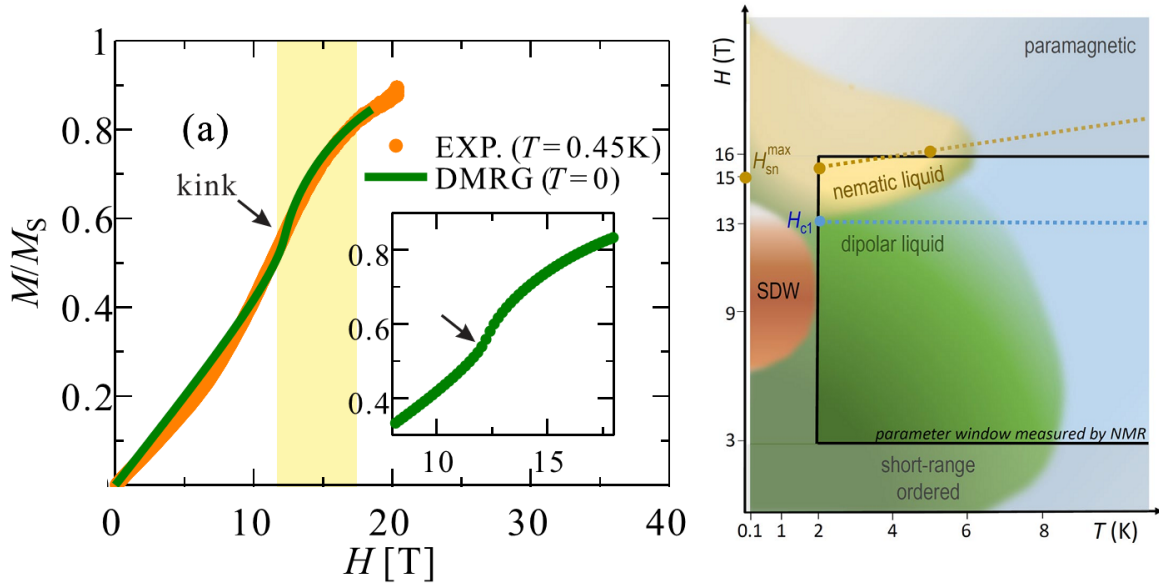
Figure 4.18: Magnetization and phase diagram of LiCuSbO$_4$
(Left) Magnetization Curve obtained by pulse fields at $T = 0.45$ K (orange), and the one calculated by DMRG at $T = 0$ K (green) (Right) Proposed phase diagram. (Both from ref. [1]).
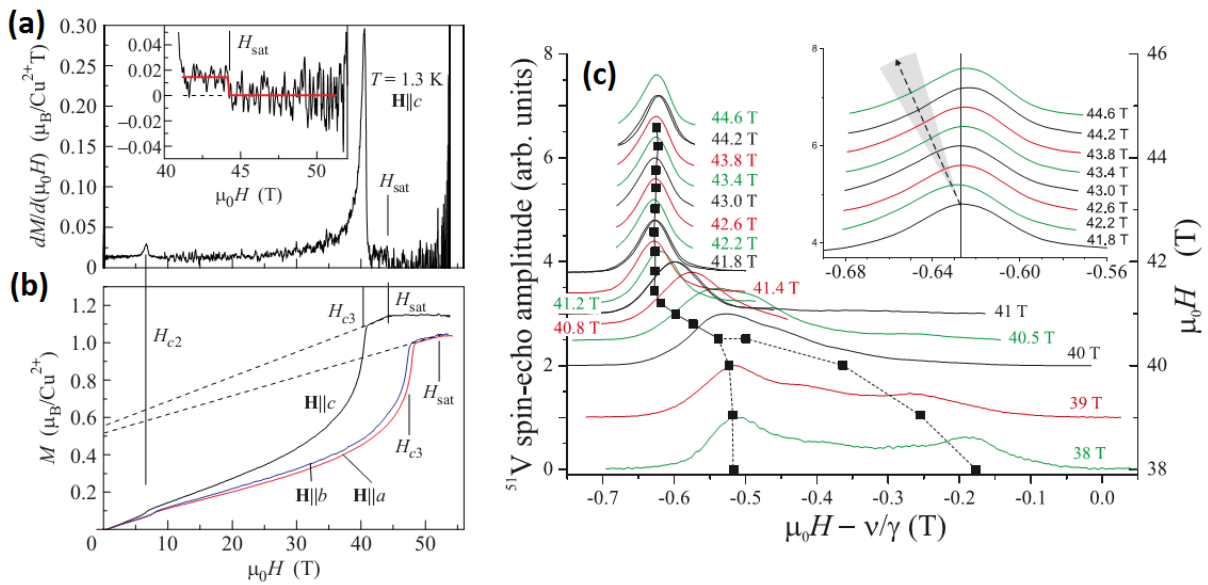
Figure 4.19: High field magnetization and shift of ^{51}V in LiCuVO$_4$
(a) dM/dH curve measured with a pulse field technique. (b) $M(H)$ curves at $T = 1.3$ K, obtained by integration of the curves shown in (a). A small region $H_{c3} < H < H_{sat}$ was related with the presence of quadrupolar phase [76]. (c) ^{51}V Spectra obtained at $T = 380$ mK in the high field region [47].
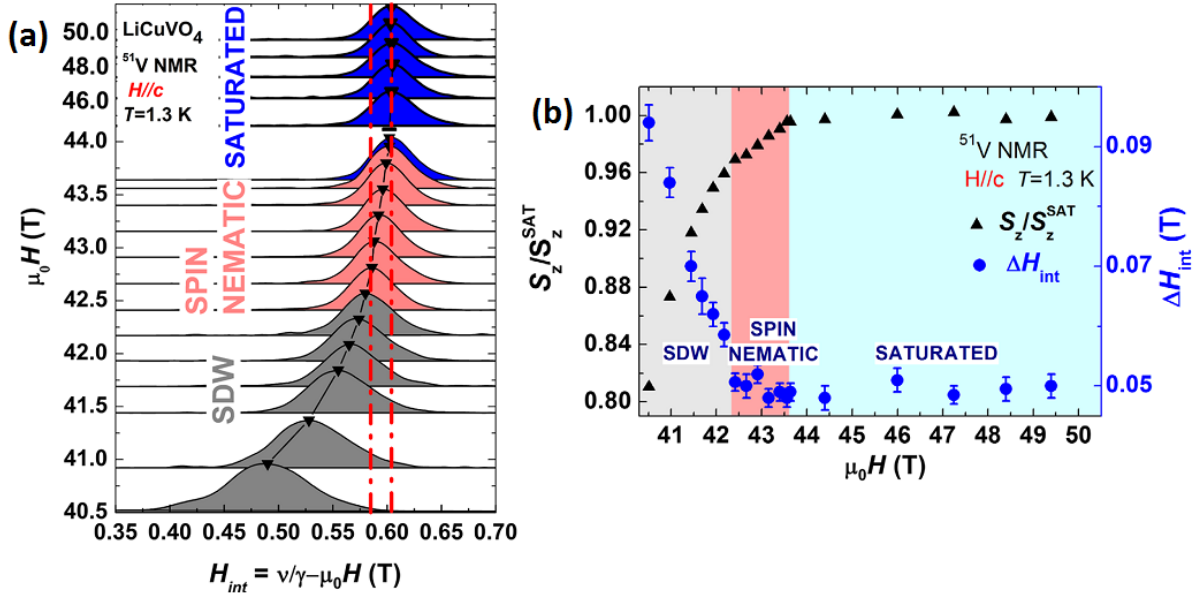
Figure 4.20: NMR spectral shift and width of LiCuVO$_4$.
(a) ^{51}V Spectra obtained at $T = 1.3$ K in the high field region. (b) Field dependence of spin polarization S_z/S_{sat} and distribution widths of internal magnetic field ΔH_{int} [55].

et al. [47]. In the latter work, bulk magnetization, ^{51}V NMR spectra and relaxation above 40 T was measured. The data are presented in Fig 4.19 (c). Below 40 T the spectra have square-like shape with two horns, typical for the SDW phase. In the region 40.5 T$< \mu_0 H <41.4$ T, the spectra become narrower and the peak shifts. Above 41.4 T the peak shape and shift is constant indicating that the system saturated. The discrepancy between peak shift and change of the slope above H_{c3} in magnetization measurements was attributed to defects. Later, Orlova et al. [55], performed a similar study on LiCuVO$_4$, but on samples from a different batch. These measurements are shown in Fig 4.20. Contrary to the results of Büttgen [47], Orlova et al report that the spectra of ^{51}V in the region between 42.41 T and 43.55 T have the same width while the peak simultaneously shifts with field. The discrepancy between these these two results was explained by the absence of defects in the sample used in the work by Orlova. Yet the absence of T_1 measurements due to the high saturation field remains a severe drawback, and definitive proof of the existence of a QN phase is still lacking.

To summarize, our investigation of LiCuSbO$_4$ has shown that in the future one should look for QN phase in the field range $12.5-13$ T at temperatures below 1.5 K.

Chapter 5

Conclusion and Outlook

This thesis describes my exhaustive experimental work on the $J_1 - J_2$ compound LiCuSbO$_4$, a candidate for observing quadrupolar nematic state, which was theoretically predicted more than thirty years ago. Several experimental techniques were used: NMR, μSR and SQUID, to investigate different parts of the temperature-field phase diagram. Special attention was given to the $T \to 0$ K part of phase diagram where different field-induced, quantum phases exist and can be identified with the help of theoretical results. From μSR measurements in zero field we have excluded conventional 3D ordering down to 30mK, and together with SQUID measurements we concluded that this vector chiral phase extends up to $\approx$4 T. From NMR results we concluded that in higher magnetic fields from ≈ 5 T to ≈ 12.5 T a field induced SDW$_2$ phase is stabilized. It is crucial to determine the value of the saturation field, since the nematic phase is expected just below the saturation field. From NMR shift measurements we have confirmed that the magnetization is saturated at $B = 13$ T. From the above we narrowed down the possibility for the existence of a quadrupolar nematic phase in LiCuSbO$_4$ in the field interval between 12.5 and 13 T. Conclusive proof of the presence of this phase remains a goal for future investigation. The results of this work show that further investigation of the possible QN phase in LiCuSbO$_4$ is feasible, owing to low saturation fields, accessible in standard DC magnets.

Chapter 6

Prošireni sažetak

6.1   Uvod

Jednodimezionalni (1D) fizikalni sustavi jedni su od najjednostavnijih, ali unatoč tome, zahvaljujući različitim tipovima interakcija i jakih korelacija, i dalje zadržavaju bogata fizikalna svojstva. Lokalizirani 1D sustavi su još jednostavnija podklasa tih sustava, s obzirom na to da se u njima mora voditi računa samo o spinskom podsustavu. U takvim, jednostavnijim sustavima, moguća je i lakša provjera analitičkih i numeričkih modela. Možemo se podsjetiti kako usprkos jednostavnosti, do danas nije poznato osnovno stanje najjednostavnijeg Heisenbergovog anitferomagnetskog hamiltonijana u tri dimenzije.

Poticaj istraživanju antiferomagnetskih sustava bilo je i otkriće visokotemperaturnih supravodiča krajem osamdesetih godina prošlog stoljeća, u čijem se faznom dijagramu uz supravodljivu uvijek nalazila i antiferomagnetska faza. Postavlja se pitanje jesu li to dva neovisna ili vezana fenomena. Antiferomagetske fluktuacije bile su smatrane i kandidatom za vezanje elektrona u Cooperovim parovima.

Jednodimezionalni spoj $LiCu_2O_2$ jedan je prototip spoja u kojem se uz feromagnetsku interakciju među prvim susjedima ($J_1 < 0$) javlja i antiferomagnetska među drugim susjedima ($J_2 > 0$). Takve interakcije vode do frustracije, zajedničkog sastojka za mnoge zanimljive sustave. Ispostavlja se da se u tom spoju simultano s magnetskim uređenjem javlja i feroelektričnost, što je vrlo zanimljivo za potencijalnu industrijsku primjenu takvih materijala.

U jednodimenzionalnim sustavima moguća su i egzotična solitonska pobuđenja kao i nova stanja materije. Zbog ograničenog faznog prostora u jednoj dimenziji i jakih korelacija, teorija Fermijeve tekućine nije adekvatna, već se mora koristiti teorija Luttingerovih tekućina kao početna točka za teorijski opis fizikalnih sustava. Prvi čvrsti eksperimentalni dokaz posto-

janja spojeva u kojima je Luttingerov opis jednodimezinalnih svojstava materijala opažen bio je sustav spinskih ljestvi BPCB.

U ovom radu proučavali smo spoj LiCuSbO$_4$, kadidat za opažanje magnetske nematičnosti, svojstva materije u kojem postoji skriveni magnetski red koji nije opisan vektorom nego tenzorom višeg reda.

6.2 Kvadrupolarni nematici

Magnetski red obično je povezan s nekom vrstom spinskog uređenja u kojemu na pojedinom mjestu vrijedi $\langle \mathbf{S}_i \rangle \neq 0$. Možemo se pitati može li postojati neka vrsta uređenja koja narušava rotacijsku $O(3)$ simetriju, a da pritom $\langle \mathbf{S}_i \rangle = 0$? Takav red u najjednostavnijem slučaju mogla bi parametrizirati bilinearna kombinacija spinskih operatora koja je neiščezavajuća $\langle S^\alpha S^\beta \rangle \neq 0$, pri čemu su $\alpha, \beta \in x, y, z$. Takav red se naziva još i nematski po uzoru na nematsko uređenje u tekućim kristalima u kojima je red opisan tenzorom drugog reda, što je prvi puta predložio de Gennes. Najjednostavnija bilinearna kombinacija operatora naziva se i kvadrupolarnom.

Takvo se uređenje može dogoditi u spinskim lancima u kojima postoji feromagnetska interakcija prvih susjeda ($J_2 < 0$) i antiferomagnetska interakcija između drugih susjeda ($J_2 > 0$). Topološki gledano, takvi su lanci ekvivalentni cik-cak ljestvama, odakle je vidljivo da interakcija drugih susjeda uvodi frustraciju. Primjena magnetskog polja sumjerljiva energiji interakcija J_1 i J_2 u takvim sustavima dovodi do kvantne kritičnosti.

Ovisno o jakosti primijenjenog magnetskog polja i omjera interakcije prvih i drugih susjeda, pojavljuju se tri različite faze.

Vektor-kiralna (VC) faza u području malog magnetskog polja, u kojoj je prosječna vrijednost spina na svakom mjestu iščezavajuća ($\langle S \rangle = 0$), a korelacija koja se najsporije raspada u prostoru je opisana parametrom reda:

$$\kappa(r, d) = \langle [\mathbf{S}_0 \times \mathbf{S}_d]^z [\mathbf{S}_r \times \mathbf{S}_{r+d}]^z \rangle, \tag{6.1}$$

gdje je $d = 1$ kada se računa korelacija među J_1 vezama, a $d = 2$ u slučaju J_2 veza, dok je r udaljenost između nultog i r-tog spina.

Val gustoće spina p vezanih spinova (SDW_p) javlja se kad povećamo magnetsko polje. Elementarno pobuđenje je okretanje p vezanih spinova ($\Delta S^z = p$), a dominantna korelacijska funkcija:

$$\langle S_0^z S_r^z \rangle - \langle S_0^z \rangle \langle S_r^z \rangle \propto \cos \left[\frac{(1 - m/m_{sat})\pi r}{p} \right] \frac{1}{r^K}, \tag{6.2}$$

gdje uočavamo da je $\langle S_0^z \rangle = \langle S_r^z \rangle = m$, pri čemu je m mikroskopska magnetizacija, $m_{sat} = 1/2$ saturacijska magnetizacija, a K Luttingerov parametar koji ovisi o J_1, J_2 i magnetskom polju h.

Nematska faza (N) javlja se prije saturacijskog polja, dominantna korelacijska funkcija u toj fazi je:

$$\left\langle \prod_{n=0}^{p-1} S_{0+n}^+ \prod_{n=0}^{p-1} S_{r+n}^- \right\rangle \propto (-1)^r \frac{1}{r^{1/K}}, \tag{6.3}$$

Za $p = 2$, faza se zove kvadrupolna, za $p = 3$ oktupolna, za $p = 4$ heksadekupolna. Spoj LiCuSbO$_4$ koji je proučavan u ovom radu ima omjer interakcija $J_1/J_2 \approx -2.2$, za koje se u područjima jakog magnetskog polja očekuje kvadrupolna nematska (QN) faza.

Većina eksperimentalnih tehnika mjeri korelacije drugog reda, pa je korelacije višeg reda lako previdjeti. Sato i suradnici predložili su NMR i neutronska raspršenja kao tehnike koje bi indirektno mogle mjeriti korelacije višeg reda [42]. NMR je posebno pogodan jer osjetljivost i rezolucija eksperimenta raste s magnetskim poljem. Opservabla koja je osjetljiva na promjenu dominantnih korelacija je spin-rešetka relaksacija T_1. Naime kad temperatura $T \to 0$ K u SDW_2 fazi $1/T_1$ divergira dok u QN fazi $1/T_1 \to 0$. U temperaturnom režimu $\omega/k_B \ll T \ll J_2$ ovisnost $1/T_1$ o temperaturi iznosi:

$$\frac{1}{T_1} = D_1^{\parallel} T + D_2^{\parallel} T^{2K-1} + ..., \tag{6.4}$$

gdje je K Luttingerov parametar koji je jednak $\frac{1}{2}$ upravo na granici između SDW_2 i QN faze, dok su D_1 i D_2 temperaturno neovisne konstante. Usporedbe radi, za standardni antiferomagnetski lanac s interakcijom prvih susjeda, relaksacija iznosi:

$$\frac{1}{T_1} = E_1^{\parallel} T + E_2^{\parallel} T^{2K-1} + E_1^{\perp} T^{1/(2K)-1} ..., \tag{6.5}$$

gdje su $E_1^{\parallel}$, $E_2^{\parallel}$ i $E_1^{\perp}$ ponovno temperaturno neovisne konstante. Treći član u jednadžbi 6.5 divergira i za $K > \frac{1}{2}$.

Među dosad poznatim materijalima opisanim $J_1 - J_2$ hamiltonijanom (6.1) najistraživaniji spoj je LiCuVO$_4$, koji ima prilično visoko saturacijsko polje od ≈ 45 T. Spoj LiCuSbO$_4$, istraživan u ovom radu, opisan je parametrima $J_1 = -75$ K, $J_2 = 34$ K i blagom anizotropijom lake magnetizacijske ravnine $\Delta = 0.83$. U nultom polju postojanje 3D uređenja isključeno je do temperature 100 mK, a saturacijsko polje procijenjeno je na ≈ 12 T [41]. U radu Dutton i suradnika [41] materijal je temeljito karakteriziran mjerenjima rendgenske difrakcije, susceptibilnosti, magnetizacije, toplinskog kapaciteta i neutronske difrakcije. Na niskim temperaturama

Table 6.1: $J_1 - J_2$ spojevi.

Eksperimentalno određena svojstva materijala opisanih $J_1 - J_2$ hamiltonijanom

Spoj	J_1[K]	J_2[K]	J_1/J_2	$\mu_0 H$[T]	T_N[K]	$|J_1/T_N|$	Ref.
LiCuSbO$_4$	-75	34	-2.2	13	<0.03	>2500	[41]
LiCuVO$_4$	-18.5	44	-0.42	45-52	1.7-2.3	9.3	[45–47]
LiCu$_2$O$_2$	-66-94	168	-0.41	est. 110	9,22,24	10.4	[48,49]
Li$_2$CuO$_2$	-100	60	-1.7	?	9	11.1	[50]
Cs$_2$Cu$_2$Mo$_3$O$_{12}$	-93	33	-2.8	≈ 10	1.85	50.3	[51]
Rb$_2$Cu$_2$Mo$_3$O$_{12}$	-138	51	-2.7	14	<2	69	[52]
PbCuSO$_4$	-100	36	-2.8	≈ 10	2.8	36	[53]
NaCu$_2$O$_2$	-16.4	90	-0.18	?	12	1.3	[54]

($T < 9$ K), razvijaju se kratkodosežne korelacije. Posebno je zanimljiva pojava vrha u toplinskom kapacitetu na $T = 0.7$ K koji se povećava s povećanjem magnetskog polja do 11 T, da bi u polju 14 T gotovo potpuno iščeznuo. Neutronska mjerenja pokazuju dobro slaganje s numeričkim računom egzaktne dijagonalizacije spinskog lanca sa 16 spinova i ranije navedenim parametrima.

6.3 Metode

6.3.1 Mionska spinska rotacija

Mionska spinska rotacija (μSR) je uz tehniku neutronske difrakcije i nuklearne magnetske rezonancije (NMR) jedna od najčešće korištenih „lokalnih proba" u fizici čvrsog stanja. Ovdje nećemo ulaziti u detalje kako se proizvode (pozitivni) mioni već samo iznijeti nekoliko elementarnih svojstava miona i što nam mogu reći o magnetskim svojstvima mate-rijala. Mioni koji upadaju na uzorak su 100% polarizirani, sa spinom obrnutim od smjera upada u materijal. Zbog velikog magnetskog momenta (≈ 3 puta većeg od mometa protona), mion je kratkoživuća čestica s vremenom života $\tau_\mu = 2.2\ \mu$s, koja se raspada na pozitron, elektronski neutrino i mionski antineutrino, pri čemu je opaziv jedino pozitron. Zbog prirode slabe sile odgovorne za raspad miona, emitirani pozitron se raspada dominantno u smjeru mionskog spina.

Tipični mionski spektrometar sastoji se od detektora stražnjeg („backward") i prednjeg („forward") detektora. Inicijalno spinovi miona pokazuju u smjeru stražnjeg detektora, pa će on de-

tektirati većinu pozitrona, međutim, ako u materijalu postoji statično ili dinamično magnetsko polje, mioni počinju precesirati oko njega ili može doći do promjene stanja spina zbog magnetskih fluktuacija. U tom će slučaju stražnji i prednji detektor registrirati određen broj miona čiji broj ovisi o vremenu. Neka je $N_B(t)$ broj pozitrona koji detektira stražnji detektor, a $N_F(t)$ broj pozitrona koji detektira prednji detektor. Veličina koja se mjeri naziva se asimetrija:

$$A(t) = \frac{N_B(t) - N_F(t)}{N_B(t) + N_F(t)}. \tag{6.6}$$

Ovisno o magnetskim svojstvima materijala i modela kojim su ona opisana, može se usporediti teorijski očekivana asimetrija s opaženom i izvršiti prilagodba podataka iz koje se dobivaju informacije o lokalnim statičkim i dinamičkim poljima u materijalu.

6.3.2 Nuklearna magnetska rezonancija

Nuklearna magnetska rezonancija je tehnika u kojoj mjereći nuklearnu magnetizaciju jezgri dobivamo informaciju o stanju „okoline" koja je određena elektronskim svojstvima materijala koji promatramo. Ovdje nećemo opisivati tehniku pulsnog NMR-a nego pokazati poveznicu između nuklearnog hamiltonijana i elektronskog sustava, te opisati opservable spektra i T_1 relaksacije.

Prvi i najčešće glavni doprinos nuklearnom hamiltonijanu dolazi od primijenjenog vanjskog magnetskog polja H_0 u z smjeru:

$$\hat{H}_0 = -\gamma \hbar \mu_0 H_0 I_z. \tag{6.7}$$

Primijenjeno magnetsko polje cijepa degenerirano spinsko stanje I jezgre na $2I + 1$ ekvidistantnih nivoa, koji se pobuđuju pulsevima. Jezgre spina većeg od $I > \frac{1}{2}$ su elipsoidne, što znači da će se u prisustvu gradijenta električnog (EFG) polja htjeti usmjeriti u pravcu najvećeg gradijenta. Ta interakcija opisana je hamiltonijanom:

$$\hat{H}_{EFG} = \frac{eQ}{4I(2I-1)}[V_{zz}(3I_z^2 - \mathbf{I}^2) + (V_{xx} - V_{yy})(I_x^2 - I_y^2)]. \tag{6.8}$$

Ovdje su $V_{\alpha\beta} = \frac{\partial^2 V}{\partial x_\alpha \partial x_\beta}$ komponente EFG tenzora, a Q kvadrupolni moment jezgre. Treći dio hamiltonijana opisuje interakciju među elektronskim i nuklearnim spinovima:

$$\hat{H}_{el-n} = -\gamma \hbar \sum_i I_\alpha A_{\alpha\beta}^i g\mu_B S_\beta^i, \tag{6.9}$$

gdje su S^i elektronski spinski operatori, $A_{\alpha\beta}^i$ hiperfini tenzor, a suma po i ide po svim elektronima s kojima interagira promatrana jezgra. Hiperfini tenzor u sebi ima komponentu spin-orbit vezanja, transferirane interakcije i dipolnog vezanja između jezgre i elektrona.

74

Spektar

Prva opservabla koja se u NMR-u mjeri je spektar. On nam daje informacije o statičkim svojstvima elektronskog podsustava. Za dani žiromagnetski faktor γ promatrane jezgre očekuje se signal na frekvenciji $\nu_0 = \gamma\mu_0 H_0$. Međutim, zbog postojanja elektrona signal je pomaknut i nalazi se na frekvenciji $\nu = (1 + K)\gamma\mu_0 H_0$, pri čemu je K pomak. Egzaktno gledajući K je tenzor povezan s hiperfinom interakcijom $A_{\alpha\beta}$. Za paramagnetske spojeve, prateći ovisnost pomaka o temperaturi i usporedbom makroskopske susceptibilnosti u slučaju kad na raspolaganju imamo monokristal, mogu se odrediti sve komponente hiperfinog tenzora. Izgled spektra, odnosno njegova promjena može nam dati informaciju u postojanju uređenja elektronskog podsustava. U praškastim uzorcima, dolazi do distribucije frekvencija na kojima opažamo signal, pa je tako detaljna analiza otežana, a često i nemoguća.

Relaksacijsko vrijepme spin-rešetka

Nakon što se pulsom nuklearna magnetizacija zarotira u $x - y$ ravninu u odnosu na ravnotežu (smjer z osi), ona se nakon vremena T_1 vraća u ravnotežno stanje. Elektronski podsustav u ovom slučaju se naziva „rešetkom”. Fluktuacije elektronskih spinova uzrokuju povratak nuklearne magnetizacije u z smjer. Spin rešetka relaksacijsko vrijeme T_1 nam dakle pruža uvid u dinamiku elekronskog spinskog sustava koji nas zanima. Egzaktan izraz glasi:

$$\frac{1}{T_1} \sim \sum_k \{\frac{\mid A_k^{\perp} \mid^2}{2}[S^{+-}(k,\omega) + S^{-+}(k,\omega)] + \mid A_k^{\parallel} \mid^2 S^{zz}(k,\omega)\}, \qquad (6.10)$$

gdje su $A_k^{\parallel}$ i $A_k^{\perp}$ Fourierovi transformati tenzora hiperfine interakcije, a $S^{+-}(k,\omega)$, $S^{-+}(k,\omega)$ i $S^{zz}(k,\omega)$ korelacijske funkcije.

6.4 Rezultati i diskusija

Rezultati prezentirani u ovom poglavlju objavljeni su u radu Bosiočić et al. [64].

6.4.1 μSR mjerenja

Glavni cilj mjerenja mionske relaksacije u uzorku bio je provjeriti postoji li magnetsko uređenje ili ne. Mjerena su obavljena na praškastom uzorku mase ≈ 1 g. U odsustvu longitudinalnog polja, asimetrija je opisana formulom $A(t) = A_0 G(t, \nu, \Delta) + A_b$, gdje $G(t, \nu, \Delta)$ dimanička Kubo-Toyabe funkcija, a parametri A_0 početna asimetrija i A_b pozadina. Na temperaturi 10 K, glavni doprinos raspadu asimetrije dolazi od nuklearnih momenata. Širina distribucije polja iznosi $\Delta/\gamma_\mu = 2.2$ G. Na nižim temperaturama distribucija se širi i dostiže plato vrijednosti

$\Delta/\gamma_\mu = 4.3$ G ispod 0.7K. Tu promjenu širine pripisali smo malom uređenju elektronskih spinova. Plauzibilno je pretpostaviti da se pozitivno nabijeni mioni zaustavljaju oko kiskovih O^{2-} iona (jedini negativni), koji su ≈ 2 Åudaljeni od Cu^{2+} iona. Najjednostavnija aproksi-macija u slučaju potpunog uređenja spinova na bakrovim ionima dala bi polje od $\mu_0\mu_B/(4\pi r^3) \approx$ 1160 G na kisikovim mjestima, dok mi opažamo tri reda veličine manju vrijednost. To vodi do zaključka da možemo odbaciti tipično 3D uređenje u našem spoju. Moguće je da je opaženi efekt posljedica kratkodosežnih korelacija koji su sugerirani u radu Dutton i suradnika [41].

6.4.2 Niskotemperaturna magnetska susceptibilnost

Mjerenja niskotemperaturne magnetske susceptibilnosti obavljena su na praškastom uzorku i na orijentiranom prahu (slika 4.8). Na orijentiranom prahu, kada je polje usmjeno duž teške osi, pojavljuje se diskontinuitet na $T = 0.7$ K na svim krivuljama. Diskontinuitet je mininum u niskim poljima (1 T i 3.5 T), dok u višim poljima (5 T i 7 T) izgleda kao blaga theta funkcija. Različitost oblika diskontinuiteta ukazuje na različite faze tj. negdje između 3.5 T i 5 T postoji fazni prijelaz. Mjerenjem na neorijentiranom prahu se ti diskontinuiteti gube.

6.4.3 NMR mjerenja

NMR mjerenja sustavno su izvođena na orijetiranom prahu tako da je magnetsko polje prim-ijenjeno duž čvrste osi. Mjeren je signal izotopa ^{7}Li. Prvi korak bio je odrediti jakost hiperfinog vezanja A_{hf} usporedbom pomaka linije K i makroskopske susceptibilnosti χ_{macro} prema relaciji (4.4) iz podataka sa slike 4.10. Dobivena je vrijednost hiperfinog vezanja $A_{hf} = -0.57(2)$ kOe/μ_B, koja nam govori o jakosti vezanja između nuklearnih spinova litija i elektronskih spinova na bakrovim ionima. Tipičan oblik spektra izgleda poput onoga na slici 4.11 ($\mu_0 H_0 = 12$ T na 1.55 K). U jediničnoj ćeliji postoje dvije pozicije litija, koji prema tome spektru dopri-nose s dvije linije. Jače vezana linija opisana je gausijanom, a slabije vezana lorencijanom, s tim da je udio jače vezane linije u glavnom vrhu 72%, a slabije vezane 28%.

U dilucijskom hladnjaku oblik spektara ovisi o primijenjenom polju (slika 4.12). Vertikalna linija pokazuje maksimalan pomak vrha (0.057 T), kada je postignut $1\mu_B$ po atomu bakra. Na nižim poljima (5.2 T, 8 T) spektar je širok i blago pravokutnog oblika što ukazuje da je došlo do uređenja (Appendix C). Spektri u polju 13 T i 13.3 T se preklapaju, a vrhovi spektara se poklapaju upravo s najvećim mogućim pomakom vrha, što ukazuje da je iznad 13 T sistem ušao u saturacijsko područje.

Relaksacijske krivulje ispod 12 T i iznad 5 K prilično su dobro opisane jednoeksponencijalnim krivuljama. Iznad 12 T i ispod 5 K korištena je preciznija funkcija koja ima u vidu da su u glavnom vrhu prisutni signali s dvije pozicije litija:

$$1 - \frac{M(\tau_1)}{M_\infty} = ae^{-(\tau_1/T_1)^\beta} + (1-a)f(\tau_1), \tag{6.11}$$

pri čemu je M_∞ vrijednost magnetizacije u ravnoteži, a predstavlja doprinos jače vezane linije u spektru i fiksiran je na 0.72, dok je $f(\tau_1)$ relaksacija slabije vezane linije, koja je nezavisno određena mjerenjem na desnoj strani spektra. Mjerili smo ovisnost T_1 o polju na dvije temperature: 1.55 K i 4.6 K. Iz mjerenja lokalne magnetizacije (pomaka linije), znamo da je vrijednost magnetizacije na $\approx 20\%$ saturacijske vrijednosti M_s na otprilike 6 T. Sudan i suradnici predviđaju promjenu iz vektor-kiralne u SDW_2 fazu na otprilike 20% magnetizacije, pa vrh u $1/T_1$ na 6 T možemo pripisati blizini $VC - SDW_2$ granice. Kvadrupolarna nematska faza predviđena je iznad 70% saturacijske magnetizacije M_s. Krivulja magnetizacije je jako oštra u tom području i moguće je da QN faza postoji u uskom području između 12 T i 13 T. S obzirom na ranije navedeno izabrali smo polja $\mu_0 H_0 = 4, 8, 12$ and 13 T na kojima smo odlučili mjeriti ovisnost $1/T_1$ o temperaturi. U polju $\mu_0 H_0 = 4$ T, gdje je očekiva VC faza, $1/T_1$ pokazuje tragove divergencije do temperature 1.55 K, s kritičnim eksponentom $1/T_1 \propto T^{-0.55(2)}$ ($K = 0.24(1)$). U polju $\mu_0 H_0 = 8$ T, gdje se očekuje SDW_2 faza, $1/T_1$ pokazuje slično ponašanje s kritičnim eksponentom $1/T_1 \propto T^{-0.30(1)}$ ($K = 0.38(1)$). Precizne vrijednosti parametra K su osjetljive na područje u kojem vršimo prilagodbu, ali je jasno da se K monotono povećava s poljem, kao što je teorijski predviđno. Temperarutarna ovisnost $1/T_1$ u magnetskom polju $\mu_0 H_0 = 12$ T pokazuje široki maksimum oko 2.5 K što moguće ukazuje na blizinu QN faze. U polju $\mu_0 H_0 = 13$ T, vrh se pomiče na višu temperaturu od 6K, ali ispod 2.2 K pad je preoštar da bi se pripisao QN fazi. Ako uzmemo u obzir mjerenja u dilucijskom hladnjaku, kritični eksponent je $1/T_1 \propto T^{3.6}$, što daje nefizikalnu vrijednost $K = 2.3(1)$. Vjerojatnije objašnjenje, u skladu s rezultatima statičkih mjerenja, je da sustav ulazi u saturacijski režim na 13T i da $1/T_1$ pokazuje eksponencijalni procjep u spektru pobuđenja. Podaci u polju 13 T ispod 2.9 K prilagođeni su na funkciju $1/T_1 = C_1 exp(-\Delta/T) + C_2$, gdje je $\Delta = 3.24(19)$K, $C_1 = 0.396(47)$ ms^{-1} i $C_2 = 5.1(1.4) \times 10^{-5}$ ms^{-1}. Posljednja, temperaturno neovisna, konstanta uzima u obzir doprinose nečistoća i/ili defekata. Možemo zaključiti da se ovisnost spin rešetka relaksacije mijenja kvalitativno i kvantitativno u uskom području između 12 i 13 T, od divergencije, karakteristične za SDW_2 fazu do eksponencijalnog procjepa karakterističnog za saturacijski režim.

6.4.4 Diskusija

U razmatranju faznog dijagrama vodit ćemo se radom Sudana i suradnika [40], za omjer interakcije prvih i drugih susjeda $J_1/J_2 = -2.22$. Predviđene su sljedeće faze: (i) vektor-kiralna (VC) za $M/M_{sat} < 0.15$, (ii) SDW$_2$ faza za $0.15 < M/M_{sat} < 0.7$, i (iii) kvadrupolna nematska (QN) za $0.7 < M/M_{sat} < 1$. Koristeći NMR pomak na temperaturi $T = 0.125$ K (slika 4.13) kao mjeru magnetizacije, možemo procijeniti da se $M/M_{sat} = 0.15$ postiže za $\mu_0 H \approx 5\,\mathrm{T}$, $M/M_{sat} = 0.7$ za $\mu_0 H \approx 12\,\mathrm{T}$, i $M = M_{sat}$ na $\mu_0 H \approx 13\,\mathrm{T}$.

Vektor-kiralna faza. Iz μSR mjerenja, zaključujemo da nema klasičnog 3D uređenja u nultom polju do 30 mK. Ti podaci su označeni zvjezdicama na slici 4.17. Dutton i suradnici [41] sugeriraju da je mogući razlog za to činjenica da susjedni lanci nisu paralelni, nego nakošeni jedni spram drugih. Uzmemo li u obzir SQUID podatke na 1 T i 3.5 T, gdje se vidi singularitet na 0.7 K u magnetskoj susceptibilnosti možemo zaključiti o granicama VC faze. Iznad 5 T susceptibilnost pokazuje drugačiju ovisnost i možemo zaključiti da se radi o drugačijoj fazi u odnosu na onu u nižim poljima. Uz to, krivulje toplinskog kapaciteta su vrlo slične u polju 0 T i 2 T, i polako se mijenjaju iznad 4 T. Iz toga možemo zaključiti da se granica između te dvije faze događa negdje između 4T i 5T.

SDW$_2$ faza. NMR spektri na 125 mK u poljima 5.2 T i 8 T jasno ukazuju da je došlo do magnetskog uređenja. NMR relaksacija u polju 8 T iznad temperature prijelaza pokazuje ovisnost $1/T_1 \propto T^{-0.30(1)}$ što je konzistentno sa SDW$_2$ fazom (negativni eksponent manji od 1). Ta opažanja ukazuju da je u poljima od ≈ 5 T do ≈ 12 T SDW$_2$ faza stabilizirana vanjskim magnetskim poljem.

Moguća kvadrupolarna nematska (QN) faza. Relaksacijska NMR mjerenja u polju 12 T pokazuju negativni nagib krivulje iznat $T = 2.5$K, u skladu s SDW$_2$ fazom, ali ispod 2.5 K nagib se počinje mijenjati u pozitivni, što bi moglo biti konzistentno s QN fazom (pozitivni eksponent manji od 1). Takvo ponašanje moguće ukazuje na blizinu prijelaza između SDW$_2$ i QN faze. Suprotno SDW$_2$ fazi, QN faza ne bi trebala širiti NMR spektar [55]. Spektar u polju 12 T sa slike 4.12 je uži nego spektri u polju 5.2 i 8 T, ali širi od onih u višem polju. To također ukazuje na blizinu QN faze. Spektar u polju 12.5 T je uži, a pomak ukazuje da je magnetizacija u 12.5T na razini $M/M_{sat} = 0.85$ što bi prema teorijskom faznom dijagramu bilo u QN fazi ($M/M_{sat} > 0.7$). Teorijski je predviđeno da u sustavima s anizotropijom čvrste osi, QN faza može biti realizirana za veće vrijednosti magnetizacije. U svakom slučaju, donja granica za QN fazu trebala bi biti blizu 12.5 T. S druge strane u polju 13 T opažena je saturacija što daje gornju granicu za QN fazu.

Saturacija. U saturacijskom području očekuje se procjep u spektru pobuđenja. To je potvrđeno u našim relaksacijskim mjerenjima iz kojih je vrijednost procijepa $\Delta \approx 3.2\,\mathrm{K}$ u polju 13 T. Teorijski model za izotropni lanac [35] predviđa otvaranje procjepa (tj. ulazak u saturacijsko područje) kada je omjer energije spina u polju $\epsilon_s = g\mu_B\mu_0 H_s$ i interakcije drugih susjeda J_2 jednak $\epsilon_s/J_2 \approx 0.5$, što je u izvrsnom slaganju s našim opažajima (za $g = 2.21$ u polju $\mu_0 H_0 = 13$ T, $\epsilon_s = 18.2$ K dok je $J_2 = 34$ K).

6.5 Zaključak

U ovom smo radu prikazali istraživanje $J_1 - J_2$ spoja LiCuSbO$_4$, kandidata za opažanje kvadrupolne nematske faze, koja je teorijski predviđena prije više od 30 godina. Korišteno je više tehnika: NMR, μSR i SQUID kako bismo dobili informacije o različitim dijelovima faznog dijagrama. Posebna je pažnja dana niskotemperaturnim mjerenjima $T \to 0$ K gdje se očekuju različita kvantna svojstva osnovnog stanja koja ovise o primijenjenom magnetskom polju. Iz μSR mjerenja u nultom polju isključili smo tipično 3D uređenje do temperature 30 mK. Iz toga, zajedno sa SQUID rezultatima zaključujemo o postojanju vektor kiralne faze do $\approx$4 T. Iz NMR mjerenja proizlazi da u višim poljima od ≈ 5 T do $\approx$12.5 T postoji SDW$_2$ faza koja je stabilizirana vanjskim magnetskim poljem. Presudno je odrediti vrijednost saturacijskog polja, jer se nematska faza nalazi tik ispod njega. Iz mjerenja NMR pomaka, pouzdano smo utvrdili saturacijsko polje od 13 T. Iz prethodno navedenog, suzili smo mogućnost postojanja kvarupolne nematske faze u LiCuSbO$_4$ u intervalu između 12.5 i 13 T. Jak dokaz za postojanjem te faze ostaje cilj za buduća istraživanja. Rezultat ovog rada pokazuje da su buduća istraživanja QN faze u LiCuSbO$_4$ moguća, naročito s obzirom na nisko saturacijsko polje dostupno u standardnim laboratorijskim magnetima.

Appendix A

Relaxation of weakly coupled site

At the peak position the spectra have contributions from both the strongly and weakly coupled lines, with different relaxation times. To determine the contribution of the weakly coupled line which corresponds to the function $f(\tau_1)$ in Eq. (4.5) we measured the relaxation on the right side of the spectra at 30% of the peak value where the contribution of the strongly coupled site is negligible. The relaxation curves of the weakly coupled line reveal two different relaxation regimes: a fast one with a relaxation time T_{1b} shorter than T_1 of the strongly coupled site, but of the same order of magnitude, and a long one T_{1c} which is several orders of magnitude longer than T_1 and T_{1b} at low temperatures as shown on Fig A.1.
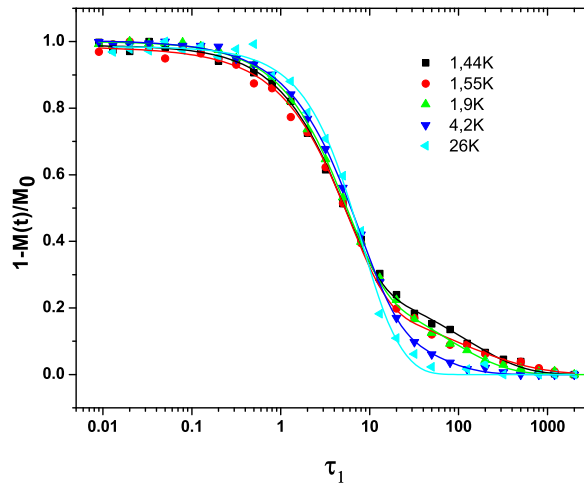

Figure A.1: Relaxation of the weakly coupled site

Our main goal was to fix T_{1b} so we could isolate T_1 in Eq. (4.5). We used the function $f(\tau_1)$ (for the weakly coupled site):

$$f(\tau_1) = be^{-(\tau_1/T_{1b})^{\beta_b}} + ce^{-(\tau_1/T_{1c})^{\beta_c}}. \qquad (A.1)$$

Having set $(1 - a) = 0.28$ in Eq. 4.5, the weights $b = \frac{0.22}{0.28}$ and $c = \frac{0.06}{0.28}$ were determined, we were able to fit the contributions of the fast and slow relaxation processes. The stretch parameters β_b and β_c were fixed to 1 above 1.55 K and left as free parameters at lower temperature measurements.

Spectra taken in $\mu_0 H_0 =$12 T at different temperatures show indeed that the spectral shape does not change appreciably between 1.55 K and 30 K, and we take the coefficients a, b and c as temperature independent. The spectral shape does not change either between 12 T and 13 T at 1.55 K, and we conclude that these parameters are field independent as well (for high fields). The parameter M_∞ was taken from the last measured point at $\tau_1 > 7 \times T_1(T_{1b})$, limited by the repetition time which had to be reasonably short in order to make measurements possible. The total signal did not relax completely between two acquisitions, but this affects only the value of the longest relaxation time T_{1c}. Since T_{1c} is an order of magnitude longer than T_1 and T_{1b}, it turns out that its exact values are not critical for the determination of T_1. The values of T_{1b} was determined for each temperature and fixed before the T_1 in Eq. (4.5) was calculated. The stretch parameter β_b ranges from 0.51 at lowest temperature to 1 at 1.55 K.

Appendix B

Calculation of EFG tensor

Calculation of EFG parameters using point charge distribution in python. We assumed point charge distribution on each ion inside the unit cell. The code first reads position of the atoms in unit cell from an ASCII file, and adds up contribution $\partial^2 V/\partial x_\alpha \partial x_\beta$ of each atom within a given distance to a selected nuclei inside unit cell. After summation, the matrix $\partial^2 V/\partial x_\alpha \partial x_\beta$ is diagonalized, end eigenvectors are calculated.

```
from math import*
from numpy import*
hmax=12
kmax=12
lmax=4
nn=30
g=13
distance=30
a=5.7925
b=5.7925
c=14.2918
br=0;
print "atom broj:", g
print "hkl maximum:",hmax, kmax, lmax,"maksimalna udaljenosti u angstremima",
hmax*a,kmax*b,lmax*c;
print "max distance",distance
norm=[[a,b,c]]
```

```python
structure=zeros((nn,3))
details=zeros((nn,2))
Vxx=0
Vxy=0
Vxz=0
Vyx=0
Vyy=0
Vyz=0
Vzx=0
Vzy=0
Vzz=0
ulaz=open("LiCuSbO4.dat","r")
for i in range(0,nn):
red=ulaz.readline()
razdvajanje=red.split("")
for j in range(0,5):
if j<3:
structure[i][j]=float(razdvajanje[j])
else: details[i][j-3]=float(razdvajanje[j])
ulaz.close()
v0=mat([[a*structure[g-1][0]+b*0.5*structure[g-1][1],b*sqrt(3)*0.5*structure[g-1][1],c*structure[g-1][2]]])
for h in range(-hmax,hmax+1):
for k in range(-kmax,hmax+1):
for l in range (-lmax,lmax+1):
for i in range(0,nn):
vip=mat(structure[i])+mat([[h,k,l]])
vi=mat([[a*vip[0,0]+b*0.5*vip[0,1],b*sqrt(3)*0.5*vip[0,1],c*vip[0,2]]])
r=v0-viif h==0 and k==0 and l==0 and i==(g-1)
:t=2
print "izbjegao sam", vi
elif linalg.norm(r)<distance:
br=br+1
```

```
r5=pow(linalg.norm(r),5)
if r5==0: print h,k,l,i
Vxx=Vxx+details[i][0]*details[i][1]*(2*r[0,0]*r[0,0]-r[0,1]*r[0,1]-r[0,2]*r[0,2])/r5
Vyy=Vyy+details[i][0]*details[i][1]*(2*r[0,1]*r[0,1]-r[0,0]*r[0,0]-r[0,2]*r[0,2])/r5
Vzz=Vzz+details[i][0]*details[i][1]*(2*r[0,2]*r[0,2]-r[0,0]*r[0,0]-r[0,1]*r[0,1])/r5
Vxy=Vxy+details[i][0]*details[i][1]*3*r[0,0]*r[0,1]/r5
Vxz=Vxz+details[i][0]*details[i][1]*3*r[0,0]*r[0,2]/r5
Vyz=Vyz+details[i][0]*details[i][1]*3*r[0,1]*r[0,2]/r5
print "pozicija atoma", v0, "broj", g
print "broja atoma unutar DISTANCE", br
print "Vxx", Vxx
print "Vyy", Vyy
print "Vzz", Vzz
print "Vxy", Vxy
print "Vxz", Vxz
print "Vyz", Vyz
V=zeros((3,3))
V[0][0]=Vxx
V[1][1]=Vyy
V[2][2]=Vzz
V[0][1]=Vxy
V[0][2]=Vxz
V[1][2]=Vyz
V[1][0]=Vxy
V[2][0]=Vxz
V[2][1]=Vyz
VV=mat(V)
print "EFG tenzor", VV
print linalg.eigh(VV)
```

Appendix C

Spectral shape in case of a simple spin freezing

Simulation of spectra when simple magnetic freezing occurs where nuclei experience random distribution of the direction of antiferromagnetic internal fields. The intensity distribution in case of a sweep field is [81]:

$$I(H) = \frac{1}{4H_A}|1 + \frac{H_0^2 - H_A^2}{H^2}|, \qquad \text{(C.1)}$$

where H_A is local magnetic field, H external applied field and H_0 resonant field. Equation C.1 is valid for $|H_0 - H_A| \leq H \leq H_0 + H_A$. Intensity distribution is plotted on fig C.1.

```
from math import*
from numpy import*
from matplotlib import cm
from matplotlib.ticker import LinearLocator, FormatStrFormatter
import matplotlib.pyplot as plt
import numpy as np
H0=5
HA=0.043
dH=0.0005
D=round(HA/dH)+100
Y=[]
X=[]
for i in range(-D,D):
```
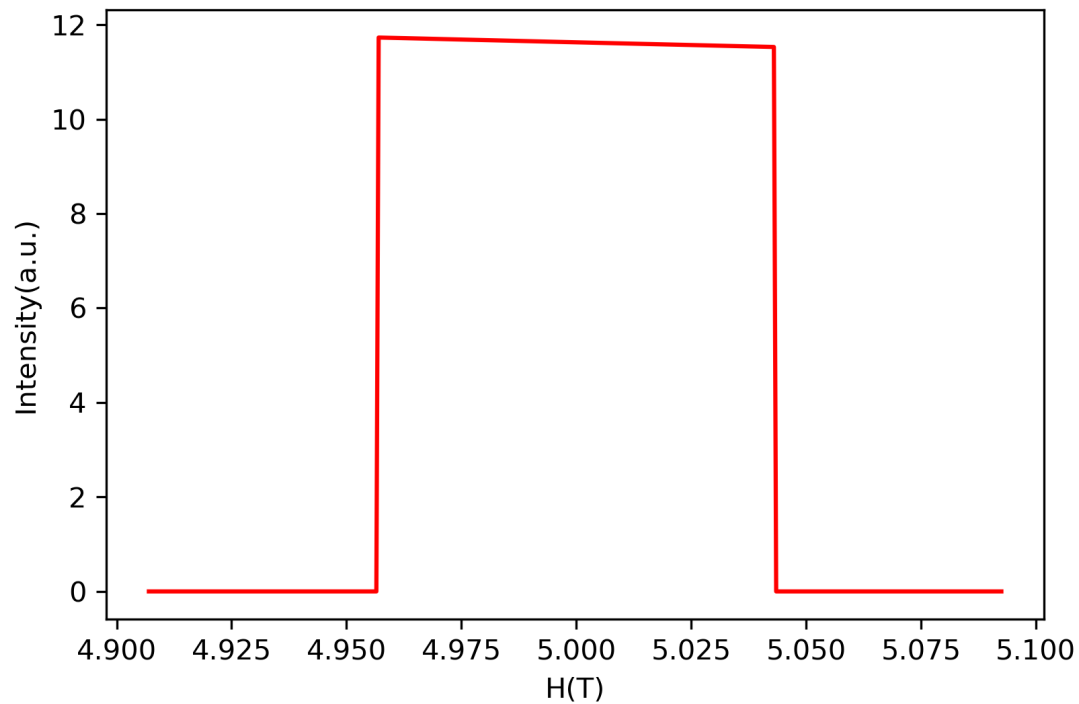
Figure C.1: Spectral shape in case of simple spin freezing.

```
Y.append(0)
X.append(H0+i*dH)
print(Y)
print(X)
for i in range(-D,D):
H=X[i]
if ((H0-HA)¡=H) and (H¡=(H0+HA)):
Y[i]=1./(4*HA)*(1+(H0**2-HA**2)/H**2)
print(Y)
plt.plot(X,Y,'r-')
plt.ylabel('Intensity(a.u.)')
plt.xlabel('H(T)')
plt.savefig('spektar', dpi=300)
plt.show()
```

Bibliography

[1] H. J. Grafe et al., *Scientific reports*: **7**, 6720, (2017)

[2] S. R. White, *Phys. Rev. Lett.*: **69**, 2863, (1992)

[3] A. Kordyuk, *Low Temperature Physics*: **41**, 319, (2015)

[4] M. Horvatić et al., *Phys. Rev. B*: **47**, 3461, (1993)

[5] M. Horvatić et al., *Phys. Rev. B*: **48**, 13848, (1993)

[6] A. J. Millis, H. Monien, D. Pines, *Phys. Rev. B*: **42**, 167, (1990)

[7] H. Monien, M. Takigawa, *Phys. Rev. B*: **43**, 258, (1991)

[8] F. Mila, T.M. Rice, *Physca C: Superconductivity*: **157**, 561, (1989)

[9] H. Mukuda et al., *JPSJ*: **81**, 011008, (2012)

[10] P. W. Anderson, *Science*: **235**, 1196, (1987)

[11] S. Park et al., *Phys. Rev. Lett.*: **98**, 057601, (2007)

[12] S. Seki, Y. Onose, Y. Tomura, *Phys. Rev. Lett.*: **101**, 067204, (2008)

[13] E. Ising, *Z. Physik*: **31**, 253, (1925)

[14] H. Bethe, *Z. Physik*: **71**, 205, (1931)

[15] J. A. Questa, A. Sanchez, *Journal of Statistical Physics*: **115**, 869, (2004)

[16] T. Giamarchi, *Quantum Physics in One Dimension*. Claderon Press, (2003)

[17] M. Klanjšek et al., *Phys. Rev. Lett.*: **101**, 137207, (2008)

[18] J. Skalyo et al., *Phys. Rev. B*: **2**, 4632, (1970)

[19] I. U. Heilmann, *Phys. Rev. B*: **18**, 3530, (1978)

[20] S. K. Satija et al., *Phys. Rev. B*: **21**, 2001, (1980)

[21] B. Lake et al., *Nature Materials*: **4**, 329, (2005)

[22] H. Rosner et al., *Phys. Rev. B*: **56**, 3402, (1997)

[23] J. Schlappa et al., *Nature*: **485**, 82, (2012)

[24] C. Kim et al., *Phys. Rev. Lett.*: **77**, 4054, (1996)

[25] M. Mourigal et al., *Nat. Phys.*: **9**, 435, (2013)

[26] L. Balents, *Nature*: **464**, 199, (2010)

[27] K. Penc, A. M. Läuchi, *Introduction to Frustrated Magnetism*, Springer, (2011)

[28] F. Reinitzer, *Monatshefte fur Chemie*: **9**, 421, (1888)

[29] P. G. De-Gennes, *The Physics of Liquid Crystals*, Clarendon Press, Oxford, (1974)

[30] S. Ziherl et al., *A Teaching Unit on Liquid Crystals*, 2010

[31] F. Mila, *Physics*: **10**, 64, (2017)

[32] A. F. Andreev, I. A. Grishchuk, *JETP*: **60**, 267, (1984)

[33] P. Lecheminant, K. Totsuka, *Phys. Rev. B.*: **74**, 224426, (2006)

[34] F. Heidrich-Meisner, A. Honecker, T. Vekua, *Phys. Rev. B*: **74**, 020403, (2006)

[35] L. Kecke, T. Momoi, A. Furusaki, *Phys. Rev. B*: **76**, 060407, (2007)

[36] T. Hikihara et al., *Phys. Rev. B*: **78**, 144404, (2008)

[37] A. V. Chubukov, *Phys. Rev. B*: **44**, 4693, (1991)

[38] T. Vekua et al., *Phys. Rev. B*: **76**, 174420, (2007)

[39] M. Sato, T. Hikihara, T. Momoi, *Phys. Rev. Lett.*: **110**, 077206, (2013)

[40] J. Sudan, A. Lüscher, A. M. Läuchi, *Phys. Rev. B*: **80**, 140402, (2009)

[41] S. E. Dutton et al., *Phys. Rev. Lett.*: **108**, 187206, (2012)

[42] M. Sato, T. Momoi, A. Furusaki, *Phys. Rev. B*: **79**, 060406, (2009)

[43] M. Sato, T. Hikihara, T. Momoi, *Phys. Rev. B*: **83**, 064405, (2011)

[44] R. Chitra, T. Giamarchi, *Phys. Rev. B*: **55**, 5816, (1997)

[45] M. Enderle et al., *EPL*: **70**, 237, (2005)

[46] K. Nawa et al., *JPSJ*: **82**, 094709, (2013)

[47] N. Büttgen et al., *Phys. Rev. B*: **90**, 134401, (2014)

[48] T. Masuda et. al. *Phys. Rev. Lett.*: **92**, 177201, (2004)

[49] A. A. Gippius et al., *Phys. Rev. B*: **70**, 020406, (2004)

[50] S. Giri et al., *Journal of Alloys and Compounds*: **326**, 61, (2001)

[51] Y. Hoshino et al., *arXiv:1309.5473*, (2013)

[52] M. Hase et al., *Phys. Rev. B*: **70**, 104426, (2004)

[53] B. Willemberg et al.,*Phys. Rev. Lett.*: **108**, 117202, (2012)

[54] L. Capogna et al., *Phys. Rev. B*: **71**, 140402, (2005)

[55] A. Orlova et al., *Phys. Rev. Lett.*: **118**, 247201, (2017)

[56] J. Sirker, *Phys. Rev. B*: **81**, 014419, (2010)

[57] J. E. Sonier, *Muon spin rotation/relaxation/resonance*, brochure

[58] S. J. Blundell, *Contemp. Phys.*: **40**, 175, (1999)

[59] P. Carretta, A. Lascialfari, *NMR-MRI, μSR and Mossbauer Spectroscopies in Molecular Magnets*: Springer, (2007)

[60] C. P. Slichter *Priniciples of Magnetic Resonance*, Springer- Verlag, (1989)

[61] E. Fukushima, S. B. W. Roader, *Experimental Pulse NMR, A Nuts and Bolts Approach*, CRC Press, (1981)

[62] J. F. Baugher et al, *The Journal of Chemical Physics*: **50**, 4914, (1969)

[63] K. Uhlig, W. Hehn, *Cryogenics*: **37**, 279, (1997)

[64] M. Bosiočić et al, *Phys. Rev. B*: **96**, 224424, (2017)

[65] F. L. Pratt, *Physica B*: **710**, 289, (2000)

[66] P. J. Baker, J. S. Lord, D. Prabhakaran, *Journal of Physics: Condensed Matter*: **23**, 306001, (2011)

[67] W. G. Clark et al., *Rev. Sci. Instrum.*: **66**, 2453, (1995)

[68] B. Perić et al., *Solid State Nuclear Magnetic Resonance*: **59**, 60, (2014)

[69] S. Eggert et al., *Phys. Rev. Lett.*: **99**, 097204, (2007)

[70] S. Shikevich, O. F. Syljuasen, S. Eggert, *Phys. Rev. B*: **83**, 054423, (2011)

[71] F. Tedoldi, R. Santachiara, M. Horvatić, *Phys. Rev. Lett.*: **83**, 412, (1999)

[72] T. Siroka et al., *Phys. Rev. Lett.*: **106**, 137202, (2011)

[73] V. F. Mitrović et al., *Phys. Rev. B*: **78**, 014504, (2008)

[74] F. Heidrich-Meisner, I. P. McCulloch, A. K. Kolezhuk, *Phys. Rev. B*: **80**, 144417, (2009)

[75] O. A. Starykh, L. Balents, *Phys. Rev. B*: **89**, 104407, (2014)

[76] L. E. Svistov et al., *JETP*: **93**, 24, (2011)

[77] N. Büttgen et al., *Phys. Rev. B*: **76**, 014440, (2007)

[78] N. Büttgen et al., *Phys. Rev. B*: **81**, 052403, (2010)

[79] N. Büttgen et al., *Phys. Rev. B*: **85**, 214421, (2012)

[80] M. Mourigal et al., *Phys. Rev. Lett.*: **109**, 027203, (2012)

[81] Y. Yamada, A. Sakata, *JPSJ*: **55**, 1751, (1986)

Curriculum Vitae

Marko Bosiočić was born in Rijeka, Croatia, on March the 24th, 1987. He completed elementary school in 2001, high school in 2005, and received title Master of Science in 2010 at Department of Physics, Faculty of Science, University of Zagreb under supervision of prof. dr. Miroslav Požek. During postgraduate studies he used NMR/NQR, together with μSR technique to study strongly correlated systems. From the 2011-2017, he was teaching several undergraduate courses. From 2018 he teaches physics, robotics and electromechanics at high school. Besides his scientific work, his hobbies are chess, photography and fishing.

Published articles:

1. B. Perić, R. Gautier, C. Pikard, M. Bosiočić, M. S. Grbić and M. Požek, Solid-State NMR/NQR and First-Principles Study of Two Niobium Halide Cluster Compounds, *Solid State Nuclear Magnetic Resonance*, **59-60**, 20 (2014)

2. M. Bosiočić, F. Bert, S. E. Dutton, R. J. Cava, P. J. Baker, M. Požek and P. Mendels, Possible quadrupolar nematic phase in the frustrated spin chain $LiCuSbO_4$: An NMR investigation, *Phys. Rev. B*, **96**, 224424 (2017)

3. M. Bosiočić, F. Bert, S. E. Dutton, R. J. Cava, P. J. Baker, M. Požek, P. Mendels, Postoji li kvadrupolna nematska faza u frustriranome spinskom lancu $LiCuSbO_4$? – Pogled NMR-om, Knjiga sažetaka 11, znanstveni sastanak Hrvatskog fizikalnog društva, Hrvatsko fizikalno društvo, 2018. str. 57

4. M. Bosiočić, F. Bert, J. Quilliam, S. E. Dutton, R. J. Cava, M. Požek, P. Mendels, NMR/μSR investigation of frustrated $J_1 - J_2$ chain $LiCuSbO_4$, The International Conference on Strongly Correlated Electron Systems Tokyo, Japan, 2013.

5. M. Bosiočić, F. Bert, J. Quilliam, S. E. Dutton, R. J. Cava, M. Požek, P. Mendels, Istraživanje $J_1 - J_2$ frustriranog lanca $LiCuSbO_4$ tehnikama nuklearne magnetske rezonancije(NMR)i mionske spinske rotacije(μSR), Knjiga sažetaka 8. znanstvenog sastanka Hrvatskog fizikalnog društva, Zagreb: Hrvatsko fizikalno društvo, 2013. str. 51

6. B. Perić, P. Planinić, M. Požek, M. Bosiočić, Gauter Régis Static solid-state NMR investigations of two niobium halide cluster compounds // Book of Abstracts / Llusar, Rosa (ur.). Castelló de la Plana, 2012. str. 45

7. M. Požek, M. Bosiočić, B. Pandey, B. Perić, M. S. Grbić, P. Planinić, R. Gautier, Istraživanje heksanuklearnih metalnih klastera širokopojasnim NMR-om i NQR-om, 7. znanstveni sastanak Hrvatskog fizikalnog društva , Zagreb: Hrvatsko fizikalno društvo, 2011. str. 60

8. B. Perić, P. Planinić, S. Cordier, R. Gautier, M. Požek, M. Bosiočić, Magnetic interactions in hexanuclear cluster compounds of niobium and tantalum, Abstract Book Trogir, 2011. str. O-27

9. M. Požek, M. Bosiočić, B. Perić, M. S. Grbić, P. Planinić, R. Gautier, Static solid state NMR and NQR investigation of niobium halide clusters 2nd Workshop on Recent Advances in Broad-Band Solid-State NMR of Correlated Electronic Systems - Knjiga sažetaka Trogir, 2011. str. P-16

10. M. Bosiočić, B. Perić, M. Požek, M. S. Grbić, P. Planinić, R. Gautier, Static ssNMR and NQR investigation of hexanuclear metallic clusters, EUROMAR 2011: Magnetic Resonance Conference : Knjiga sažetaka Frankfurt am Main, 2011. str. 302

11. B. Perić, P. Planinić, M. Požek, M. Bosiočić, R. Gautier, Solid state NMR investigation of two niobium clusters: $[Nb_6Br_{12}(H_2O)_6][HgBr_4]\bullet 12H_2O$ and $Nb_6Cl_{12}(H_2O)_4(OH)_2]\bullet 4H_2O$, The twentieth Croatian-Slovenian crystallographic meeting - CSCM20, Book of Abstracts and Programme, Zagreb: Croatian Academy of Sciences and Arts, Croatian Crystallographic Association, 2011. str. 33

12. M. Požek, B. Perić, P. Planinić, M. Bosiočić, R. Gautier, Static solid state NMR investigation of niobium cluster $[Nb_6Br_{12}(H_2O)_6][HgBr4]\bullet 12H_2O$, Poster Abstracts Kazan, Rusija, 2011. str. P39